The Henryk Niewodniczański Institute of Nuclear Physics
Polish Academy of Sciences

FORMATION AND PROPAGATION OF COSMIC-RAY ENSEMBLES

Oleksandr Sushchov

Supervisor
Dr. hab. Piotr Homola

A thesis submitted in fulfillment
of the requirements for the degree of

Doctor of Philosophy

Krakow, 2020

Formation and propagation of cosmic-ray ensembles

Oleksandr Sushchov

Abstract

High-energy particles interact with matter, electromagnetic fields and radiation while propagating through the Universe. As a result, they initiate particle cascades of various types and sizes; in the thesis, these cascades are referred to as cosmic-ray ensembles (CRE). Particles constituting CRE are messengers of the primary physical processes, thus it is important to establish in which circumstances they can reach the Earth and be detected using available or possible infrastructure. The outcome of this knowledge could help opening a new channel of studying astrophysics phenomena – correlated observations of cosmic rays on the global scale – to complement the present approach focused on detection and analysis of individual particles. Since recently, Cosmic-Ray Extremely Distributed Observatory (CREDO) Collaboration aims at pursuing a mission dedicated to CRE, and the research presented in the thesis is a part of the CREDO program.

The aim of the study is to simulate the formation and propagation of CRE in specific astrophysical conditions and to identify potential scenarios favorable for the detection of CRE. The focus was on high-energy electrons that are believed to play an important role in the physical processes that lead to CRE development and also during their formation.

The main method of this study is computer simulation of the interaction chain that the primary particle undergoes as it propagates through the interstellar space. The main tool used in the research is the publicly available and widely used Monte Carlo CRPropa 3 code. For the purposes of this work, a new algorithm called CRE-Pro was developed, providing external simulation of the shape and size of CRE. It can be used to analyze the results of CRPropa or similar codes simulating electromagnetic cascades, expanding their applicability and saving computing resources.

The thesis presents the results of simulations and CRE analyzes created within selected astrophysical scenarios with the use of the software described above. It has been shown that there may be a chance of observing CRE composed of synchrotron radiation photons emitted even at relatively large distances from the Earth, e.g. exceeding the size of the Galaxy. This result opens up new research perspectives in the field of particle astrophysics, pointing in particular to the possible extension of the observation horizon of high-energy cosmic rays, new possibilities for verifying certain astrophysical scenarios, as well as new research strategies relating to basic physical processes occurring under conditions impossible to reproduce in Earth laboratories.

Streszczenie

Cząsteczki o wysokich energiach oddziałują z materią, polami elektromagnetycznymi i promieniowaniem podczas propagacji we Wszechświecie. W efekcie inicjują kaskady cząstek różnego typu i wielkości; w niniejszej pracy kaskady te nazywane są zespołami promieniowania kosmicznego (ang. cosmic-ray ensembles - CRE). Cząstki tworzące CRE są przekaźnikami informacji o podstawowych procesach fizycznych, dlatego ważne jest, aby ustalić, w jakich okolicznościach mogą dotrzeć do Ziemi i zostać wykryte za pomocą dostępnej lub możliwej infrastruktury. Wynik tej wiedzy może pomóc w otwarciu nowego obszaru badań zjawisk astrofizycznych - globalnych obserwacji skorelowanych promieni kosmicznych jako uzupełnienia obecnego podejścia skoncentrowanego na wykrywaniu i analizie pojedynczyc cząstek. Od niedawna współpraca Cosmic-Ray Extremely Distributed Observatory (CREDO) ma na celu realizację misji poświęconej CRE, a badania przedstawione w niniejszej pracy są częścią programu CREDO.

Celem pracy jest wykonanie symulacji powstawania i propagacji CRE w określonych warunkach astrofizycznych oraz wskazanie potencjalnych scenariuszy sprzyjających możliwości wykrywania CRE. Skupiono się na wysokoenergetycznych elektronach, które, jak się uważa, odgrywają ważną rolę w procesach fizycznych prowadzących do rozwoju CRE, a także zachodzących w trakcie ich powstawania.

Główną metodą tego badania są symulacje komputerowe łańcucha interakcji, którym podlega cząstka pierwotna podczas propagacji w przestrzeni międzygwiazdowej. Głównym narzędziem zastosowanym w badaniach jest publicznie dostępny i szeroko stosowany kod Monte Carlo CRPropa 3. Na potrzeby niniejszej pracy opracowano nowy algorytm o nazwie CRE-Pro, zapewniający zewnętrzną symulację kształtu i wielkości CRE. Może być on używany do analizowania wyników CRPropa lub podobnych kodów symulujących kaskady elektromagnetyczne, rozszerzając zakres ich stosowalności i oszczędzając zasoby obliczeniowe.

W rozprawie przedstawiono wyniki symulacji i analiz CRE powstających w ramach wybranych scenariuszy astrofizycznych z wykorzystaniem opisanego powyżej oprogramowania. Wykazano, że może istnieć szansa zaobserwowania CRE złożonych z fotonów promieniowania synchrotronowego emitowanych nawet w stosunkowo dużych odległościach od Ziemi, np. przekraczających rozmiar Galaktyki. Wynik ten otwiera nowe perspektywy badawcze w obszarze astrofizyki cząstek, wskazując w szczególności na możliwe poszerzenie horyzontu obserwacji wysokoenergetycznych promieni kosmicznych, na nowe możliwości weryfikacji określonych scenariuszy astrofizycznych, a także na nowe strategie badawcze odnoszące się do podstawowych procesów fizycznych zachodzących w warunkach niemożliwych do odtworzenia w ziemskich laboratoriach.

Acknowledgements

First and foremost, I would like to express my sincerest gratitude to my PhD supervisor dr. hab. Piotr Homola, who allowed me to join the CREDO project as a PhD student at The Henryk Niewodniczański Institute of Nuclear Physics Polish Academy of Sciences, and then has been guiding and helping me during the whole time of my studies and thesis preparation.

Many thanks to my colleagues dr. hab. Dariusz Góra, dr. Niraj Dhital, dr. Kévin Almeida Cheminant and prof. Bohdan Hnatyk for their fruitful discussions and valuable advices regarding my research. I would also like to thank my close friends (and colleagues) for being by my side during these years: dr. Oleh Kobzar, dr. Volodymyr Marchenko, dr. Natalia Borodai, and especially dr. Artem Bohdan, who helped me a lot more than he can imagine.

Among many wonderful teachers who put their efforts into my education and helped forming my personality I would like to highlight two great persons. One of them is my favourite school teacher of physics Liudmyla Shostak, whose unforgettable lessons motivated me to become a physicist. The other is prof. Mykola Hrytsenko, my high school supervisor, who always believed in me and whose positive influence on my career is immense.

And finally, I would be remiss if I did not mention the two extraordinary women who have touched my life. First, my mother, Valentyna, who gave me life and since then has been protecting, inspiring and motivating me. And my wife, Kateryna, for her love and everlasting support.

Numerical simulations have been performed using computational and storage resources of the Prometheus system at ACC Cyfronet AGH and we warmly thank the staff for their always helpful supercomputing support.

Abbreviations and acronyms

AGN - active galactic nuclei
CMB - cosmic microwave background
CR - cosmic ray
CRE - cosmic-ray ensembles
CREDO - Cosmic-Ray Extremely Distributed Observatory
CTA - Cherenkov Telescope Array
DSA - diffusive shock acceleration
EHECR - extremely high energy cosmic ray
EGMF - extragalactic magnetic field
EM - electromagnetic
GCR - Galactic cosmic ray
GMF - Galactic magnetic field
GRB - gamma-ray burst
GZK-cutoff - Greisen-Zatsepin-Kuzmin cutoff
IACT - Imaging Atmospheric Cherenkov Telescope
ICS - inverse Compton scattering
ISM - interstellar medium
LIV - Lorentz invariance violation
MHD - magnetohydrodynamics
ODE - ordinary differential equation
QED - quantum electrodynamics
RKM - Runge-Kutta method
SHDM - super-heavy dark matter
SNR - supernova remnant
SPS - super-preshower
TD - topological defect
UHE - ultra high energy
UHECR - ultra high energy cosmic ray

Contents

Chapter 1

Introduction

The discovery of cosmic rays belongs to Victor Hess [1], who performed a series of balloon flights in 1911-1912 measuring the electric properties of the Earth atmosphere at 5.3 km above the sea level. As a result of his experiments, he concluded that the increase of the atmosphere ionization with the altitude could be explained by extraterrestrial sources of radiation. His results were confirmed by Robert Millikan in 1925 who named the radiation Hess had studied "cosmic rays".

During more than a century since the discovery of cosmic rays, their study made a spectacular progress and contains, contributes to and benefits from the research in many fields of astrophysics and particle physics. Starting from radioactivity driven environmental studies, cosmic ray physics helped progress of quantum electrodynamics and electromagnetic cascades theory, became the main way of discovery of new particles until sharing the field with the human-built laboratory accelerators, lead to the birth of space physics and played an important role in the evolution of Standard Model of particle physics. The interest in cosmic ray research boosted the development of instrumental tools, such as particle detectors of different types, and already mentioned accelerators designed to complement existing cosmic ray data. The extensive use of advanced technique allowed to obtain experimental data of significant amount and accuracy, and ongoing efforts on theoretically explaining this data enhanced our knowledge on the astrophysical processes. However, despite the great overall progress of cosmic ray physics, some problems still remain not fully understood and unexplained, thus stimulating a growing interest in the field.

Cosmic rays span a very wide energy range from around 1 MeV to the highest ever registered $3 \cdot 10^{20}$ eV (Fig. 1.1). The plot demonstrates the differential spectrum of cosmic rays with energies exceeding 100 GeV per nucleus (cosmic rays at lower energies are affected by the solar modulation, thus including them to this plot will not be so representative). It can be roughly described by a power-law distribution, $N(E) \propto E^{-\gamma}$, with the spectral index $\gamma \sim 3$.

However, over 14 orders of magnitude in energy and 34 orders in the flux there are

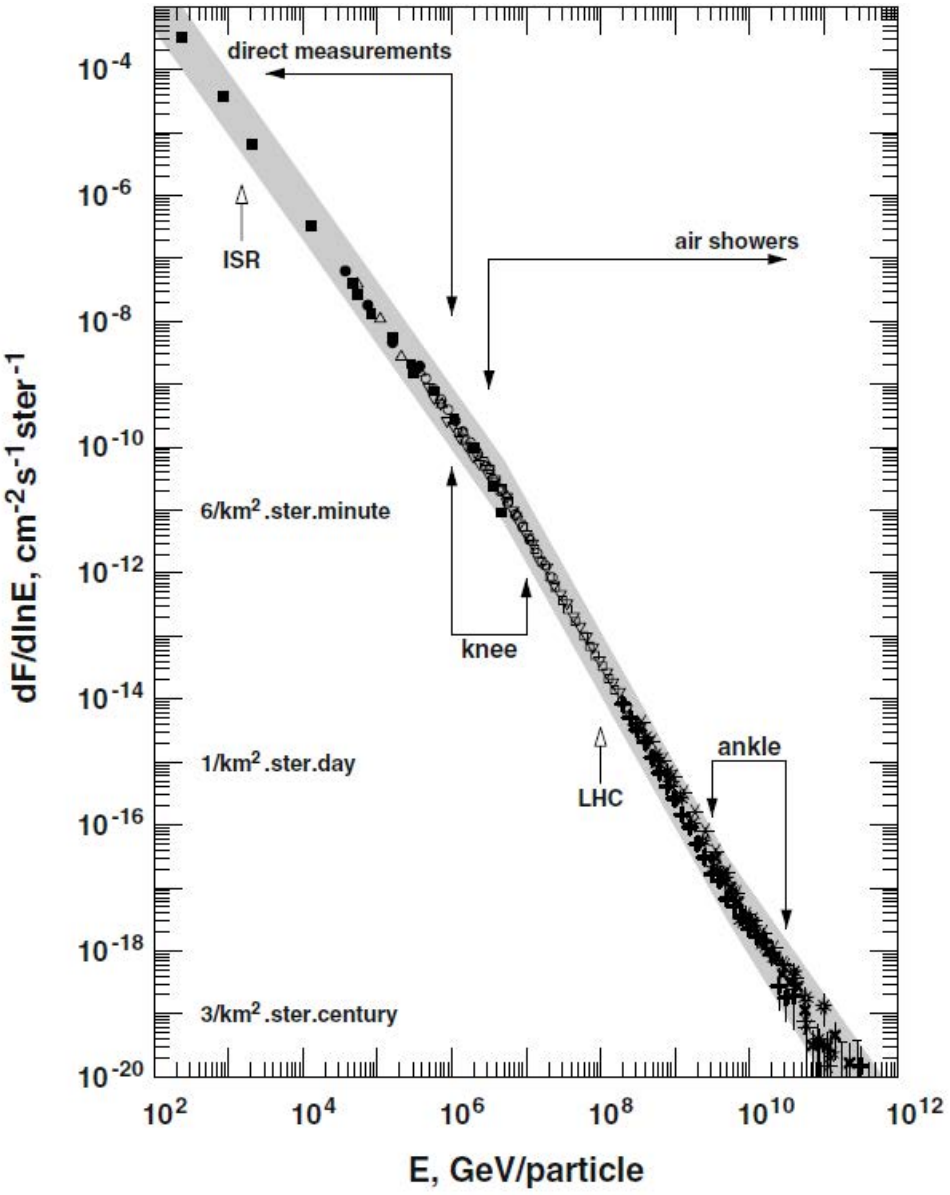

Figure 1.1: Cosmic rays energy spectrum (taken from [2]).

small, but important, regions where the slope of the spectrum changes. This fact may be the evidence that either the possible sources number is limited or the acceleration of cosmic rays is driven by the same mechanism, typical for different classes of astrophysical objects.

One of the features of the cosmic ray spectrum is the so-called "cosmic ray knee" - the steepening of the spectrum above 3 PeV. It is associated with the transition between the galactic and extragalactic sources of cosmic rays. It occupies the energy range $E \approx (1-5)$ GeV, and contains more subtle changes of the slope. Another feature of the spectrum is the so-called "cosmic ray ankle" - the flattening of the spectrum at around 5×10^9 GeV. The results of measurements performed in this energy range by different experiments [3, 4, 5] do not fully agree with each other, but cosmic rays with energies

beyond the "ankle" are believed to have an extragalactic origin [6]. At around 5×10^9 GeV the spectrum is cut off. It is usually explained by the GZK effect (see Section 2.5 of this thesis), independently predicted by K. Greisen [7], G. Zatsepin and V. Kuzmin [8] - the fast fragmentation of cosmic rays with the energies exceeding this range due to their interaction with the cosmic microwave background.

The origin of ultra-high energy cosmic rays (UHECR; $E > 10^{18}$ eV) still remains a puzzle for modern astrophysics. Different models have been proposed for its explanation, following two main approaches. One group of scenarios, called bottom-up models, considers acceleration of particles up to ultra-high energies [9]. The most likely acceleration objects are shock wave structures in active galactic nuclei (AGN), gamma-ray bursts (GRB), jets of radio galaxies etc. Another group of scenarios, called top-down models, analyzes the possibility of UHECR origination as a result of decay or annihilation of supermassive particles, which can be either metastable or emitted by topological defects in the present epoch [10, 11]. Neither of these approaches neglects UHECR photons as a component of the UHECR flux, though the fractions predicted by various models differ: from percents in the bottom-up scenarios [12] to up to a half in the top-down scenarios [13]. New physics scenarios describing propagation or interaction effects, such as Lorentz invariance violation (LIV) [14], can be also tested with ultra-high energy (UHE) photons. One of the main consequences of the LIV is the increase of the photons mean free path, which leads to extension of the photon flux. The main cosmic ray experiments, however, have not unambiguously identified any of UHE photons so far, thus setting stringent upper limits which under some assumption might disfavour the top-down models of UHECR production [15, 16]. Nevertheless, the search of UHE photons is still a tempting task. It could be argued, that the physics in the UHE range is not fully understood, because it relies on the interaction models derived from the extrapolations made for the experimental data at lower energies. This leads to the increase of uncertainties and thus complicates the exact treatment of the UHECR data. Thereby, an observation of a UHE photon is of extreme importance for many astrophysical problems.

Aforementioned uncertainties in the UHECR data interpretation still allow making alternative assumptions, considering the existence of UHE photons. For example, one possible explanation of their non-observation is negligible chances to reach the Earth due to interactions on their way. In this work we will highlight and study this assumption in detail.

High energy particles, including photons, should interact with matter, fields and different types of radiation while propagating through the Universe. These interactions obviously initiate particle cascades of various types and sizes, hereafter referred to as cosmic-ray ensembles (CRE). While the modern cosmic ray research is based on the detection and analysis of cosmic rays using individual detectors or arrays, the study of cosmic particles correlated (temporarily and/or spatially) on the global scale remains less

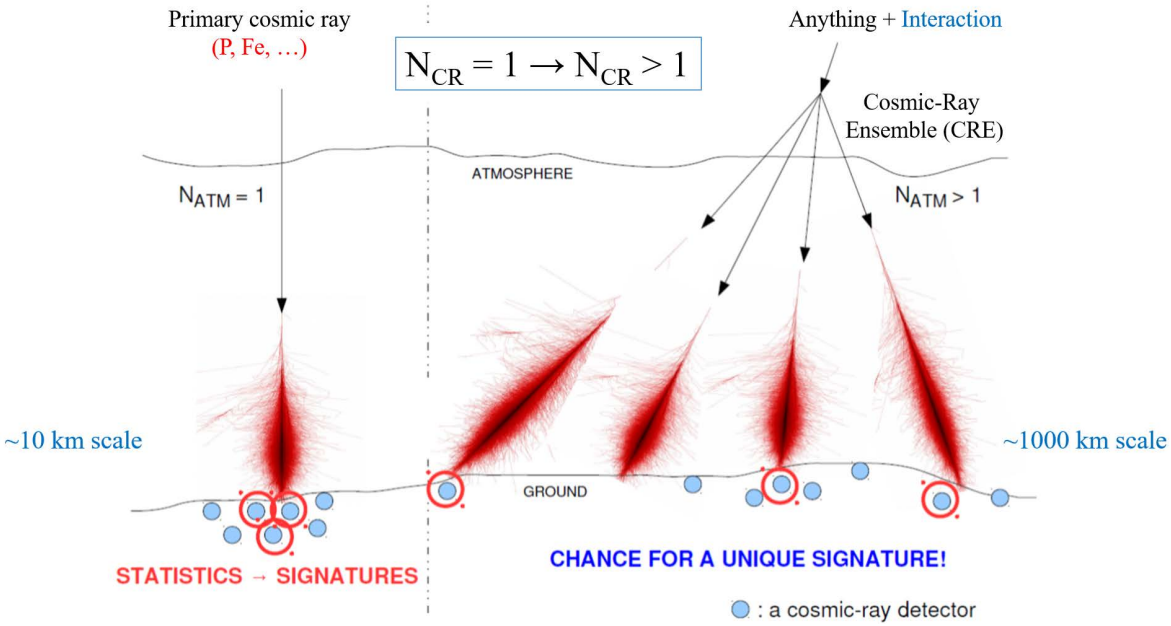

Figure 1.2: Cosmic-Ray Ensembles: a new approach to cosmic-ray research (taken from [20]).

popular. However, the effort undertaken in this direction could provide a better understanding of the physical processes that might take place at energies rarely considered, including the highest known. Since recently, Cosmic-Ray Extremely Distributed Observatory (CREDO) Collaboration [17, 18, 19, 20] aims at pursuing a mission dedicated to CRE, and this thesis is planned to become a part of the CREDO program.

The aim of the thesis is to investigate the processes occurring as a result of propagation of high energy particles through the Universe. The focus will be made on UHE electrons, either accelerated in some astrophysical environments or originating in pair production process by UHE photons, which are believed to produce the largest CRE. In this work the conditions under which it will be possible to identify at least two cosmic rays belonging to one CRE at the Earth (Fig. 1.2), are studied. We also discuss the scientific gain of such observations and the potential of CRE-oriented research for shedding light on yet unobserved or new physics manifestations.

The main method of our investigation is computer simulations in order to study the whole chain of interactions undergone by the primary particle under various physical conditions. We use a publicly available software, CRPropa 3, a general and universal tool enabling efficient and versatile modeling of the astrophysical media producing as output primary and secondary cosmic messengers (see in Section 4.1 for more details). We also developed an algorithm which allows to analyze the output of CRPropa or other codes able to simulate the particle cascades origination and propagation, externally modeling

the sizes of resulting CRE and the distribution of their constituents. The description of this code is provided in the thesis, and its implementations for the analysis of astrophysics scenarios are discussed.

The thesis is organized as follows. Chapter 2 contains the scientific motivation of studying the cosmic ray ensembles. Namely, we discuss certain key problems of cosmic ray physics, including the models of UHECR origin and propagation effects. Chapter 3 is dedicated to physics processes which are necessary to be taken into account in the simulations of a CRE rise and propagation. The technical part concerning the software, including CRPropa description and examples of use, is presented in Chapter 4. We also provide a more detailed discussion of some modules of this code, which are of the most importance for our study. Chapter 5 introduces the algorithm, developed by the author for the analysis of the simulations output in terms of a CRE-oriented study. The results are presented in the next chapters. Chapter 6 demonstrates an exemplary CRE-aimed analysis to highlight its basic principles, while Chapter 7 shows the results of this analysis application to the specific astrophysical scenarios, namely Galactic Center as a CRE source and uniform distribution of CRE sources over the Galaxy. The summary of the thesis together with the general discussion of the results and outlook of the further investigations, can be found in Chapter 8.

Chapter 2

Cosmic rays

It is known that the most common components of cosmic rays (CRs) are protons, nuclei and electrons, primary in a sense of their capability to be directly accelerated to relativistic energies by powerful sources. Some nuclei (Li, Be, B) as well as the anti-particles (positrons and antiprotons) are produced by the primaries as results of their interactions with matter and background fields inside the accelerators [21]. The flux and spectrum of CRs is also known quite well (Fig. 1.1), but their exact origin is still among the problems lacking a coherent explanation despite a considerable amount of experimental data and extensive theoretical efforts in domain of cosmic ray astrophysics.

The main ideas on the CRs origin are based on the analysis of the CR spectrum features, mentioned in Chapter 1. While the transition from the Solar to the Galactic cosmic rays occurs at around 1 GeV, the upper boundary of the latter is more debated; some models [22, 23] propose the "knee" as the limit of the Galactic CR spectrum from above, the others consider the region between the ",of galactic as well as extragalactic origin [24, 25, 26]. Nowadays there is more confidence about the extragalactic nature of extremely high energy CRs (EHECR; $E > 10^{18}$ eV) [27, 28], but the exact mechanisms leading to their origin are still a puzzle.

2.1 Galactic cosmic rays

It is widely believed that the main contribution to the flux of the Galactic cosmic rays (GCR) belongs to Supernova Remnants (SNRs). This idea was introduced in [29], and since then several arguments in support of this paradigm have been formulated. The main of them results from the energy considerations and was pointed out in [30]. Since the average energy released per a Supernovae explosion is around 10^{51} erg, and the number of such events is estimated as 2-3 per century, the mean energy production rate caused by them is roughly 10^{42} erg/s. On the other hand, CR production rate, calculated with respect to the average time spent by CRs before leaving the Galaxy, is about 10^{41} erg/s, which means that 10% of Supernova explosions energy is enough to be converted into

the kinetic energy of CRs to provide the observed flux of the latter. It should be noted, however, that from the formal point of view other plausible classes of GCR sources, such as pulsars, microquasars, GRBs, young stars with the powerful mechanical winds etc. can also meet these energy requirements.

Theoretically the SNR paradigm is well described by the diffusive shock acceleration (DSA) model, applied to the strong shocks in SNRs [31, 32, 33, 34]. According to this theory the CRs are mainly produced in the shock waves, originating as a result of interaction of supernova ejecta with the interstellar medium. The shock waves are usually non-relativistic ($v \simeq 10^4$ km/s), and can energize the particles via the first-order Fermi process [35, 36]. Particles are accelerated when undergoing multiple scattering off magnetic inhomogeneities associated with the moving shock front. The name of the process denotes linear dependence of particles acceleration on the front velocity, which results in the power-law spectrum with energy spectral index $\alpha \approx 2$. The spectrum is modified during the diffusive propagation of the particles through the ISM after they leave the acceleration region. The particles with higher energies escape the Galaxy faster, that leads to the increase of the overall spectral index up to $\alpha \approx 2.7$ at the Earth, which is consistent with observations.

Multiwavelength studies of SNRs confirm the high-energy particles production at these sources. For example, the measured synchrotron spectral index for SNRs has a typical value $\alpha_{synch} \simeq -0.5$. Using the formula $\alpha_{synch} = \dfrac{1-\alpha}{2}$ [9], one can obtain the power-law energy distribution of electrons producing the synchrotron emission, and its value, $\alpha \simeq 2$, is in agreement with the DSA theory. According to X-ray observations of SNRs [37, 38], the fraction of SNRs energy converted into the acceleration of GCR is about 10%, which also fits the theoretical estimations. High-energy gamma-ray data [39, 40, 41] also confirms acceleration of particles in the shock regions up to at least 10^{14} eV.

2.2 Extragalactic cosmic rays

The suggestion that EHECRs, i.e. the cosmic rays with energies exceeding 10^{18} eV, are of extragalactic origin [42], is a logical consequence of the fact that their gyroradii are too large to let them stay within the Galaxy during significant time. The same argument is often used to mark the same energy as the highest possible for the GCR so that a transition zone at the energy of around 10^{18} eV (the "ankle") is formed in the CR spectrum [43]. Yet the mechanisms responsible for such enormous energies of a single particle remain unknown. As it was briefly mentioned in Chapter 1, the origin of EHECR is attempted to be explained within two groups of scenarios [44], "bottom-up" models, suggesting acceleration of the particles up to extremely high energies, and "top-down" models, which consider EHECRs as secondary particles originated as a result of decay or annihilation of a hypothetical particle with a higher energy.

2.2.1 Bottom-up scenarios

Bottom-up scenarios can be separated with respect to two distinct processes of the particles acceleration they consider: diffusive shock acceleration (interactions of particles with magnetized plasmas via Fermi mechanisms) and one-shot acceleration, which can occur in very high electric field [45], induced by the rapidly rotating magnetized objects (supermassive black holes [46, 47], young neutron stars [48], white dwarfs). The energy gained by a particle via diffusive process depends on time the particle is confined within the source, which in turn is the function of the size and magnetic field strength of the accelerator. The relation for the maximal energy a particle of charge Ze can reach in the accelerating site of size R and magnetic field B was formulated [49]:

$$E_{max} = \beta Ze \left(\frac{B}{1\mu G}\right)\left(\frac{R}{1kpc}\right) \text{ EeV}, \tag{2.1}$$

with β standing for the velocity of the shock wave. Fig. 2.1 illustrates the acceleration capabilities of astrophysical objects. To accelerate a given particle up to 100 EeV the source should be located above the correspondent line on the diagram.

One can list the following classes of objects as potential UHECR sources: GRB-related processes, neutron stars and other similar compact objects, AGN cores and jets, large-scale structures resulting from the collision of galaxies, hot spots and radio lobes of radio active galaxies. However, more accurate account for the radiative energy losses in magnetic fields sets additional limitations on the plausible UHECR acceleration sites [51]. It is inferred that regardless of the initial energy of the particle it cannot exceed the "critical" energy value, defined by

$$E_{cr} = \frac{3}{2}\left(\frac{Am_pc^2}{Ze}\right)^4 \left(B^2R\right)^{-1} \sim 3\times 10^{16}\frac{(A/Z)^4}{B_G^2 R_{kpc}} \text{ eV}. \tag{2.2}$$

One-shot acceleration is characterized by a very high total energy density in the candidate sources which causes intense energy losses. The maximal energy of the accelerated particle can be well approximated by (2.1) only in case the losses are negligible, but when they become comparable with the critical energy (2.2), the energy above which further acceleration is impossible (losses start to dominate), is defined by

$$E_{eff} \simeq \sqrt{E_{max}E_{cr}} \sim 10^{20} A^2 B^{-1/2} Z^{-3/2} \text{ eV}. \tag{2.3}$$

This results challenges the assumption of compact sources as UHECR accelerators candidates in favor of extended structures (radio lobes, galactic halos, galaxy clusters etc.), since it sets the limit on the source sizes as well.

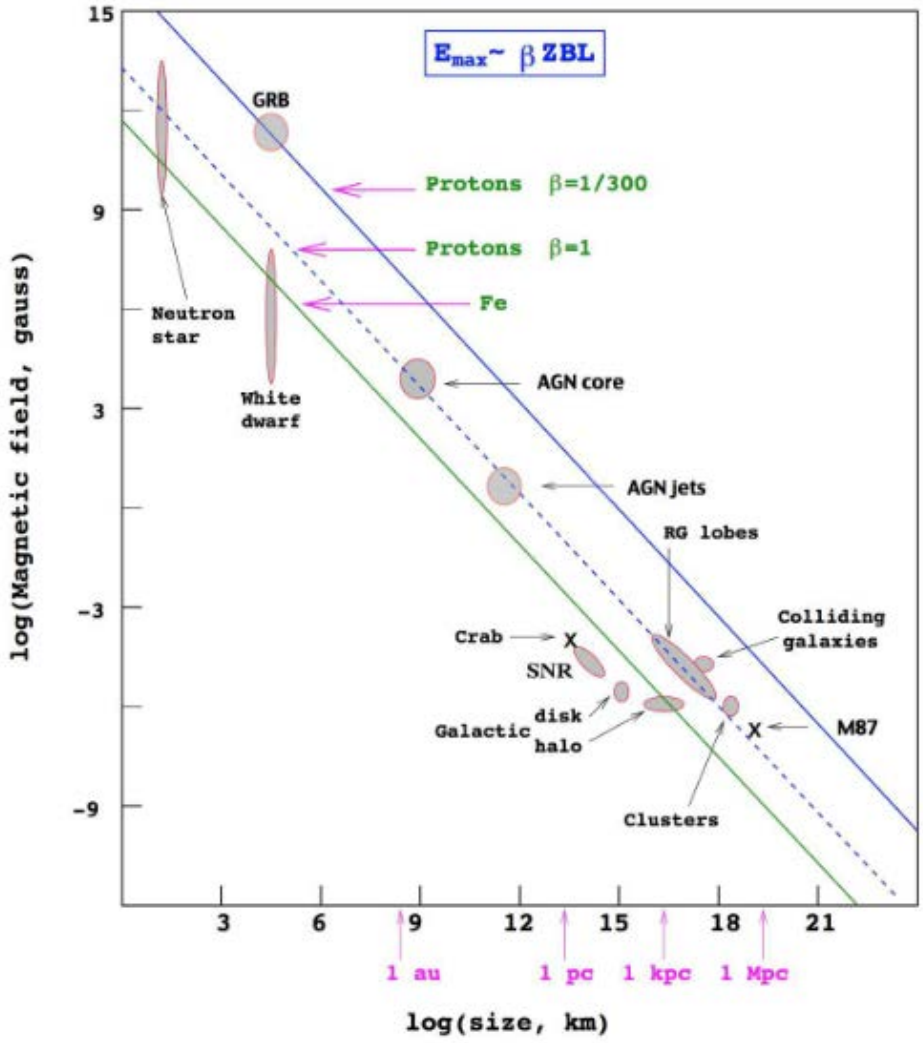

Figure 2.1: Candidate CR acceleration sites (taken from [50]).

2.2.2 Top-down models

An alternative approach to the explanation of existence of UHECR, especially those registered beyond the GZK-cutoff, is the assumption that they are not accelerated as such, but are produced via the decay of some supermassive X particle or by collapse of a topological defect. Such a process should initiate production of quarks and leptons, resulting in a large cascade of photons, neutrinos and light leptons with a small fraction of nucleons, with cosmic rays emerging from these cascades already having the energies of ultra-high scale. There are some general conditions which should be satisfied by the hypothetical X particle in order to explain the observable UHECR flux:

- The decay should occur at distances within 100 Mpc, so that the resultant particles energy losses on their way to the Earth are not significant.

- The X particle mass should exceed the value of the highest observed UHECR energy (~ 100 EeV).
- The ratio of the X particles volume density to their decay time should be consistent with the observed UHECR flux.

Topological defects (TD) are believed to be formed during the consequence of spontaneous symmetry breaking phase transitions in the early Universe. They include, for example, such objects as magnetic monopoles [52, 53], cosmic strings [54], domain walls [55], textures and their hybrid combinations [56]. Among the listed defects only the monopoles (point-like) and cosmic strings (1-dimensional) are considered as potential UHECR sources. In the processes of radiation, interaction or collapse of TD, the GUT energy scale particles, which decay instantly, are produced. The flux of UHECR is related to the TD number density and their radiation, collapse or interaction rate.

Metastable superheavy relic particles of mass $m_X \simeq 10^{12}$ GeV and lifetime exceeding or comparable to the age of the Universe were proposed as UHECR sources candidates [57, 58, 59, 60] (Superheavy Dark Matter, or SHDM, model). Unlike TD, relic particles should be aggregated due to gravitational effects in galaxies and galaxy clusters and act as a cold dark matter component, which implies that the contribution of X particles to the UHECR flux will be dominated by the Galactic halo component over the extragalactic one. Besides, the photon dominated UHECR spectrum in this case should contain no signatures of the GZK-cutoff. For the SHDM scenario the flux of UHECR is defined by the ratio of their density over the lifetime.

Another phenomenon considered to be capable of generating UHECR is the so-called "Z-bursts", decays of Z-bozons originated via resonant interactions between high energy and background neutrinos [61, 62, 63, 64]. The main problem of this scenario is the incident UHE neutrino flux: it cannot be measured directly and thus only flux bounds derived indirectly should be taken into consideration. In addition, the very mechanisms of UHE neutrino production require explanation with the acceleration models or the decay of TD.

Summarizing two previous subsections, one should conclude, that there are still problems with the unambiguous interpretation of the high-energy end (in case its existence does get proven) of the CR spectrum. The bottom-up models are self-limiting, i.e. the condition (2.1) for the maximal energy obtainable within a source sets limitations on its size R and magnetic field strength B, hence the highest energies observed ($\geq 10^{20}$eV) can barely be achieved even in the most powerful objects of reasonable R and B. Another challenge to the theory is that no obviously identifiable sources of UHECR have been found so far. On the other hand, top-down models, despite all their convenient features, like the absence of the direct connection to the real astrophysical objects, fail short with getting the experimental evidences. The fraction of UHE photons in the CR spectrum

predicted within top-down models, should be significant, while the latest experiments, carried out by Auger and TA, show the contrary (Fig. 2.2). These results seriously reduce the chances of exotic models to explain the origination of UHECR.

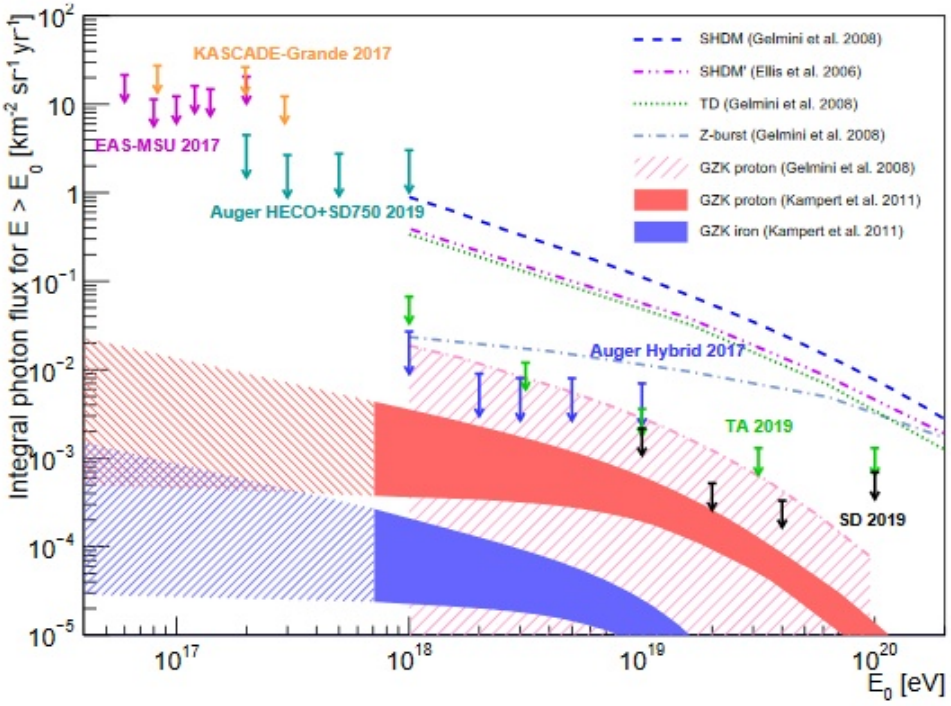

Figure 2.2: Comparison of experimental (TA [65], Auger surface and hybrid detectors [66], KASCADE-Grande [67] and EAS-MSU [68]) upper limits on the diffuse UHE photon flux with predictions of theoretical models, listed in the plot legend (taken from [66]).

2.3 Gamma Rays

In the thesis we consider gamma-rays as a significant contributor to the CR flux. They are also an important component of CRE, in particular, of electromagnetic cascades, which are the main focus of this research. At energies exceeding 100 MeV the gamma-ray flux is dominated by diffuse emission resulting from interactions of cosmic rays with the interstellar gas and radiation fields in the Galaxy, but due to the fact that photons, unlike charged CRs, are propagated without being deflected by magnetic fields, gamma-rays can also be directly associated with their sources. The latter include AGN, blazars, pulsars and pulsar wind nebulae, SNRs, and are considered among the most energetic compact objects in the Universe.

Direct observation of gamma-rays (the atmosphere is opaque to them) is possible with the space satellites (Fig. 2.3). The discovery of cosmic gamma-rays belongs to the OSO-3 satellite [70] in 1960s. A decade later, SAS-2 [71] and COS-B [72] satellites found and

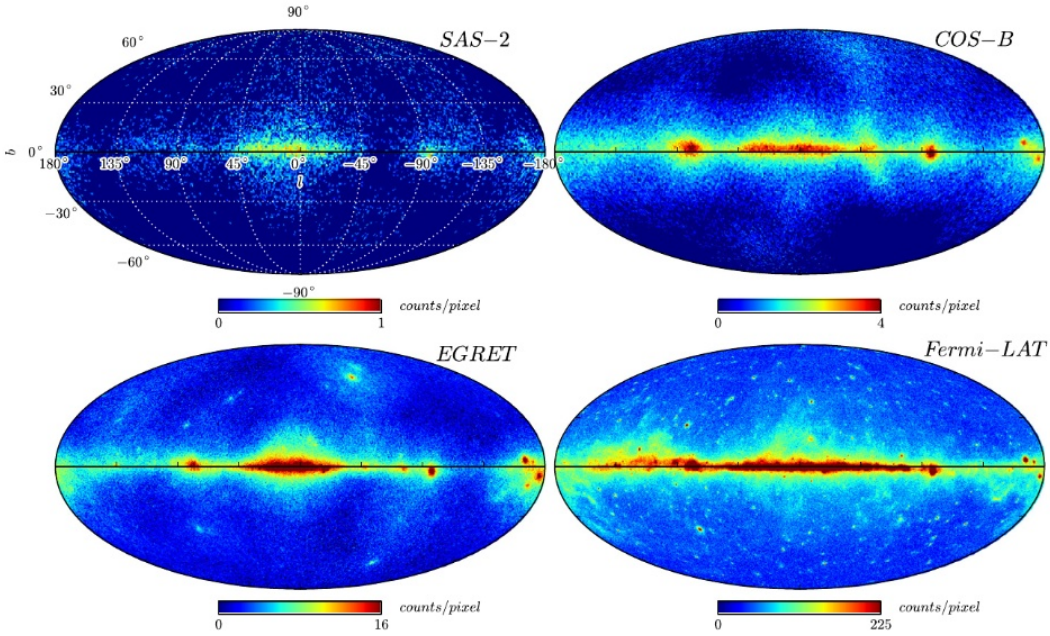

Figure 2.3: Progress in γ-ray sky mapping (Mollweide projections of galactic coordinates) comparing four different satellites: SAS-2 (1972, top left), COS-B (1975, top right), EGRET (1991, bottom left) and Fermi-LAT (2008, bottom right) [69]).

investigated the first gamma-ray sources and built the first sky maps. EGRET experiment [73] operating from 1991 till 2000 helped improve the sky maps and also discovered new sources. Since 2008 so far the most precise instrument, the Fermi-LAT [74], operates in energy range from 20 MeV to over 300 GeV. Due to its improved resolution the discovery of new structures such as Fermi bubbles [75] became possible. The last satellite detector to be mentioned is the AMS-02, installed at the International Space Station. Though designed for the detection of charged particles, it is also capable to track high energy gamma-rays with great precision.

The ground-based instruments perform measurements of Cherenkov emission from air showers induced by very high gamma-rays The main operating experiments are HAWC [76] and the telescopes using the so-called Imaging Atmospheric Cherenkov Telescope (IACT) technique: MAGIC [77] and VERITAS [78] and H.E.S.S. [79], working in a sensitivity range from 50 GeV to 50 TeV. They have an excellent angular resolution, but are limited in a field of view, which make them applicable to the observation of point sources rather than of diffuse emission. The next generation IACT telescope, called CTA [80], which is under construction, will widen the energy range and improve overall characteristics, which will open new opportunities to gamma-ray astrophysics.

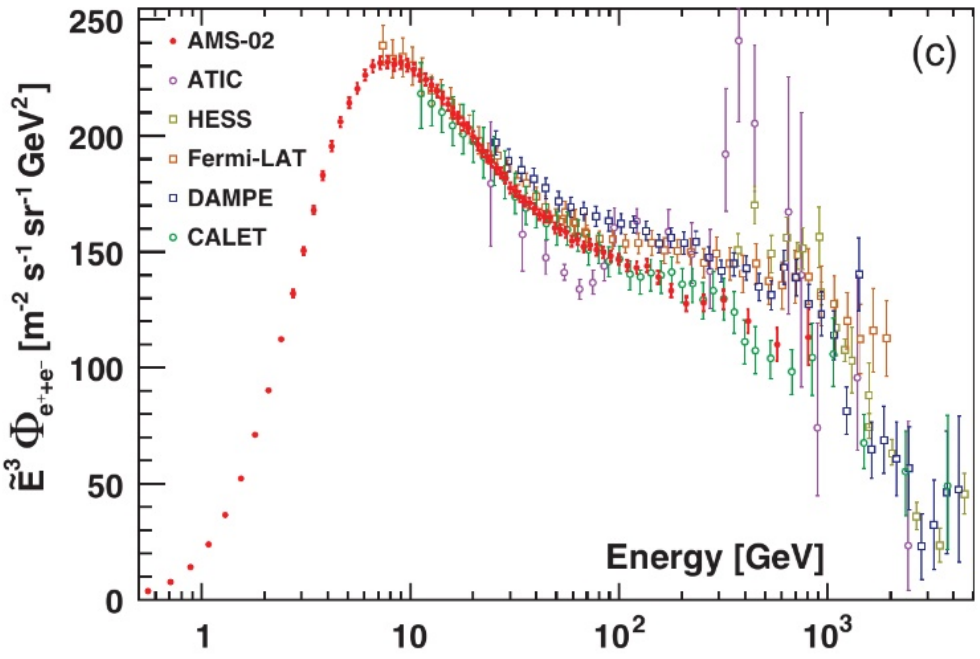

Figure 2.4: Sum of the fluxes of CR electrons and positrons, multiplied by E^3, as a function of the electron/positron energy (taken from [81]).

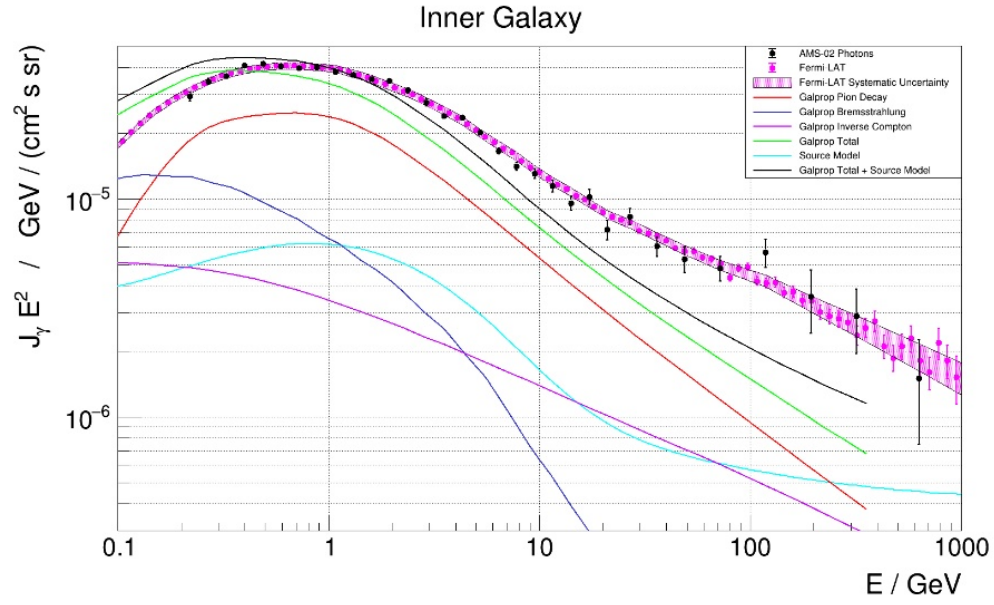

Figure 2.5: Comparison of the measured γ-ray flux in the inner galaxy with a recent GALPROP model [57]. AMS uncertainties are statistical only. GALPROP components: Fluxes for π^0-decays (red), bremsstrahlung (blue) and inverse Compton emission (magenta). Green line: Sum of GALPROP predictions for diffuse emission. Cyan line: Summed model prediction for γ-ray sources. Black line: Sum of green and cyan lines, corresponding to the total model prediction (taken from [82]).

Cosmic-ray electrons and positrons, the other important constituents of CRE, are directly linked to some processes, like bremsstrahlung or synchrotron radiation, resulting in diffuse gamma rays emission. Physics of gamma ray sources often refers to the mechanisms involving e.g. inverse Compton scattering (ICS) to explain the production of high energy photons. Some experiments measure the total flux of electrons and positrons, being unable to distinguish these species (e.g. ground-based telescopes, Fermi-LAT), while the others, equipped with magnets, are able to calculate the flux for each component separately (e.g. AMS-02). The summed flux of electrons and positron is compared for different detectors in Fig. 2.4.

The results of modeling of various processes leading to creation of gamma rays are compared to the observations taken by AMS and FERMI-LAT for the inner galaxy region ($-20^\circ < l < 80^\circ, |b| < 8^\circ$, where l and b are the galactic longitude and latitude, respectively) in Fig. 2.5.

2.4 Propagation of UHECR in the magnetic fields

When travelling through space, UHECR experience various interactions with the ISM components resulting in the changes of their energy, composition (more details in Section 2.5) and deflections of their trajectories. The latter occur mostly due to the magnetic fields acting on moving charged particles via the Lorentz force. Magnetic deflections of UHECR trajectories hampers direct identification of their sources. On the other hand, the process depends on the particle rigidity E/Ze, where E is the energy, Ze is the electric charge (in this regard a 1 EeV proton is equivalent to a 26 EeV iron nucleus, etc.), which is helpful for the proper understanding of the particle propagation details under certain conditions. In the present section of the thesis we will briefly overview the influence of magnetic fields on the propagation of UHECR, paying particular attention to the model of the Galactic magnetic field used in the simulations performed as a part of our research.

2.4.1 Galactic magnetic field

Most of the visible matter found in the Universe exists in the form of plasma, thus it is ionized which provides suitable conditions for the generation of magnetic fields. The latter play an extremely important role in many astrophysical processes taking place in planets, stars, galaxies, galactic clusters, interstellar and intergalactic media [83, 84, 85, 86].

The origin of the first cosmic magnetic field still remains unsolved, while the most promising theory for the evolution of fields leading to their current observable state is the dynamo, which transforms mechanical into magnetic energy. The interplay of motion of charged particles in plasma and electromagnetic fields generated by this motion is

described by the equations of magneto-hydrodynamics (MHD) [87].

The magnetic field of our Galaxy (the galactic magnetic field, from now on referred to as the GMF) is of more importance for astrophysics than the fields of other galaxies. It has not only a great impact on the processes within the Galaxy, but also affects some extragalactic observations. The information on its structure and strength is obtained from the observational data. There are several channels of observation of the GMF, including polarization of starlight, polarized thermal dust emission from clouds, Zeeman splitting of lines, diffuse synchrotron emission (radio and microwave), Faraday rotation of polarized sources (galactic and extragalactic), Faraday tomography (galactic and extragalactic), rotation measure synthesis [88, 89]. None of these measurement methods is capable of giving an unambiguous picture of the large-scale GMF, but their combined data allows estimating the GMF structure as well as its strength.

Observers separate the GMF into the following components:

- The regular (coherent) field, i. e. the component which direction remains coherent at a large distance
- The isotropic random (or isotropic turbulent) field, i. e. the component with equal dispersions in all dimensions
- The ordered random [89] (anisotropic turbulent [88], striated [90]), i. e. the component with anisotropic fluctuations of the local field

Such a separation of the magnetic field is important for understanding its relation to the other components of the ISM and is useful for computational feasibility, since the components of the field may be generated independently.

There are numerous models of the GMF, which evolved both qualitatively and quantitatively with the improvement of observational tools and increase of the analyzed data sets [91, 92, 93, 94, 95, 96, 97, 98, 99, 90]. We will focus on the GMF model introduced in [90], known as the JF12 model, because it is widely used by the cosmic-ray community for different astrophysics applications. For instance, it is one of the available options of modeling the GMF in the CRPropa code (Chapter 4), which we used in our simulations of the propagation of charged particles in the Galaxy. According to this model, the regular GMF consists of the spiral (following the distribution of matter) disc field and the field of the halo, separated into poloidal and toroidal components. Unlike the earlier models, in which the poloidal field was approximated by a dipole, the JF12 model treats this component as having an X-like profile in the vertical plane. Other components included to the model are a large-scale striated field and a small-scale isotropic random field.

The large-scale disc field (its best fit is shown in the upper left panel of Fig. 2.6) is modeled following [100]. It has 11 free parameters: the strength of the toroidal molecular

ring region, eight spiral arms field strengths, and two parameters corresponding to the transition from the disc to the halo. The disc field is z-symmetric.

The toroidal halo is modeled by the six parameters: two field strength amplitudes, two vertical and two radial transition parameters. This component of the field is z-asymmetric. The poloidal halo model contains four parameters: the strength of the central field, the angle of elevation and two radial parameters.

From the top panels of Fig. 2.6 one can see that despite the similar look the magnetic field just above the mid-plane is not identical to the one below the same plane. This can be explained with superposition of the field components with different symmetry with respect to the XY plane. At $|z| = 1$ kpc the field is dominated by the halo component, but still exhibits signs of the superposition with the X-field (Fig. 2.7), and even the disc field.

The striated field is modeled by 13 parameters, 10 of which describe the disc field (spiral arms, the central part and the disc thickness) and 3 remaining are used for the halo: the central part and the vertical extent in two opposite directions. All the components were modeled to ensure zero magnetic divergence. The entire list of estimated parameters is presented in the Table 1 of [90]. The CRPropa code implements the JF12 model only with the best-fit parameter values.

As far as the influence on the propagation of UHECR is concerned, the following remarks should be made. Since the field is non-uniform, the deflection of particles propagating in different directions is highly asymmetric across the sky even within a single field model. The average deflection of a 100 EeV proton estimated for different toy models gave values from 2° to 4° [101]. However, according to [90], the particles with the same rigidity should be a subject of generally higher deflections, around 8.7° in average. Moreover, not only the deflection value, but also its direction, calculated for different GMF models, may vary significantly [102, 103].

2.4.2 Extragalactic magnetic field

The origin of extragalactic magnetic fields (EGMF), their spatial distribution and evolution are still not fully understood [105, 106, 107, 108]. Till now only ~ 1 μG magnetic fields in the central parts of galaxy clusters have been measured experimentally [109]. The upper limits on (density-weighted) magnetic field in the filaments $B_{fil} \leq 0.03(0.13)$ μG and primordial (void) field $B_v \leq 1.0$ nG are inferred from the cross-correlation of the 2.3 GHz S-PASS survey with the constrained MHD local cosmic web simulations [110]. The similar ∼nG upper limit on the smoothed over 1 Mpc void field is obtained [111], based on the Faraday rotation measurements of extragalactic sources and Planck data combined with the South Pole Telescope cosmic microwave background (CMB) polarization measurements ($B_{1\ Mpc} < 1.2$ nG at 95% C.L) [112]. Meantime, the suppression of

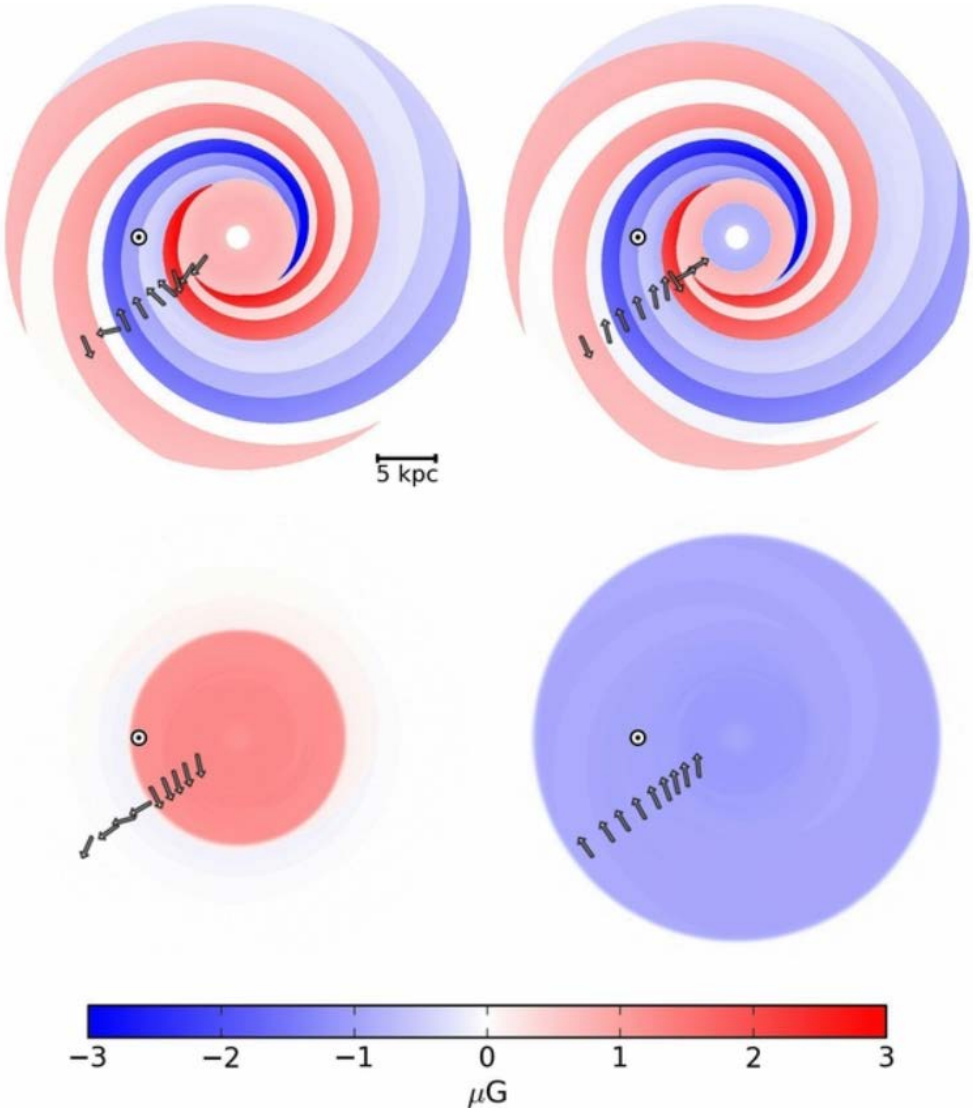

Figure 2.6: Top view of slices in the XY plane of the JF12 GMF model. Top row, from left: slices at $z = 10$ pc and $z = -10$ pc. Bottom row, slices at $z = 1$ kpc and $z = -1$ kpc, respectively. The color scheme shows the magnitude of the total regular field, with negative values if the azimuthal component is oriented clockwise. The location of the Sun at $x = -8.5$ kpc is marked with a circle. The arrows show the direction of the field (taken from [90]).

low-energy secondary gamma ray emission from TeV-blazars allows estimating the lower limit in voids at level $B_v \geq 3 \times 10^{-16}$ G for the correlation length $\lambda_B \geq 0.1$ Mpc [113].

Since the stronger field regions enclose a small fraction of the Universe ($\leq 10^{-6}$), the EGMF is usually modeled as a turbulent field with a Kolmogorov power spectrum with a ∼nG RMS strength. Its influence on the UHECR propagation in this case can be described in terms of diffusion process in the particle momentum space. It results in a small-angle random scattering around the main trajectory in the regular field, that allows calculating the average angular deflection Θ_{rms} and the corresponding time delay τ_{rms} in

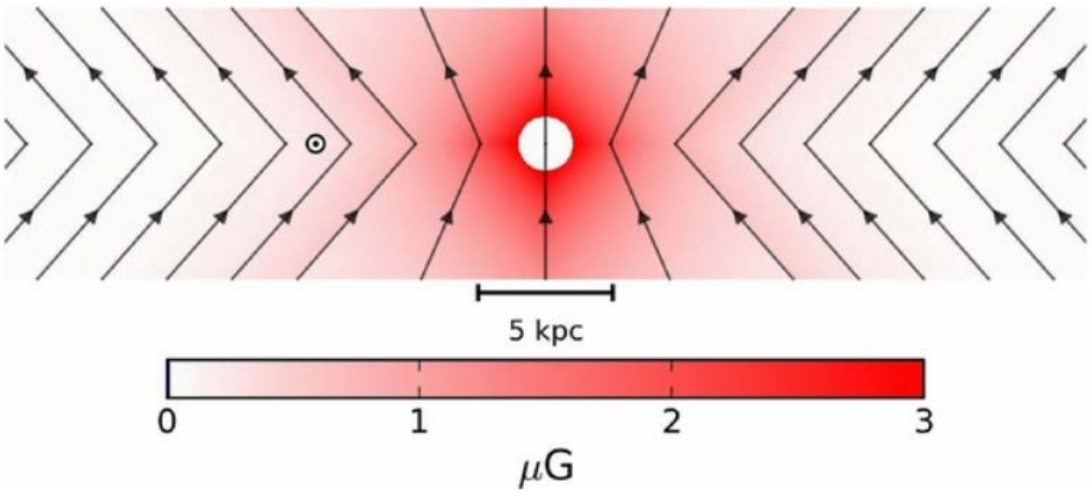

Figure 2.7: x-z slice of the galaxy showing only the out-of-plane "X" component. The black lines crossing the mid-plane at ±4.8 kpc trace the boundary between the outer region with constant elevation angle, and the inner region with varying elevation angle. The black arrows show the direction of the field (taken from [90]).

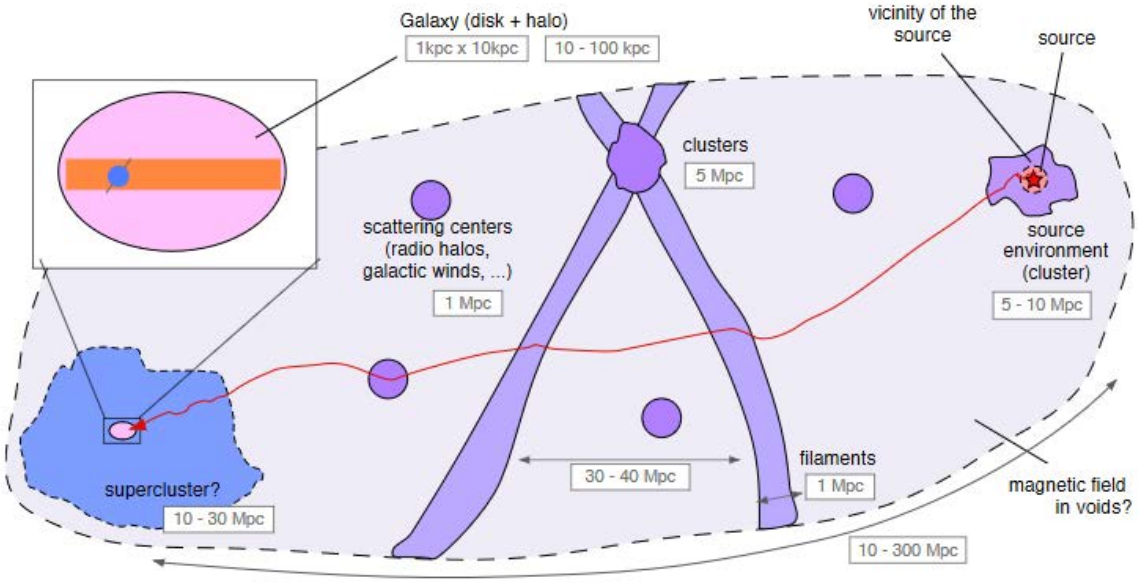

Figure 2.8: Schematic structure of the EGMF. The typical sizes of the objects and distances separating them are indicated in grey (taken from [104]).

the random field of B_{rms} strength with the coherence length l_c [114, 115] analytically:

$$\begin{aligned}\Theta_{rms}(E,L) &= \sqrt{\frac{2}{9}}\left(\frac{Ze}{E}\right) B_{rms}\sqrt{l_c L} \\ &\simeq 0.8^\circ \left(\frac{E}{10^{20}\text{ eV}}\right)^{-1}\left(\frac{L}{10\text{ Mpc}}\right)^{\frac{1}{2}}\left(\frac{l_c}{1\text{ Mpc}}\right)^{\frac{1}{2}}\left(\frac{B_{rms}}{1\text{ nG}}\right)\end{aligned} \tag{2.4}$$

and

$$\tau_{rms}(E,L) = L\Theta^2_{rms}(E,L)/4c$$
$$\simeq 1500Z^2\left(\frac{E}{10^{20}\text{ eV}}\right)^{-2}\left(\frac{L}{10\text{ Mpc}}\right)^{2}\left(\frac{l_c}{1\text{ Mpc}}\right)\left(\frac{B_{rms}}{1\text{ nG}}\right)^{2}, \tag{2.5}$$

where L is the UHECR total trajectory length.

To summarize, both galactic and extragalactic magnetic field considerably affect the propagation of charged UHECR, misrepresenting their arrival directions and thus complicating the direct search for their sources. In this regard, gamma-ray and neutrino observations can provide a complementary information shedding light upon the plausible sites of UHECR origin, though direct correlations of UHECR and gamma-ray/neutrino sources might be nontrivial due to UHECR arrival time delay (2.5). In this thesis the focus of research is shifted towards the Galaxy and the GMF, correspondingly, thus not much attention is explicitly paid to the extragalactic space. However, it is not only important for the completeness of the whole picture, but can be one of the directions of the further CRE-related research.

2.5 GZK Effect and Photo-Nuclear Disintegration

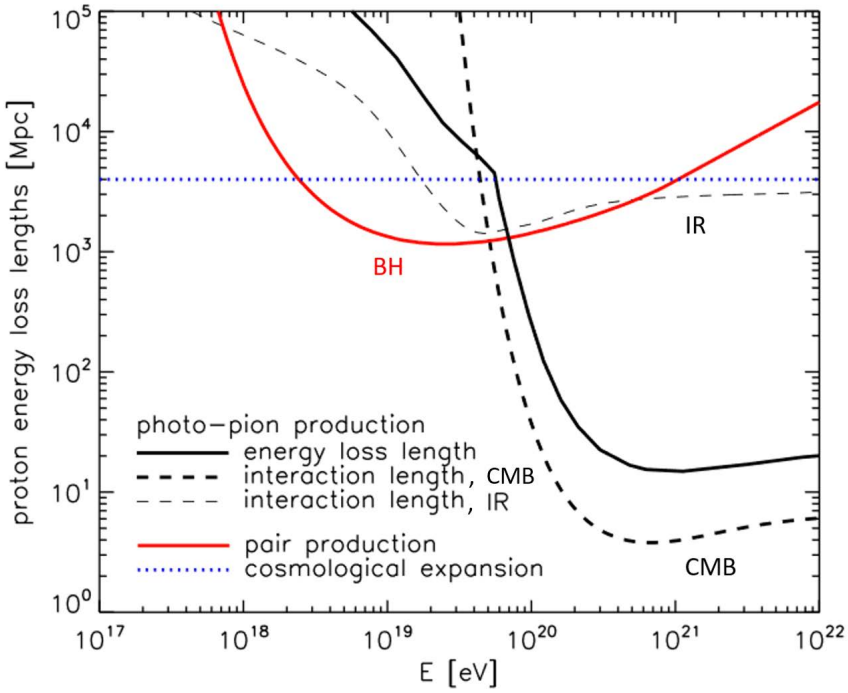

Figure 2.9: Proton energy loss lengths for the processes listed in the plot legend (IR-UV background described by the [116] model) (taken from [104]).

Apart from the adiabatic energy loss due to the expansion of the Universe, there are two important energy loss processes undergone by UHE protons: pion photo-production ($p+\gamma_{bg} \rightarrow \Delta^+ \rightarrow p+\pi^0$ or $p+\gamma_{bg} \rightarrow \Delta^+ \rightarrow n+\pi^+$) and electron-positron pair production ($p+\gamma_{bg} \rightarrow p+e^-+e^+$ Bethe-Heitler process) identical to the pair production interactions of γ–rays in the nuclear field (discussed in Section 3.1). In the context of this thesis it should be emphasized, that both phenomena could generate UHE electrons, which propagation is simulated in Chapters 6-7. These processes occur as a result of interaction of protons with background photon fields, namely, CMB, which is a remnant from an early stage of the Universe, and infrared, optical, and ultra-violet background (IR-UV) [117, 116, 118, 119, 120, 121], which is the consequence of the processes taking place in various astrophysical objects. Fig. 2.9 illustrates energy dependence of the energy loss length $L_{loss} = -\frac{1}{E}\frac{dE}{dx}$ for protons.

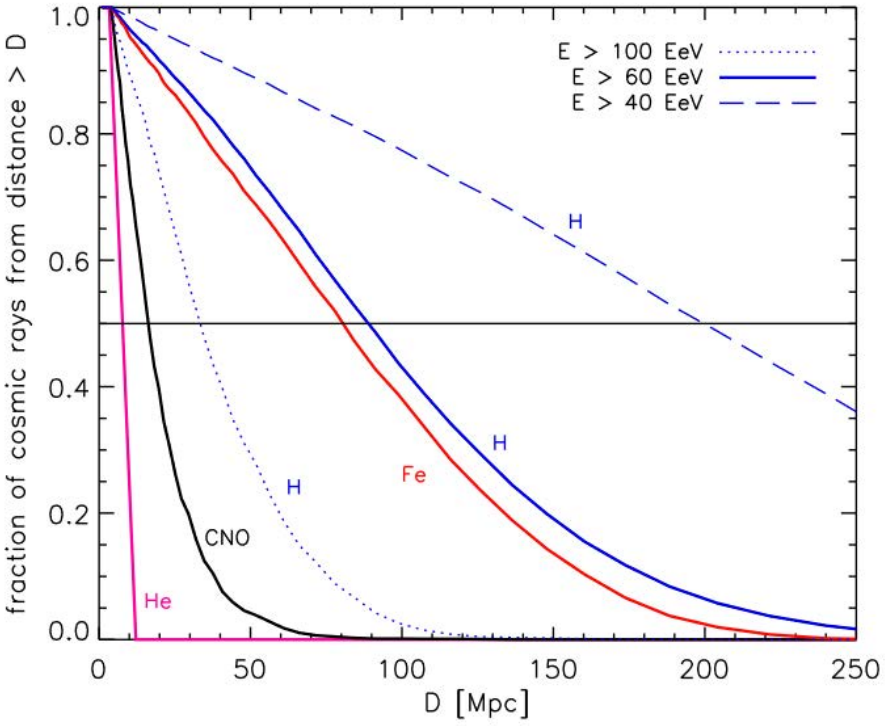

Figure 2.10: Fraction of cosmic rays that survives propagation over a distance exceeding D for protons above 40, 60 and 100 EeV and He, CNO and Fe above 60 EeV. Black solid line shows the conditions under which a half of a given species can originate (taken from [104]).

One can see, that starting from ∼50 EeV, the distance that particles can travel without losing their energy, significantly reduces. It imposes the suppression of the flux of cosmic rays with higher energies, arriving from the cosmological distances, the phenomenon known as the GZK-effect (or GZK-cutoff) and named after the authors predicting it [7, 8]. It constraints the distances to the sources of the highest-energy protons, predicting

they should be located within the Local Universe, within a distance $\leq L_{loss}(E)$.

Nuclei with the charge number $Z > 1$, in addition to the already discussed proton interactions, may suffer energy loss via photodisintegration mechanism, introduced in [122]. As follows from the name of the scenario, the nucleus interacts with background photons producing nucleons and lighter nuclei. The intermediate mass nuclei lose their energy via photodisintegration faster, than the iron nuclei (Fig. 2.10), which can lead to observation of the mixed (p-Fe) composition of UHECR at the highest energies.

Chapter 3

Electromagnetic cascades

While propagating through space, high energy photons and electrons interact with matter, low energy radiation fields, such as cosmic microwave background, and get affected by the magnetic fields, thus initiating electromagnetic (EM) cascades. In the absence of magnetic field the development of EM cascades is defined by the interplay of two main processes, the electron-positron pair production (PP; $\gamma\gamma_{bg} \to e^- e^+$), and ICS ($e\gamma_{bg} \to e'\gamma$). For UHE photons, when scattering occurs in the quantum regime, almost all initial energy is carried out either by an electron or by a positron of the newborn pair. Then the electron (positron) typically loses around 90% of its energy in an ICS event which causes the background photon to get the energy comparable to that of the primary UHE photon [123]. In the EGMF such a chain of energy transitions repeats itself until the energy loss caused by synchrotron radiation prevails the ICS rate, and the cascade development gets suppressed.

Under certain conditions the higher order QED processes, such as double pair production ($\gamma\gamma_{bg} \to e^- e^+ e^- e^+$) [124, 125, 126], triplet pair production ($e\gamma_{bg} \to e e^- e^+$) [127] and photon splitting in the presence of an intense magnetic field ([128], [129]) should be also taken into account since they can affect the formation and development of EM cascades when the correspondent rates become comparable to those of the PP and ICS.

3.1 Interactions of high energy photons

The main interactions of photons with atomic nuclei, electrons and atoms are photoelectric absorption, Compton effect and electron-positron pair production. The effect caused by each of these processes depends on the photon energy and thus the observations performed in different spectral ranges allow studying different astrophysics environments.

- Photoelectric absorption

  This process is dominant for low photon energies, $\hbar\omega \ll m_e c^2$. In case the energy of the incident photon exceeds the binding energy of the atom, the electron from the

corresponding level is likely to absorb the photon energy and be ejected from the atom. The minimal energy needed for such an event defines the low ("absorption") edge of the spectrum. The absorption cross-section for the ejection of electrons from the K-shells of atoms is calculated analytically:

$$\sigma_K = \frac{e^{12} m_e^{3/2} Z^5}{192\sqrt{2}\pi^5 \varepsilon_0^6 \hbar^4 c} \left(\frac{1}{\hbar\omega}\right)^{7/2}, \tag{3.1}$$

with Z standing for the atomic number of the nucleus. Such a strong dependence on Z means a non-negligible contribution of heavier elements to the total absorption cross-section despite their lower abundances. Thus, they should be accounted for when estimating the total cross-section in an accurate way.

- Compton scattering

  This effect is known as the increase of the photon wavelength because of the scattering from a free electron, in other words, the energy transfer from the photon to the "recoil" electron. The corresponding total cross-section is given by the Klein-Nishina formula:

$$\sigma_{K-N} = \pi r_e^2 \frac{1}{x} \left\{ \left[1 - \frac{2\,(x+1)}{x^2}\right] \ln(2x+1) + \frac{1}{2} + \frac{4}{x} - \frac{1}{2\,(2x+1)^2} \right\}, \tag{3.2}$$

  where $x = \hbar\omega/m_e c^2$, $r_e^2 = e^2/4\pi\varepsilon_0 m_e c^2$ is the classical electron radius. In the ultra-relativistic limit the Klein-Nishina cross-section is

$$\sigma_{K-N} = \pi r_e^2 \frac{1}{x} \left(\ln 2x + \frac{1}{2}\right), \tag{3.3}$$

  so that the cross-section roughly falls off as x^{-1} at the largest energies. For an atom with Z electrons the total cross-section per atom is $Z\sigma_{K-N}$, whereas the nuclei contribution is negligibly small compared to that of the electrons.

- $e^- e^+$ pair production

  This process is possible in case the photon energy is higher than the sum of the rest mass energies of an electron and a positron, $E_\gamma \geq 2m_e c^2$. For high photon energies (MeV and more) it dominates over two other processes, mentioned above. Pair production can occur in the field of a nucleus; for intermediate photon energies $1 \ll \hbar\omega/m_e c^2 \ll \alpha_{em} Z^{1/3}$ the cross-section is estimated as

$$\sigma_{PP} = \alpha_{em} r_e^2 Z^2 \left[\frac{28}{9} \ln\left(\frac{2\hbar\omega}{m_e c^2}\right) - \frac{218}{27}\right] m^2/\text{ atom}, \tag{3.4}$$

while the cross-section for the ultrarelativistic photon is

$$\sigma_{PP} = \alpha_{em} r_e^2 Z^2 \left[\frac{28}{9} \ln \left(\frac{183}{Z^{1/3}} \right) - \frac{2}{27} \right] m^2/ \text{ atom}, \tag{3.5}$$

where $\alpha_{em} \simeq 1/137$ is the fine structure constant. One can notice that the cross-section for the pair production via the interactions of photons with electrons is negligibly smaller and can thus be not taken into account.

Another phenomenon leading to the conversion of a photon into an e^-/e^+ pair is the so-called magnetic pair production [130, 131, 132]. It was shown that for the photon energies even well in excess of threshold ($\hbar\omega = 2m_e c^2$) extremely high values of magnetic field strength ($B > 10^9$ G) were required to provide a non-zero conversion rate. For the limit of high photon energies the probability of an e^-/e^+ pair creation over a finite distance of propagation R is

$$P_{conv}(R) = 1 - exp \left[- \int_0^R \alpha(\chi(r))\, dr \right], \tag{3.6}$$

where $\alpha(\chi) = (\alpha_{em} m_e c/2\hbar)(B_{tr}/B_{cr})T(\chi)$, $\chi = (h\nu/2m_e c^2)(B_{tr}/B_{cr})$, B_{tr} is the transverse to the photon momentum magnetic field component, $B_{cr} = m_e^2 c^3/e\hbar = 4.414 \cdot 10^{13}$ G is the quantum critical value of magnetic field strength [133] and $T(\chi)$ is the magnetic pair production function. The latter can be approximated in terms of the modified Bessel functions as $T(\chi) \cong 0.16\chi^{-1} K_{1/3}^2 \left(\frac{2}{3\chi} \right)$. The calculations allowed to conclude that despite every photon with the energy above the threshold is not kinematically restricted to produce a pair, the conversion probability rate is negligible unless $\chi \geq 0.1$, and increases with the strength of the magnetic field.

3.2 Energy loss processes for high energy electrons

Once an electron-positron pair is produced, the electrons can undergo a number of energy loss processes on their way through the interstellar medium, as they interact with matter, radiation and magnetic fields. Some of these interactions are favourable for the emission of photons with the energies high enough to produce a consecutive $e^- e^+$ pair, etc., which leads to an EM cascade formation. The electron energy is lost in the following cases:

- Ionization losses - occur as a result of interactions of the electrons with the neutral atoms. For example, the loss rate for atomic hydrogen case is

$$- \left(\frac{dE}{dt} \right)_i = 7.64 \times 10^{-15} n \left(3 ln\gamma + 19.8 \right) \text{ eV } s^{-1}, \tag{3.7}$$

where γ is the Lorentz factor of the electron and n is the concentration of hydrogen. As one can see, the energy dependence of the energy loss rate is logarithmic.

- Bremsstrahlung - the losses resulting from the deceleration of the electron interacting with the nuclei. The correspondent loss rate can be written as

$$-\frac{1}{E}\left(\frac{dE}{dt}\right)_{Brem} = 4nZ^2 r_e^2 \alpha_{em} c\bar{g}, \tag{3.8}$$

with $\bar{g}$ standing for a Gaunt factor. In fully ionized plasma $\bar{g} = \ln\gamma + 0.36$, making the energy loss rate

$$-\frac{1}{E}\left(\frac{dE}{dt}\right)_{Brem} = 7.0 \times 10^{-23} n \left(\ln\gamma + 0.36\right) s^{-1}, \tag{3.9}$$

while for the neutral hydrogen (the energy is lost in the interactions of the electrons with the nuclei of the atoms) $\bar{g} = ln\left(183Z^{-1/3}\right) - \frac{1}{18}$, and the loss rate becomes

$$-\frac{1}{E}\left(\frac{dE}{dt}\right)_{Brem} = 3.66 \times 10^{-22} n \ s^{-1}. \tag{3.10}$$

It is noticeable that the energy loss rate is proportional to the electron energy in both cases.

- Adiabatic losses - occur in case the electrons are confined within en expanding volume. The energy loss rate for a uniformly expanding sphere of the R radius is, for example,

$$-\frac{1}{E}\left(\frac{dE}{dt}\right)_{ad} = \frac{1}{R}\left(\frac{dR}{dt}\right). \tag{3.11}$$

Adiabatic losses are important in case the electrons are always confined within the source during its expansion.

- Inverse Compton scattering - results from the propagation of an ultrarelativistic electron in a low energy radiation field. The term "inverse Compton scattering" reflects the situation when the electron loses its energy interacting with a low energy photon, whereas the "traditional" Compton scattering reflects the situation when a high energy photons scatters off the electron, transmitting energy to the latter. The energy loss rate for the IRC is

$$-\left(\frac{dE}{dt}\right)_{ICS} = \frac{4}{3}\sigma_T c \gamma^2 U_{rad}, \tag{3.12}$$

where U_{rad} is the energy density of the radiation field.

- Synchrotron radiation, highlighted in 3.3, is characterized by the energy loss rate

proportional to E^2:

$$-\left(\frac{dE}{dt}\right)_{synch} = 6.6 \times 10^4 \gamma^2 B^2 \text{ eV } s^{-1}. \tag{3.13}$$

3.3 Synchrotron radiation

An accelerated charged particle emits electromagnetic radiation. In case the particle acceleration is a result of its propagation in the magnetic field, radiation is called "synchrotron radiation", deriving its name from synchrotrons, in which this type of radiation was discovered in 1946 and then described in 1947 [134]. Such a phenomenon is typical in astrophysics environments due to the presence of magnetic fields, and thus is of particular interest for this work, since it is one of the main processes leading to formation and propagation of the electromagnetic particle cascades in space initiated by UHE photons and electrons.

The electromagnetic field of a moving particle of mass m and electric charge q can be written in a non-covariant form as follows [135]:

$$\vec{E}\left(\vec{r},t\right) = \frac{1}{4\pi\varepsilon_0}\left(\frac{q\left(\vec{n}-\vec{\beta}\right)}{\gamma^2\left(1-\vec{n}\cdot\vec{\beta}\right)^3 R\left(t'\right)^2} + \frac{q\vec{n}\times\left(\left(\vec{n}-\vec{\beta}\right)\times\dot{\vec{\beta}}\right)}{c\left(1-\vec{n}\cdot\vec{\beta}\right)^3 R\left(t'\right)}\right)_{t'} \tag{3.14}$$

$$\vec{B}\left(\vec{r},t\right) = \frac{\mu_0}{4\pi}\left(\frac{qc\left(\vec{\beta}\times\vec{n}\right)}{\gamma^2\left(1-\vec{n}\cdot\vec{\beta}\right)^3 R\left(t'\right)^2} + \frac{q\vec{n}\times\left(\vec{n}\times\left(\left(\vec{n}-\vec{\beta}\right)\times\dot{\vec{\beta}}\right)\right)}{\left(1-\vec{n}\cdot\vec{\beta}\right)^3 R\left(t'\right)}\right)_{t'} \tag{3.15}$$

where $\beta = \frac{v(t')}{c}$ is the relative to the speed of light particle velocity, $\gamma = \frac{1}{\sqrt{1-|\beta(t')|^2}}$ (the Lorentz factor), $\vec{R}\left(t'\right) = \vec{r} - \vec{r_0}\left(t'\right)$ is the distance from the charge, $R\left(t'\right) = |\vec{R}\left(t'\right)|$, $\vec{n}\left(t'\right) = \frac{\vec{R}(t')}{R(t')}$ is the unit vector between the observation point and the position of the charge at the retarded time t'. The latter is understood as the time when the field actually started to propagate, taking into account the delay needed for the field to reach from the point of its emission (defined by $\vec{r_0}$ to the observer (located at $\vec{r}$), written as $t' = t - \frac{|\vec{r}-\vec{r_0}|}{c}$).

The first terms in each field expression are proportional to R^{-2} and do not depend on the particle acceleration (velocity fields). They are also called generalized Coulomb fields, since they could be obtained from the Lorentz transformation of the static Coulomb field as well. The second terms (acceleration fields) depend linearly on $\dot{\vec{\beta}}$, and fall off as R^{-1}. The latter are typical radiation fields with both $\vec{E}$ and $\vec{B}$ being transverse to the

radius vector, and represent electromagnetic radiation. For derivation of the important characteristics of radiation the first terms in (3.14) and (3.15) can be omitted.

The radial component of Poynting's vector is:

$$\left[\vec{S}\cdot\vec{n}\right] = \frac{q^2}{16\pi^2\varepsilon_0 c}\left\{\frac{1}{R^2}\frac{|\vec{n}\times\left[\left(\vec{n}-\vec{\beta}\right)\times\dot{\vec{\beta}}\right]|^2}{|\left(1-\vec{n}\cdot\vec{\beta}\right)|^3}\right\}_{t'}, \tag{3.16}$$

from where one can derive that the power radiated per unit solid angle is

$$\frac{dP}{d\Omega} = \frac{q^2}{16\pi^2\varepsilon_0 c}\frac{|\vec{n}\left(t'\right)\times\left[\left(\vec{n}\left(t'\right)-\vec{\beta}\left(t'\right)\right)\times\dot{\vec{\beta}}\right]|^2}{\left(1-\vec{n}\left(t'\right)\cdot\vec{\beta}\left(t'\right)\right)^5}, \tag{3.17}$$

and after the integration over the solid angle the total power radiated can be written

$$P = \frac{q^2}{6\pi\varepsilon_0 c}\gamma^6\left[|\dot{\vec{\beta}}|^2 - |\vec{\beta}\times\dot{\vec{\beta}}|^2\right]. \tag{3.18}$$

The latter expression is known as the relativistic generalization of Larmor's formula.

Application of (3.18) to the analysis of a charged particle motion along the bended trajectory, which is the general case for, e.g., cosmic magnetic fields, allows to write down the power radiated in an entire solid angle as

$$P = \frac{q^2}{6\pi\varepsilon_0 c}|\dot{\vec{\beta}}|^2\gamma^4 = \frac{q^2 c}{6\pi\varepsilon_0}\frac{\beta^4\gamma^4}{\rho^2}, \tag{3.19}$$

where ρ is the particle gyroradius.

Thus the emitted power scales as $\left(\frac{E}{m}\right)^4$, and decreases with the square of the radius of the orbit. The former fact means that the emission of synchrotron radiation by electrons leads to a lot faster energy loss than in case of the other (heavier) charged particles.

The study of angular distribution of synchrotron radiation with respect to the direction of the particle momentum allows for making another important conclusion. Analysis of (3.16) indicates that there are two types of relativistic effects affecting the emission of radiation by a moving charge. One of them is that the mutual orientation of $\vec{\beta}$ and $\dot{\vec{\beta}}$ determines the detailed angular power distribution. The other arises from the relativistic effect of transforming from the rest frame of the particle to the observer's frame. It is expressed by the factor $\left(1-\vec{n}\cdot\vec{\beta}\right)$ in the denominator of (3.16), and dominates the whole angular distribution in case of ultra-relativistic particles.

In case of a moving charge with velocity $\vec{\beta}$ perpendicular to its acceleration $\dot{\vec{\beta}}$, the general expression (3.17) for the angular distribution of radiation reduces to

$$\frac{dP}{d\Omega} = \frac{q^2}{16\pi^2\varepsilon_0 c}\frac{|\dot{\vec{\beta}}|^2}{\left(1-\beta\cos\theta\right)^3}\left[1-\frac{\sin^2\theta\cos^2\gamma}{\gamma^2\left(1-\beta\cos\theta\right)^2}\right], \tag{3.20}$$

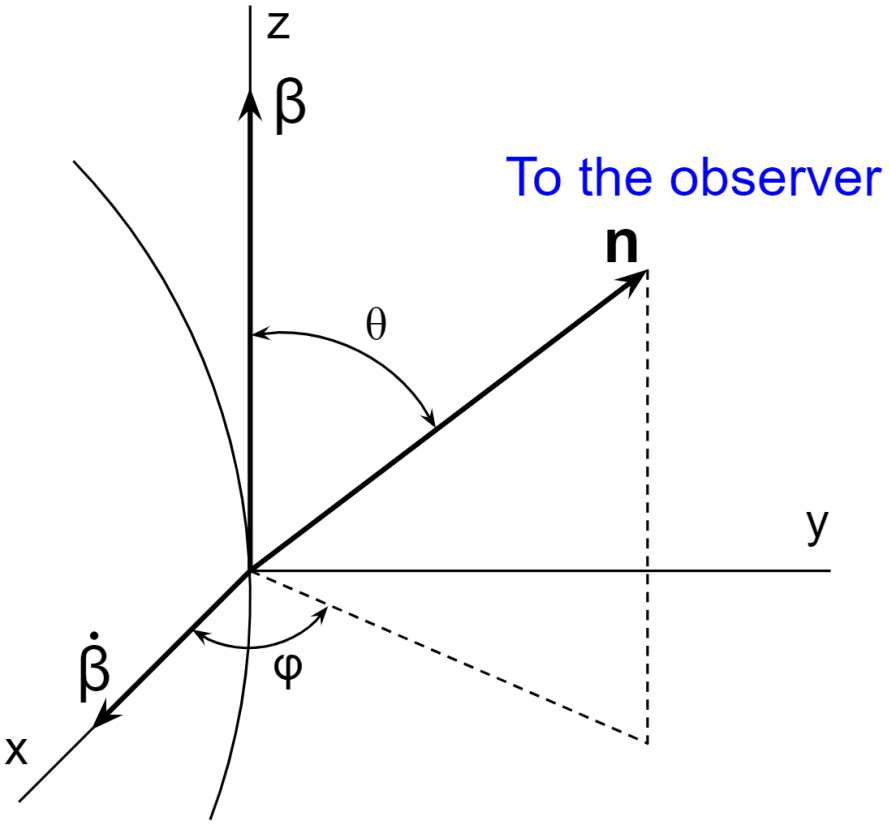

Figure 3.1: A charged particle in the spherical coordinate system; $\vec{\beta}$ and $\dot{\vec{\beta}}$ are the charge velocity and acceleration, correspondingly.

where θ and γ are polar angles defining the direction to the observer, as shown in Fig. 3.1.

In a relativistic case, i.e. when $\beta \to 1$, due to the factor $(1 - \beta\cos\theta)$ in the denominator of (3.20) the angular distribution is tipped forward into a narrow cone like the beam of a headlight pointing ahead of the particle. The angle $\theta_{\max}$ for which the intensity is maximal is

$$\theta_{\max} \to \frac{1}{2\gamma}, \tag{3.21}$$

and the RMS angle of the emission of radiation is

$$\theta_{RMS} = \frac{1}{\gamma} = \frac{mc^2}{E}, \tag{3.22}$$

where mc^2 is the rest energy of the particle, E is its total energy.

Such a confinement of the synchrotron radiation makes an observer able to detect it only as a consequence of short pulses (the radiation is visible when directed towards the observer) of time duration $T = \frac{L}{c}$, occurring at regular intervals $T_0 = \frac{L_0}{c}$, where $L = \frac{\rho}{2\gamma^3}$, with ρ being the gyroradius of the charge trajectory (Fig. 3.2). Fourier decomposition of

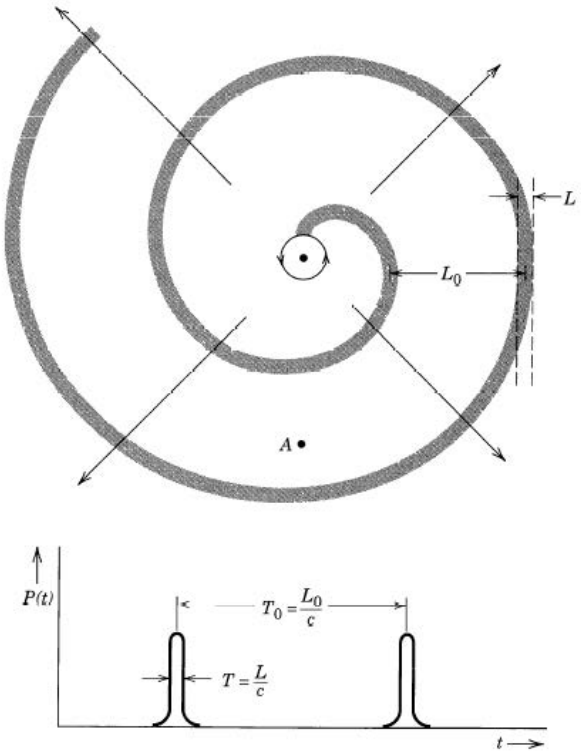

Figure 3.2: Radiation pattern emitted by a relativistic particle during its periodic motion (taken from [135]).

the finite wave package shows that radiation spectrum will contain the frequency components up to some critical value,

$$\omega_c \sim \frac{c}{L} \sim \left(\frac{c}{\rho}\right)\gamma^3. \tag{3.23}$$

This can be proven by analyzing the frequency distribution in the spectrum of synchrotron radiation. Angular and frequency distribution of the energy received by an observer can be written as

$$\frac{d^2I}{d\Omega dt} = \frac{q^2}{16\pi^3\varepsilon_0 c}\left|\int_{-\infty}^{+\infty} \frac{\vec{n}\times\left[\left(\vec{n}-\vec{\beta}\right)\times\dot{\vec{\beta}}\right]}{\left(1-\vec{n}\cdot\vec{\beta}\right)^2} e^{i\omega(t-\vec{n}\cdot\vec{r}(t)/c)}dt\right|^2, \tag{3.24}$$

the formula known as the radiation integral. After non-trivial calculations of (3.24) for a charge moving along the instantaneous arc, the energy radiated per unit frequency interval per unit solid angle is

$$\frac{d^2I}{d\Omega dt} = \frac{q^2}{12\pi^3\varepsilon_0 c}\left(\frac{\omega\rho}{c}\right)^2\left(\frac{1}{\gamma^2}+\theta^2\right)^2\left[K_{2/3}^2(\xi)+\frac{\theta^2}{(1/\gamma^2)+\theta^2}K_{1/3}^2(\xi)\right], \tag{3.25}$$

where the function K is a modified Bessel function of the second kind,

$$\xi = \frac{\omega\rho}{3c}\left(\frac{1}{\gamma^2} + \theta^2\right)^{3/2} \tag{3.26}$$

with θ standing for the angle between the direction to the observer and the arc. The terms in the square brackets correspond to different polarizations of the radiation (in-plane of the orbit and normal to that plane, correspondingly).

From the properties of Bessel functions it is known that the intensity of radiation is negligible for $\xi \gg 1$ (at large angles; the greater the frequency, the smaller the critical angle beyond which the radiation is negligible). This means that the radiation is mostly confined to the plane where the motion of the charged particle takes place, being confined more the higher the frequency is. For high values of ω the parameter ξ also becomes large for all angles, and thus the total energy emitted at that frequency is negligible. The critical frequency beyond which the radiation at any angle is negligible is defined from the condition $\xi = 0.5$ for $\theta = 0$:

$$\omega_c = \frac{3}{2}\gamma^3\left(\frac{c}{\rho}\right) \tag{3.27}$$

The angular spread at a certain frequency is estimated by the critical angle θ_c at which

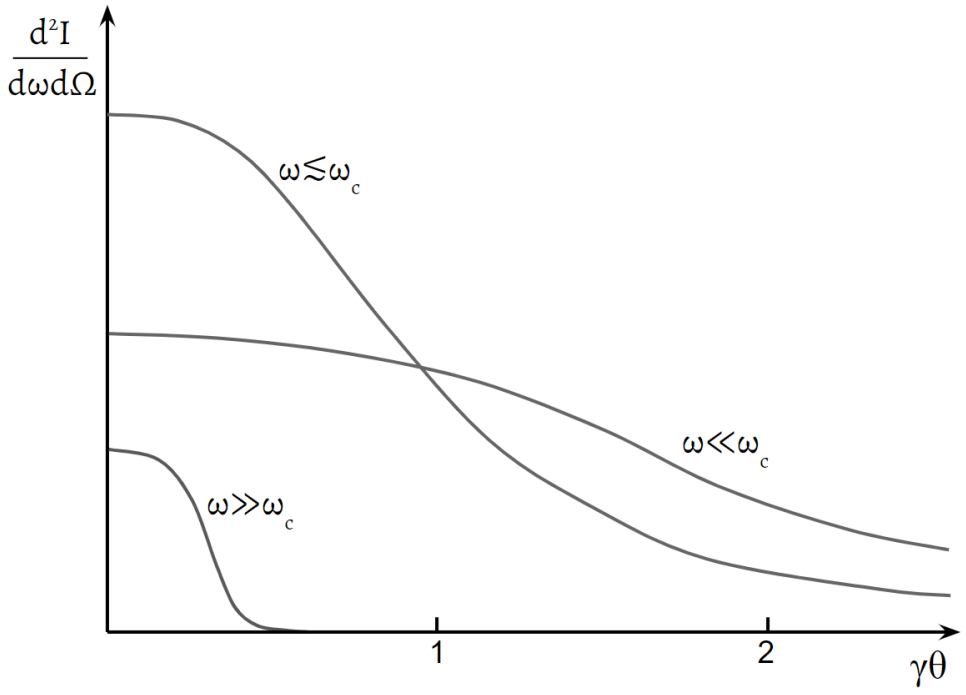

Figure 3.3: Differential frequency spectrum as a function of angle [135]. For $\omega \leq \omega_c$ the radiation is confined to angles of the order of γ^{-1}, for much smaller (higher) frequencies the confinement is larger (smaller).

$\xi(\theta_c) \simeq \xi(0) + 1$. If $\omega \ll \omega_c$, $\xi(\theta_c) \simeq 1$, and

$$\theta_c = \frac{1}{\gamma}\left(\frac{2\omega_c}{\omega}\right)^{1/3} \tag{3.28}$$

Fig. 3.3 demonstrates the angular distribution of radiation for different frequency ranges. The frequency distribution of the total radiated energy can be obtained by integration of (3.24) over all angles. The result can be written as:

$$\frac{dI}{d\omega} = \frac{\sqrt{3}e^2}{4\pi\varepsilon_0 c}\gamma\frac{\omega}{\omega_c}\int_{\omega/\omega_c}^{\infty} K_{5/3}(x)\,dx \tag{3.29}$$

In terms of photons the synchrotron radiation can be treated keeping in mind the expression for the energy of a photon $\varepsilon = \hbar\omega$. The critical photon energy in this language is defined as

$$\varepsilon_c = \hbar\omega_c = \frac{3\hbar c}{2\rho}\gamma^3 \tag{3.30}$$

The higher this value is, the more photons with high energies are generated.

3.4 Examples of EM cascades

The notion of CRE, proposed by the CREDO Collaboration [17], refers to all possible cosmic-ray cascades, which may contain nucleons, electrons, neutrinos, photons etc. In this thesis the focus is made on EM cascades, which constitute a specific sub-class of CRE. The processes of energy conversion between the particles forming EM cascades (photons and electrons), as it can be seen from the energy loss rates provided in the previous subsections of this chapter, depend on the particles energy as well as on the strength of the magnetic field in the regions the propagation takes place. Though the geomagnetic and Solar magnetic field values are relatively low, the UHE photons can still undergo cascading under these conditions and thus one can expect EM cascades to be initiated at the vicinity of the Sun as well as in the magnetic field of the Earth.

3.4.1 Preshowers in the geomagnetic field

One of the illustrative examples of EM cascades is the so-called preshower effect [130, 136]. It is associated with the UHE photon undergoing e^-e^+ pair production in the geomagnetic field above the Earth atmosphere with the subsequent synchrotron emission by the pair components. The name of the phenomenon is related to the processes it comprises, namely "pre" denoting the localization of the initiating process, i.e. above the atmosphere, and "shower" meaning the cascading of the primary UHE photon (Fig. 3.4).

Due to the fact that it is the transverse component of the magnetic field that affects

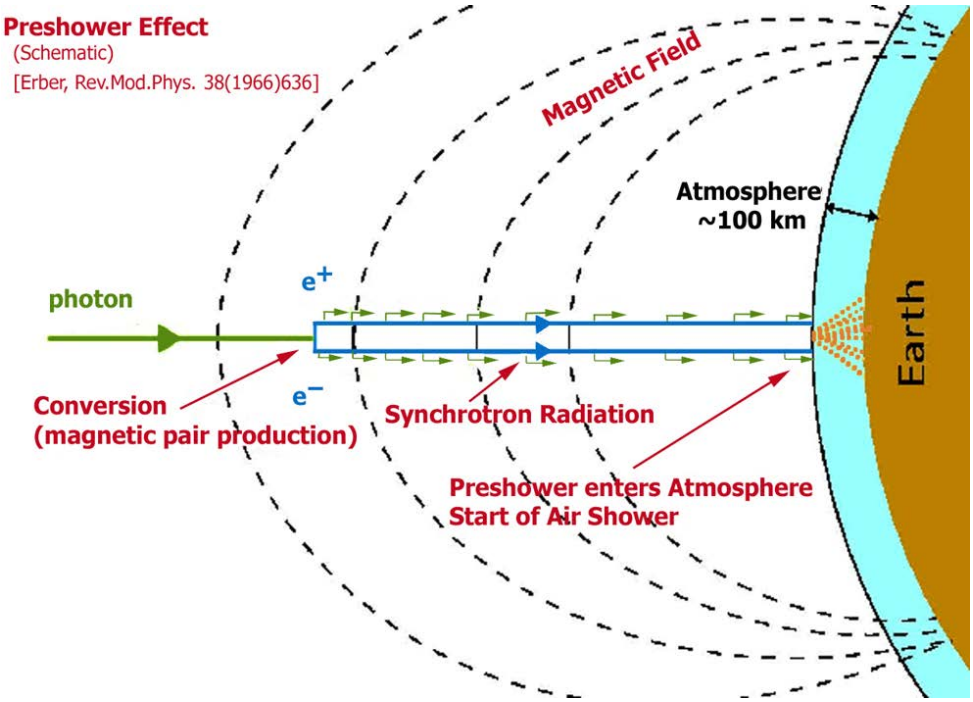

Figure 3.4: A schematic illustration of the preshower effect (taken from [130]).

the conversion probability, the development of a preshower, starting with the first pair production event, strongly depends on the way of a primary UHE photon through the magnetosphere. It also imposes the dependence of the cascade characteristics on the incident angle making the preshower effect more significant for large zenith angles of the incoming photons in the magnetic equator plane [137].

A typical preshower [138] initiated by a 10^{20} eV photon starts at around 1000 km a.s.l. Since the distance to the top of the atmosphere is typically of the order of several radiation lengths, the cascade gets developed and as a result enters the atmosphere (around 100 km a.s.l.) with hundreds of photons and a few e^-e^+ pairs of typical energies at the EeV scale. The values of photon energies span several orders of magnitude, with the largest around 10^{19} eV. Large fluctuations around these average numbers may take place, especially in case the UHE photon is converted into a pair closer to the Earth. As far as spatial extent of a typical preshower is concerned, it is expected to be very small. In a EeV energy range the angular spread of particles is $\Delta\theta \simeq m_e/E \sim 10^{-12}$, which even for the longest distances $\sim 10^4$ km from the initiation point to the Earth results in $\Delta x \simeq 10^{-3}$ cm linear deflections on top of the atmosphere [136]. The resultant atmospheric showers have properties very similar to those induced by single CRs, which complicates their identification with traditional methods .

Extensive studies of the preshower effect in order to discriminate its consequences from those of individual extensive air showers were performed in [139]. As a result of studying the energy and directional dependencies of the simulated cascades at the CTA-

North site, an efficient method of preshower/hadron separation was developed. With its use the predictions of the expected preshower rate according to different models of the production of UHE photons were made, and despite the low numbers obtained, it was concluded that the IACT technique can be used to probe physical phenomena not only in the TeV domain, but also in the EeV regime.

3.4.2 Sun super-preshowers

The effect of the cascading of a UHE photon can also take place in the Solar magnetic field. Its component, transverse to the photon propagation direction, can be strong enough to cause the creation of an e^-e^+ pair relatively close to the Sun. Synchrotron emission of the electrons also takes place mostly in these regions, thus the close vicinity of the Sun defines the development of the EM cascade. In [140] it is demonstrated that the typical strength of the transverse Solar magnetic field exceeds that of the geomagnetic field roughly by an order of magnitude. This allows to expect the correspondent energies of the photons favorable to cascading to be of the order of 10^{19} eV. Also the relation between the impact parameters of the Sun, i.e. the distances from its center at which the formation of a cascade takes place, and the photon energies initiating it, was investigated. The size and shape of the footprint, formed by the secondary photons of the Sun EM cascade on top of the Earth atmosphere, were estimated. The footprint was expected to be a very prolate ellipse elongated tens of kilometers in the direction perpendicular to the Sun magnetic field in the region of the cascade formation.

More recently, a complementary study of the Sun cosmic-ray ensembles with the use of PRESHOWER code, was performed [141]. To generalize the notion "preshower", the term "super-preshower" (SPS) was introduced, to denote an EM cascade originating above the Earth's atmosphere, regardless of the initiating process and distance to the Earth. The investigation of the Sun SPS properties included comparison of two models of the Solar magnetic field, the dipole model with the dipole magnetic moment 6.87×10^{32} G$\cdot cm^3$ used in the pioneer paper, and the dipole-quadruple-current-sheet model, proposed in [142]. The latter one is more realistic and provides a better description of the Solar magnetic field farther from the Sun, which was useful for the cited research when tracking the electrons of the cascades on their ways towards the Earth. Another improvement was made for calculating the synchrotron photons angular distribution, introducing the half-opening angle defined by Eq. 3.22.

The dependence of the photon conversion probability on the Sun impact parameter is shown in Fig. 3.5 for different initial energies. One can see that very close to the Sun (around $1R_\odot$) even the photons with energies 1 EeV can undergo successful conversion, while for 10 EeV photons conversion probability is close to unity for the distances around $2R_\odot$. At the same time nearly all the photons with energies 100 EeV can still produce a

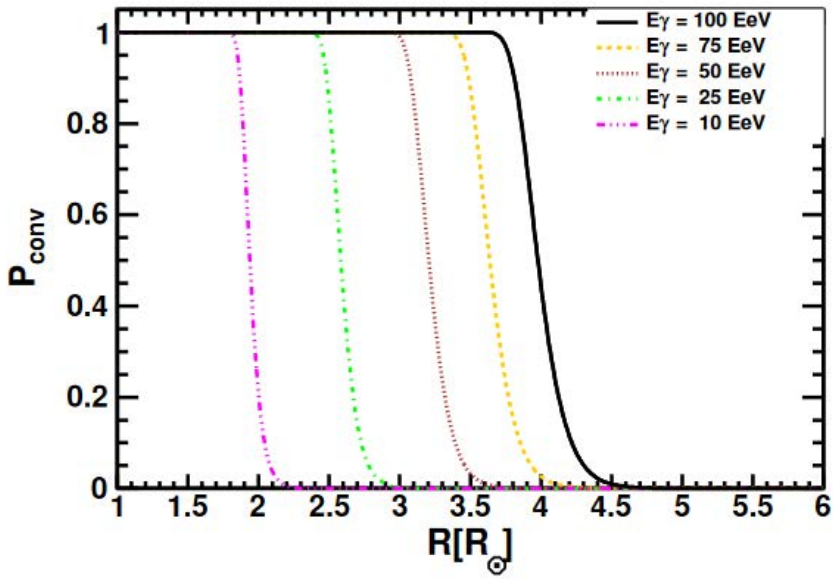

Figure 3.5: Probability of magnetic pair production as a function of the impact parameter for UHE photons heading towards the Earth from the Sun's vicinity (taken from [141]).

pair even at distances up to $4R_{\odot}$ from the center of the Sun that increases the effective solid angle within which the Sun SPS should be expected to arrive to the Earth.

Since the region of the most effective synchrotron emission is also located in the vicinity of the Sun, and is small compared to the electrons gyroradii, it could be assumed that the electron and the positron from the same pair experience nearly the same magnetic field and thus emit approximately in the same plane, being deflected in the opposite directions by the Lorentz force. This results in the shape of a cascade footprint on top of the Earth atmosphere (a prolate ellipse, as it was already mentioned), which size is calculated for different heliocentric latitudes of the primary photon and shown in Fig. 3.6.

The plot is consistent with the expectations; the closer the photon approaches the Sun, the stronger field it experiences and the more deflected become the electrons of the produced pair.

Distributions of product photons in a footprint of an example SPS on top of the atmosphere are compared for different Solar magnetic field models in Fig. 3.7. The origin point corresponds to the location of the undeflected photon, whereas the Y and Z axes are directed to the East and North, respectively.

As one can see, despite the difference in the sizes and orientations of the footprints obtained for two models, they have a very elongated shape in both cases. The energy distribution of the photons on top of the atmosphere is demonstrated in Fig. 3.8, which is a zoomed in central (core) part of the cascade footprint, weighted by the energy of the secondary photons. The results are in consistency with those pointed out in [140], namely

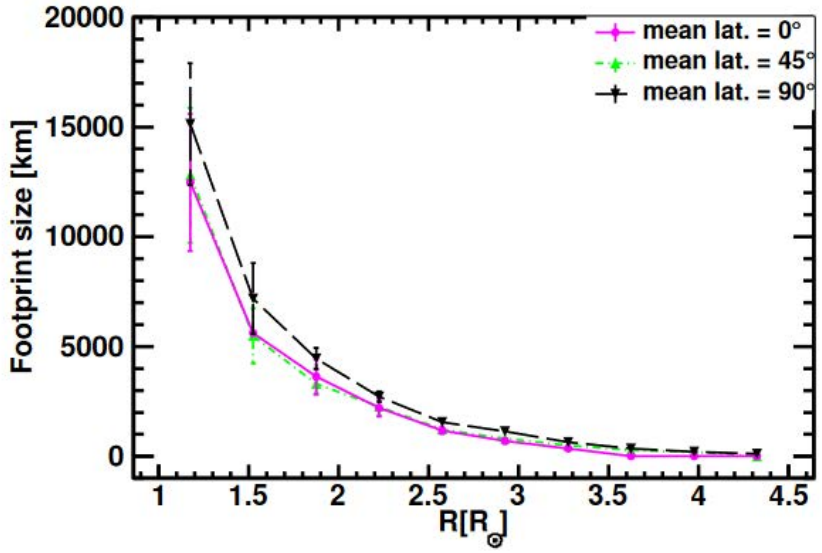

Figure 3.6: Size of a Sun SPS footprint at a distance of 1 AU from the Sun as a function of impact parameter for a 100 EeV primary photon (taken from [141]).

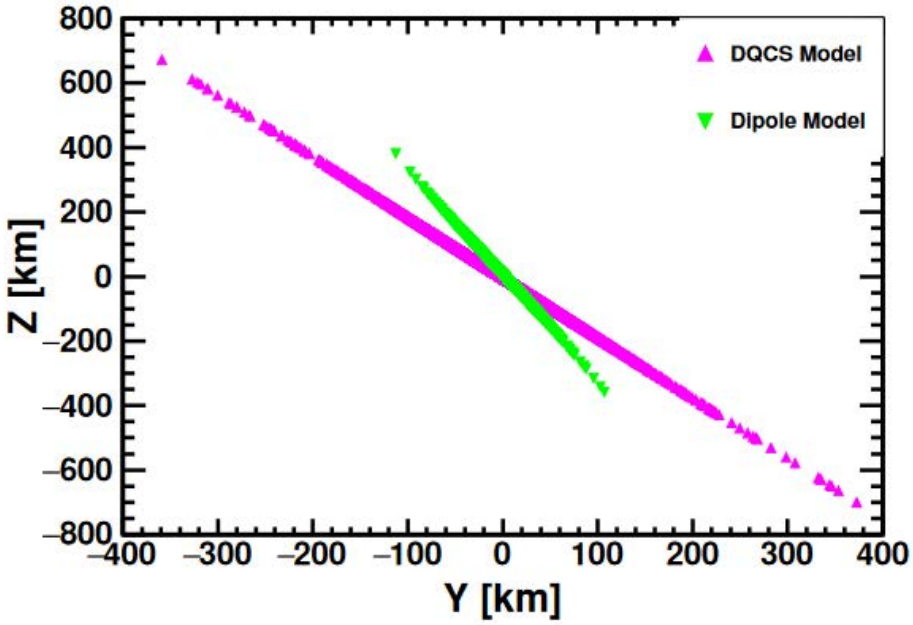

Figure 3.7: Spatial distribution of product photons with energies above 1 TeV arriving at the top of the atmosphere. The primary 100 EeV photon is directed towards the Earth such that the position of the closest approach has heliocentric latitude 45° (taken from [141]).

the photons with higher energies are located closer to the core of the footprint, i.e. the point the primary photon would have reached if unconverted into the pair.

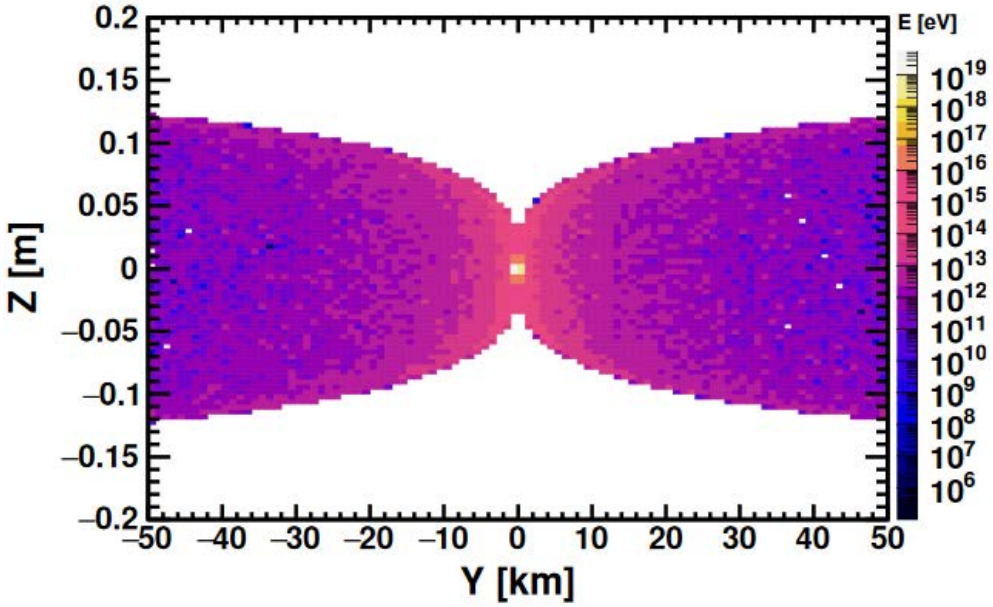

Figure 3.8: Distribution of energy of product photons arriving at the top of the atmosphere. The primary 100 EeV photon is directed towards the Earth such that the position of the closest approach has heliocentric latitude 0°, and its impact parameter is $3R_{\odot}$. Note the difference in the scales along the axes (taken from [141]).

3.4.3 Cosmic-ray ensembles and the CREDO project

As one can see from the previous examples, the production of an $e^{-}e^{+}$ pair can occur under different conditions, and together with subsequent electron energy loss processes it leads to the formation of an EM cascade. The term "cosmic-ray ensemble" denotes any group of a minimum of two correlated, be it spatially or temporally, cosmic rays with a common primary interaction vertex or the same parent particle. Schematically, the novelty of the CRE approach is demonstrated in Fig. 1.2, emphasizing the transition from a single particle in the research focus to the expression

$$N_{CR} > 1, \tag{3.31}$$

which means the correlation of the particles having a common primary, and could be regarded as the mathematical definition of a CRE. One of the main questions regarding the possible observation of the CRE is illustrated in Fig. 3.9.

It is believed that propagation of a UHE particle results in its extinction due to the interactions it undergoes on its way, thus it would be correct to ask not whether the CRE exist, but rather under which conditions they could be observed. If the photons in an EM cascade arriving at the Earth travel closely to each other, as in the preshower effect described above (3.4.1), the resultant extensive air shower will resemble the one initiated by a single primary particle. This case does not require any special infrastructure for the

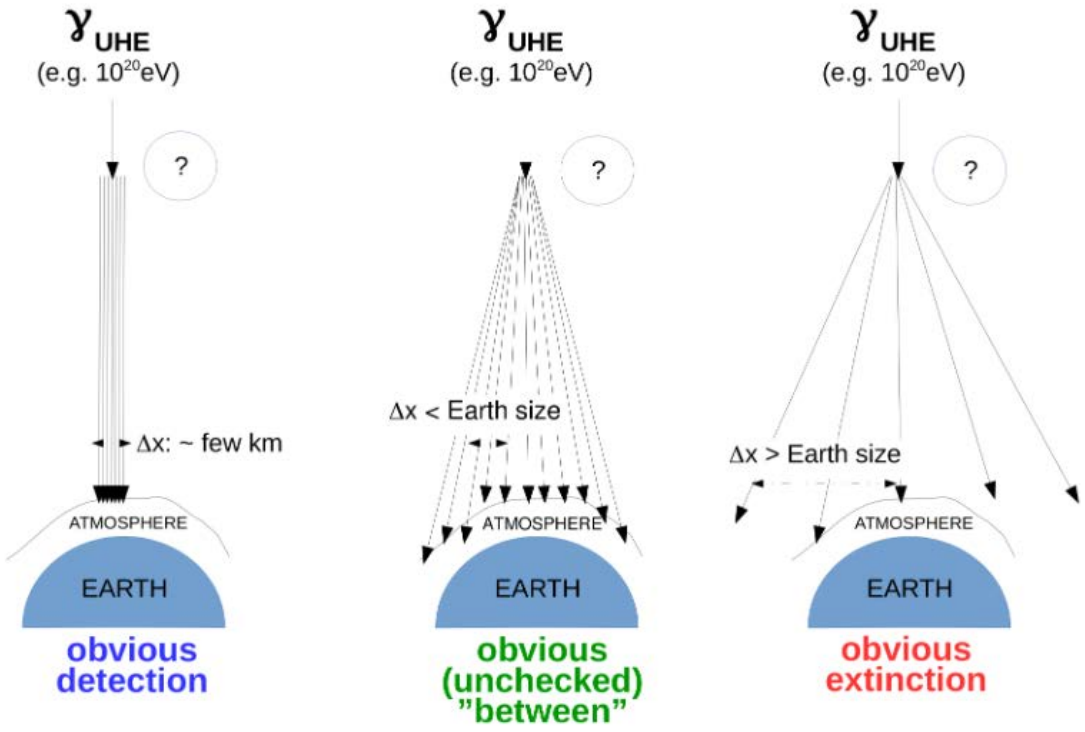

Figure 3.9: Obviously in experimental reach, although not yet probed, detection of Cosmic Ray Ensembles, using ultra-high energy photons as example primary particles (taken from [20]).

observation and is referred to as the "obvious detection" (the left panel in Fig. 3.9). The opposite extreme case is correspondent to the cascades with too sparse distribution of the components (more that the size of the Earth on average). In such a situation there is no chance to identify a particle as a part of the cascade, and one should consider this case as a limitation for the observation of CRE ("obvious extinction"; the right panel in Fig. 3.9). The central panel of the same plot, named "obvious between", illustrates what can be studied with the CRE approach - any scenarios capable to produce particle distributions less sparse than the "obvious extinction" limit. This domain is yet unexplored and requires a globally coordinated effort.

Indeed, CRE footprints can be extended up to the global scale, thus the chances of their observation increase only with the use of detector arrays of the correspondent size. For obvious reasons, building such an infrastructure from the scratch does not seem to be as an achievable goal in the nearest future. An alternative solution, proposed by the CREDO collaboration, namely, connecting as many already existing detectors as possible into a global network, looks far more promising. Data from all types of detectors, from the simplest, like smartphones and pocket scintillators, to large cosmic-ray experiments, is useful for the CREDO research, because the energies of the secondary particles constituting CRE are distributed over many orders of magnitude and thus different detectors

provide complementary information.

One of the first steps already made by the CREDO collaboration is a smartphone application, which allows to detect radiation with the camera photo sensors [143]. The particles detected might either be parts of air showers, induced by cosmic rays in the atmosphere, or result from a natural radiation background. Smartphones are already globally spread, and the number of their users is already huge and still growing, so the application induces the increase of the coverage of the smartphone detectors network. On the other hand, it fits within the strategy of a wide involvement of non-professionals into the scientific research (the so-called "citizen science"), ensuring a two-way benefit to all the participants: the scientists are helped with a manpower - the enthusiasts contribute in data acquisition and classification, while the application users get an opportunity to educate themselves, participate in scientific research and even become co-authors of scientific papers. The smartphone application data is accessible via CREDO API (open access is another feature of the CREDO project; the algorithms used for the data acquisition and analysis can be found on GitHub). This should stimulate a growing interest among the users, because everyone can easily access the results of his participation, even if it is a simple data registration, or contribute to the data analysis participating in the code development.

Examples of CREDO smartphone application data analysis are described in [144, 145, 146].

Chapter 4

Software and algorithms

4.1 Introduction to CRPropa

The main tool chosen to simulate CRE formation and propagation within this work is CRPropa 3 [147]. It is the most popular state of the art Monte Carlo code which enables simulations of behavior of different particles (nuclei, leptons, photons etc.) in an astrophysics environment, taking into account interactions with fields and matter. Its modular structure (4.1) along with the possibility of including the user written or modified modules together or instead of default ones makes it a flexible and universal instrument. Thus, CRPropa is very helpful, if not inevitable, in solving a wide range of tasks related to high-energy astrophysics. Its official website [148] provides the user with the updates, usage examples and tutorials.

The main idea of the CRPropa structure is that all the phases of a particle propagation in space as well as the processes it is involved in are realized as independent simulation modules. A cosmic ray is looped through the list of active modules *ModuleList* while they edit its state until the particle propagation is stopped on the signal sent by a module. The initial and current state of the particle is stored in the *Candidate* object, also containing information on the step size, redshift, possible interaction and status flags. The *isActive* flag serves as a break condition and is checked after each repetition of the *ModuleList* operations.

The CRPropa algorithm is steered by a simple input specification where all the modules expected to influence a particle propagation are added to the *ModuleList* and specified according to the simulation task. The input configuration contains, for example, an information on the *Candidate* (the type of primary particle, its initial energy, initial direction etc.), type of propagation (corresponding to 1D, 3D motion, propagation in magnetic field etc.), interactions with different types of cosmic backgrounds (pair production, synchrotron radiation, inverse Compton scattering etc.), stop (breaking) conditions, observer, output type and other relevant modules.

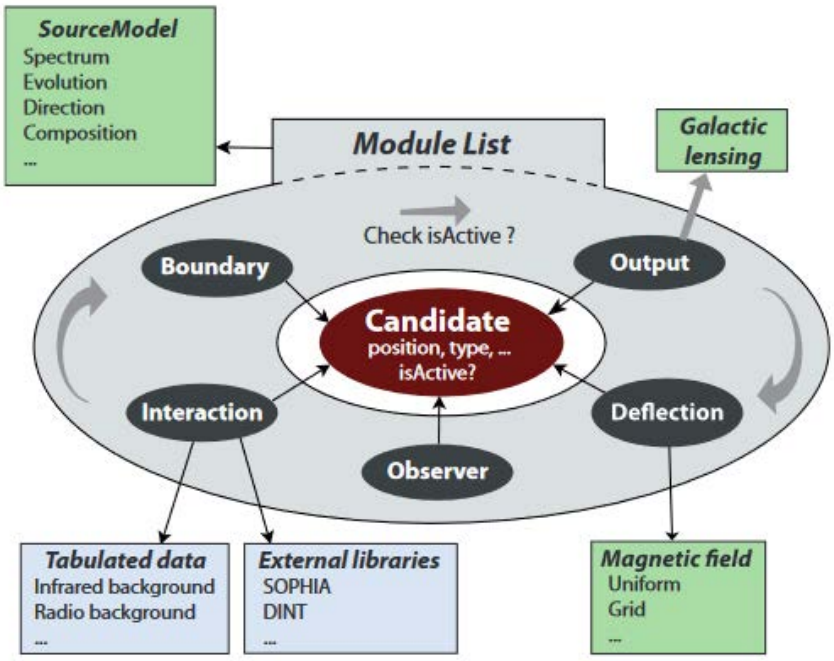

Figure 4.1: Illustration of the CRPropa 3 modular structure. Each module contained in the module list acts on the candidate class (taken from [147]).

The simulation results are saved in the output files which contain the information on propagation of the particles involved in the physical processes included in the simulation chain. The plain text output, which has been used for this work, is realized within the *TextOutput* module (another supported output type is HDF5, provided by the *HDF5Output* module). Depending on the place of the code where the output module is linked, it could be called on different steps or after meeting certain predefined conditions (breaking, due to reaching the threshold, or border ones, when the particle crosses the observer surface). Such variability ensures the efficient use of computer resources and allows obtaining one or several different output files, which makes the analysis of the simulation more complete.

Depending on the task run by the user the output can be stored in one of five presets: *Event1D*, *Event3D*, *Trajectory1D*, *Trajectory3D* and *Everything*, with different display schemes, as described below. The most complete preset of the output is *Everything*. It contains information stored in the correspondent columns of the text file. They are the following: serial number of the particle (within a particular simulation); its trajectory length; energy, ID (particle type defined in correspondence with PDG Monte Carlo particle numbering scheme [149], coordinates and momentum components calculated in current, starting (primary particle) and origin (parent particle) positions. Other presets do not display all the values listed above, but only the relevant ones. For example, *Event1D* contains trajectory length, ID's and energies in the origin and current points, *Event3D*

presumes saving current position and momentum components, as well as coordinates of the starting point, in addition to *Event1D* information. *Trajectory1D* allows to write down only ID, energy and position (a coordinate along the trajectory), while *Trajectory3D* preset includes also trajectory length, redshift, serial number, coordinates and momentum components in the current position. The described scheme of the output is convenient while studying cascades of particles, since all the information needed to track a particular particle can be retrieved easily. Additionally, fine-tuning of the output is possible, which is done by enabling or disabling one or several columns.

CRPropa uses the SI unit system by default, but most of the important units (GeV, kpc) are assigned to the correspondent symbols, which enforces expressive code, e.g. *MinimumEnergy*(1*GeV). The unit scale is chosen for every value displayed in the output independently, for instance:

- t = TextOutput(filename, Output.Everything)
- t.setLengthScale(meter)
- t.setEnergyScale(GeV)

An example output file (a fragment) is shown in Fig. A.1. The *Everything* preset is used, while some columns (the serial number, redshift, initial momentum components) are disabled. The meter scale is chosen for distances, and energy is scaled in GeV (this information is displayed in the first lines of the output file). The output module during this simulation was called to save every propagation step of every particle originated during the propagation of the primary particle.

4.2 Cash-Karp algorithm

One of the main processes to be considered while studying the formation and propagation of cosmic-ray ensembles is the synchrotron emission of a charged particle, e.g., an electron, due to its accelerated motion in the cosmic magnetic fields (Section 3.3). Propagation of the particles in space requires the solution of the ordinary differential equation (ODE) of the second order

$$\frac{d\vec{p}}{dt} = q\left(\vec{E} + \vec{v} \times \vec{B}\right), \tag{4.1}$$

where $\vec{p}$ is the particle momentum, q is its electric charge, $\vec{E}$ and $\vec{B}$ are electric and magnetic constituents of the electromagnetic field, respectively, and the right-hand side of the equation is the general expression for the Lorentz force acting on a charged particle which propagates in the electromagnetic field. Since the cosmic electromagnetic fields have a complicated structure (see e.g. 2.4.1 and 2.4.2), the analytical solution of (4.1)

represents a non-trivial, if not an impossible, task, and thus the use of numerical methods is required in order to obtain an approximate solution.

The Runge-Kutta methods (RKM) are widely used for integrating the ODE with the known initial conditions (one of the types of the Cauchy problem). They belong to the so-called one-step methods, which require only the last time point of the approximate solution, to perform the calculations of every next step. Let the initial value problem be described by the equation:

$$\frac{dy}{dt} = f\left(t, y\right), \tag{4.2}$$

where y is an unknown scalar or vector function of time t with the given initial conditions:

$$y\left(t_0\right) = y_0 \tag{4.3}$$

Originally, the scheme of the family of explicit RKM was defined as

$$y_{n+1} = y_n + h\sum_{i=1}^{s} b_i k_i, \tag{4.4}$$

where

$$\begin{aligned} k_1 &= f\left(t_n,\, \mathrm{y}_n\right) \\ k_2 &= f\left(t_n + c_2\mathrm{h},\, \mathrm{y}_n + h\left(a_{21}k_1\right)\right) \\ k_3 &= f\left(t_n + c_3\mathrm{h},\, \mathrm{y}_n + h\left(a_{31}k_1 + a_{32}k_2\right)\right) \\ k_s &= f\left(t_n + c_s\mathrm{h},\, \mathrm{y}_n + h\left(a_{s1}k_1 + a_{s2}k_2 + ... + a_{s,s-1}k_{s-1}\right)\right) \end{aligned} \tag{4.5}$$

Any particular method of the family is characterized by the number of stages s, and the Runge-Kutta matrix $a_{ij}\,(1 \le j < i \le s)$, weights $b_i \;\; (i = 1, 2, ..., s)$ and nodes $c_i\,(i = 2, 3, ..., s)$. These coefficients are arranged in the so-called Butcher tableau:

$$\begin{array}{c|ccccc} 0 & & & & & \\ c_2 & a_{21} & & & & \\ c_3 & a_{31} & a_{32} & & & \\ \vdots & \vdots & \ddots & & & \\ c_s & a_{s1} & a_{s2} & \dots & a_{s,s-1} & \\ \hline & b_1 & b_2 & \dots & b_{s,s-1} & b_s \end{array}$$

Some additional conditions should be met by the coefficients, namely

$$\begin{aligned} &\sum_{i=1}^{s} b_i = 1, \\ &\sum_{j=1}^{i-1} a_{ij} = c_i \end{aligned} \tag{4.6}$$

for $i = 2, 3, ..., s$.

The classical RKM is the method

$$\begin{aligned} y_{n+1} &= y_n + \frac{1}{6} h \left(k_1 + 2k_2 + 2k_3 + k_4\right) \\ t_{n+1} &= t_n + h \\ k_1 &= f\left(t_n, \mathrm{y}_n\right) \\ k_2 &= f\left(t_n + \frac{h}{2}, \mathrm{y}_n + h\frac{k_1}{2}\right) \\ k_3 &= f\left(t_n + \frac{h}{2}, \mathrm{y}_n + h\frac{k_2}{2}\right) \\ k_4 &= f\left(t_n + h, y_n + hk_3, \right) \end{aligned} \tag{4.7}$$

belonging to the family of methods with the fourth order of accuracy of the form (4.4) with s=4, in a sense that a local truncation error is of the order of $O\left(h^5\right)$, while the total accumulated error is of the order of $O\left(h^4\right)$.

Here y_{n+1} is the RK4 approximation of $y\left(t_{n+1}\right)$, and every next value is determined by the present value plus the weighted average of four increments, each one being the product of the interval size h and an estimated slope (Fig. 4.2) specified by the function f on the right-hand side of (4.7).

- k_1 is the slope at the beginning of the interval, depending on y_0
- k_2 is the slope at the midpoint of the interval, depending on y_0 and k_1
- k_3 is again the slope at the midpoint of the interval, but now depending on y_0 and k_2
- k_4 is the slope at the end of the interval, depending on y_0 and k_3.

Midpoint slopes are assigned to the higher weights when averaging.

Obviously, for the RK4 method the Butcher tableau takes the form:

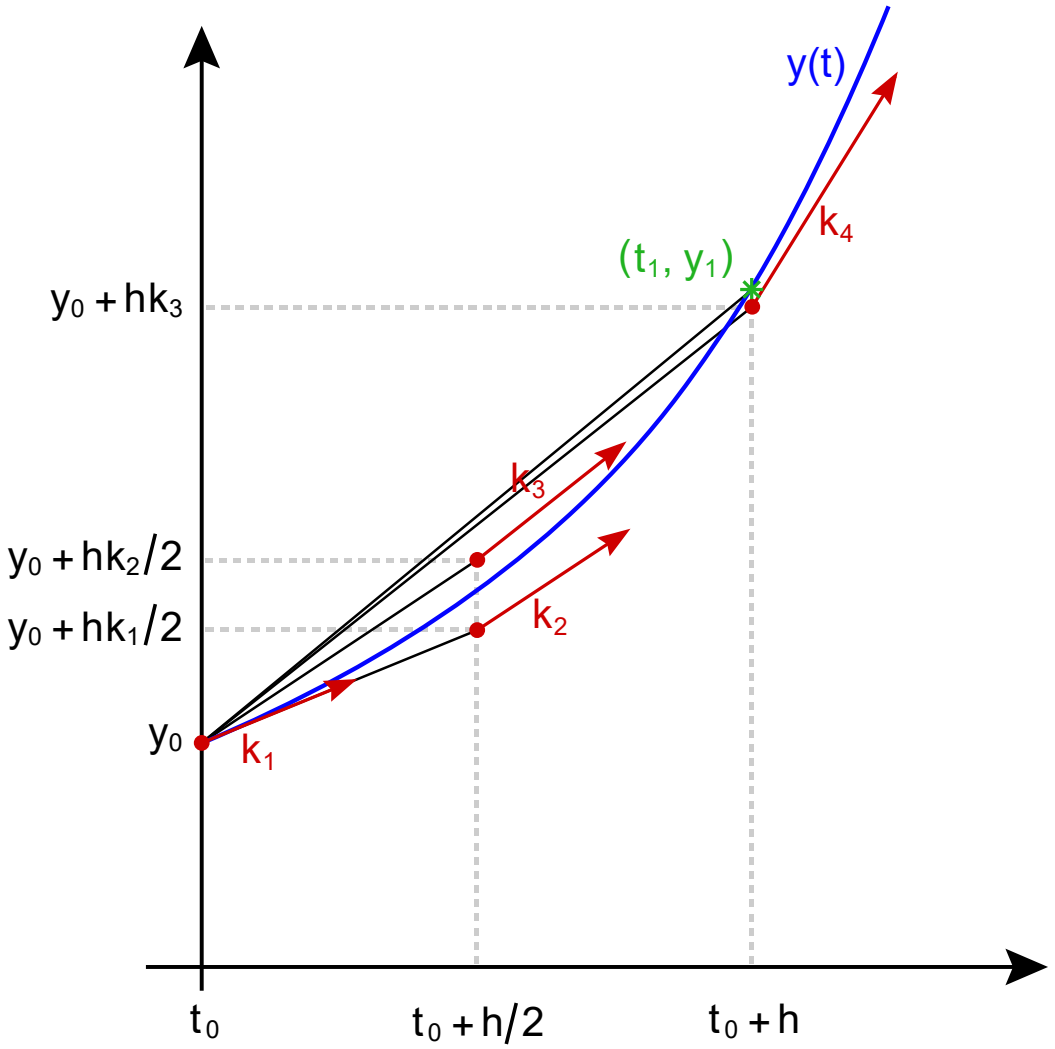

Figure 4.2: Geometrical interpretation of the classical Runge-Kutta method.

0				
1/2	1/2			
1/2	0	1/2		
1	0	0	1	
	1/6	1/3	1/3	1/6

In order to control the errors of the method and ensure the stability of the algorithm, adaptive step size is sometimes used for the numerical solution of the ODE. The idea behind is that a local truncation error is estimated after every step of the RKM. This is

performed with the use of two methods of the order p and $p-1$. Due to the fact that the methods have common intermediate steps, the computational cost of the error estimation is small compared with a step of the higher-order method.

The step is adapted in a sense that the error is compared with the user defined value, and in case the error exceeds this threshold, the step should be repeated with a reduced size, while if the error is much lower than the threshold, the step is increased which enables to save the computational time. In this way the user gets an almost optimal step size automatically.

The step of the lower order is:

$$y^*_{n+1} = y_n + h \sum_{i=1}^{s} k_i b^*_i, \tag{4.8}$$

where k_i are the same as for the method of the higher order. The error is estimated as

$$\varepsilon_{n+1} = y_{n+1} - y^*_{n+1} = h \sum_{i=1}^{s} k_i \left(b_i - b^*_i\right) \tag{4.9}$$

Therefore the Butcher tableau is extended one line more, containing b^*_i:

$$\begin{array}{c|ccccc} 0 & & & & & \\ c_2 & a_{21} & & & & \\ c_3 & a_{31} & a_{32} & & & \\ \vdots & \vdots & \ddots & & & \\ c_s & a_{s1} & a_{s2} & \dots & a_{s,s-1} & \\ \hline & b_1 & b_2 & \dots & b_{s,s-1} & b_s \\ & b^*_1 & b^*_2 & \dots & b^*_{s,s-1} & b^*_s \end{array}$$

There are several adaptive RKM [150]. The authors proposed their own method there, known as Cash-Karp method. Its advantages are discussed in detail in the reference. It should be noted, though, that this method uses six function evaluations to calculate the accurate solutions of the fourth and the fifth order. The Butcher tableau of this method is given in a form:

0						
1/5	1/5					
3/10	3/40	9/40				
3/5	3/10	−9/10	6/5			
1	−11/54	5/2	−70/27	35/27		
7/8	1631/55296	175/512	575/13824	44275/110592	253/4096	
	37/78	0	250/621	125/594	0	512/1771
	2825/27648	0	18575/48384	13525/55296	277/14336	1/4

,

where the first row of b coefficients corresponds to the fifth-order accurate solution, and the second row gives the fourth order solution.

This method is one of the available options to propagate the particles with the CRPropa code, and we used it in our research as well.

4.3 Processing the CRPropa output

4.3.1 Step-by-step processing of the output file

In this paragraph we discuss the processing of the output file, created as a result of an example, single run of the CRPropa code, simulating the propagation of an electron in the Galactic magnetic field. Such a processing is needed to adapt the CRPropa output to the needs determined by the definition of the CRE-related study.

The main goal of a step-by-step output processing is to have full control over its results in a sense of the correct interpretation of the processes occurring during the primary particle and its products propagation. In this regard it is crucial to have as complete information as possible about every particle tracked during a simulation. For this purpose the output module should be included to the *ModuleList* directly, so that the cosmic ray information is written out at every simulation step. The electron is expected to emit synchrotron radiation due to its motion in the magnetic field, and the photons produced can have (or, at least, are not excluded to have) energies large enough to produce electron-positron pairs due to their interaction with the cosmic backgrounds.

To illustrate the CRPropa output handling needed for the purposes of this section we will use an example CRPropa run with the following parameter set:

- The primary electron starting energy $E_0 = 1.0$ EeV;

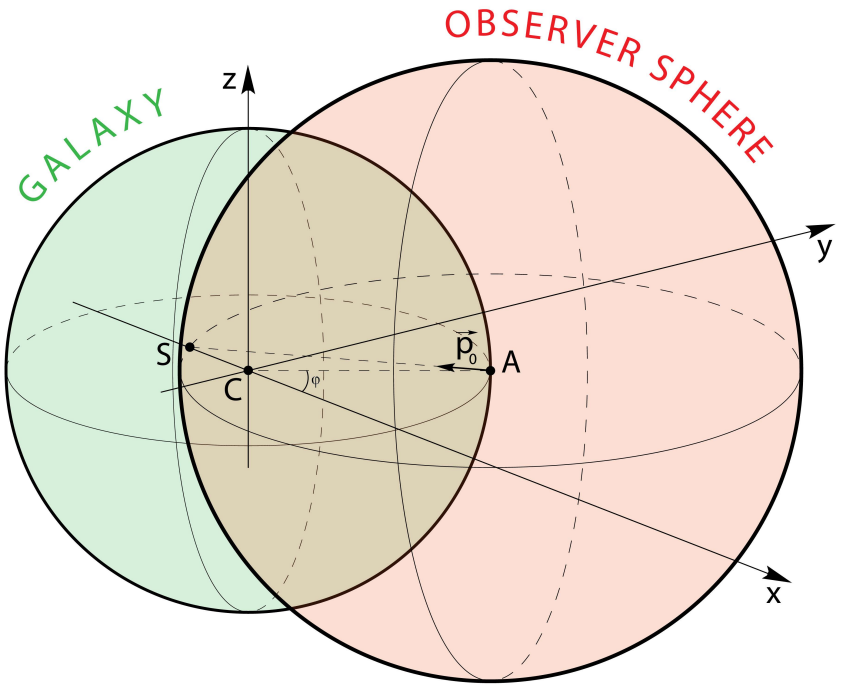

Figure 4.3: Illustration of the simulation setup. C denotes the Galactic Center, S - the position of the Solar System, A is the starting point of the primary electron, $\vec{p}_0$ is its initial direction; $\phi = 30°$.

- The starting point of its propagation is (20.0 kpc, 30.0, 0.0) in the spherical galactocentric system (the Solar system location is (-8.5 kpc, 0.0, 0.0))
- The initial direction of the primary electron is towards the Solar System (its momentum components are calculated in the code and not listed here explicitly)
- The galactic magnetic field according to the JF12 model (see the description in Section 2.4.1)
- The minimum energy threshold $E_{br} = 1.0$ TeV (the particles are stopped after their energy falls below this value)
- The synchrotron radiation threshold is 1.0 TeV (the photons with lower energies are not produced)

The observer surface in the current example was defined as the sphere centered around the primary electron starting point (Fig. 4.3), with the radius equal to the distance from

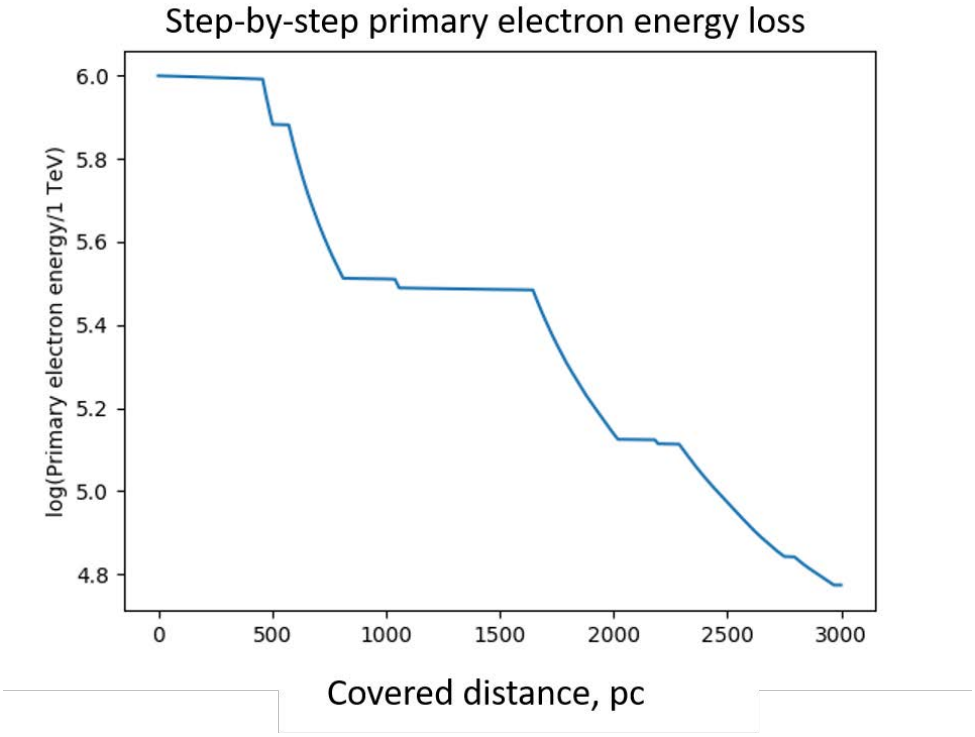

Figure 4.4: Energy loss of the primary electron along its trajectory (first 30 000 steps).

the center to the Solar System (the particles propagation is stopped after they cross the observer surface).

The analysis of the results of CRE simulations with CRPropa in many cases might be not trivial due to the large size of the output files (see the description of the problem and the discussion of the possible ways of handling it in A.1).

One of the key factors in the CRE study is the step by step control of the energy losses of the simulated particles during their propagation. This is well possible with CRPropa, although not without additional processing of the output. An example plot visualising the primary electron energy loss over the travelled distance for the first 30 000 propagation steps is shown in Fig. 4.4 (the overall number of steps is too large to get a representative plot). From the plot one can see that the regions with relatively fast energy loss are followed by those for which the energy loss is a lot slower. Irregular energy losses seen in the plot can be understood keeping in mind the irregularities in the galactic magnetic field model used here (the JF12 model, see 2.4.1) and the physics of synchrotron radiation process, namely, with the fact that the radiated power is proportional to B^2, see 3.13.

In other words, one expects that electrons propagating through the regions where magnetic fields are weaker should lose energy slower than in the case of the stronger fields. Another example (Fig. 4.5) demonstrates the juxtaposition of the electron energy loss along the trajectory with the strength of the magnetic field transverse component. As one can see from the plot, indeed, the fast energy loss regions correspond to the stronger

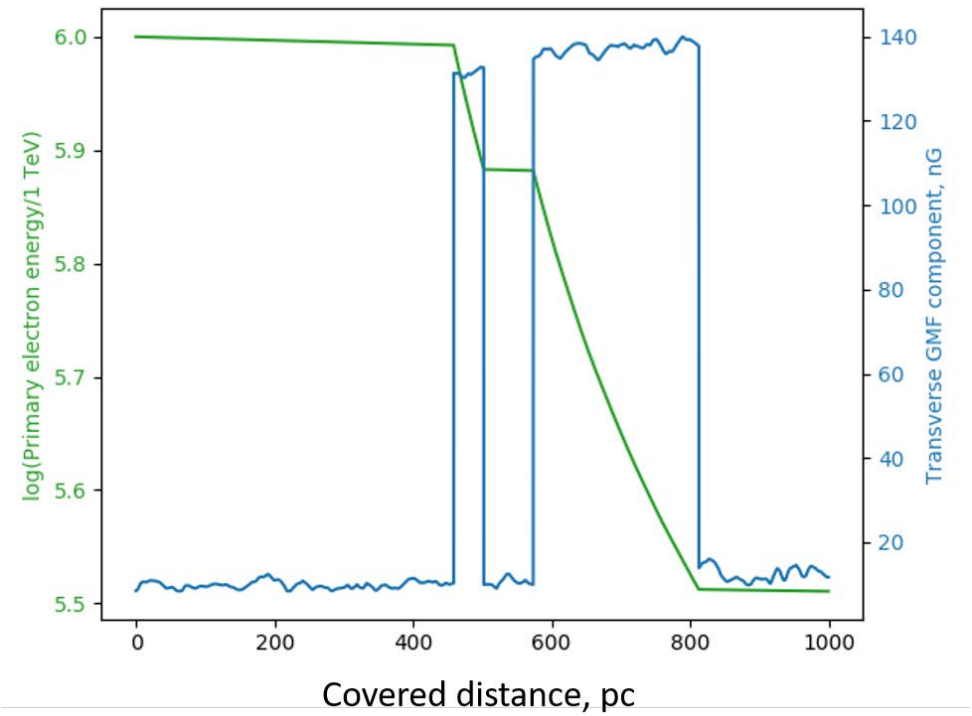

Figure 4.5: Energy loss of the primary electron in the magnetic field along the first 10 000 propagation steps.

deflection of the electron via the Lorentz force in the magnetic field.

The *SynchrotronRadiation* module of CRPropa simulates the continuous energy loss of a charged particle with an option of creating the synchrotron photons above a user-defined threshold as secondary particles. The points of the photon emission are shown in another example extracted from the same run (Fig. 4.6) with the red dots.

Both points in the plotted part of the primary electron trajectory are emitted in the regions with the stronger magnetic field. Such a small number of emitted photons is due to the relatively high threshold for synchrotron radiation energy (1 TeV). The choice of lower value of synchrotron threshold would increase the number of secondary particles, as will be seen in the other examples shown throughout this work. Too many particles in a simulation run cause memory problems, so in practice running a CRPropa simulation dedicated to CRE studies, in particular simulating secondary electromagnetic cascades, imposes restrictions on the input parameter set, even if superior computer resources such as those available in typical supercomputing centers, are available. Understanding and quantifying these limitations is then an important part of this work, and it requires in a sense an "experimental" approach, using a time consuming trial and error method.

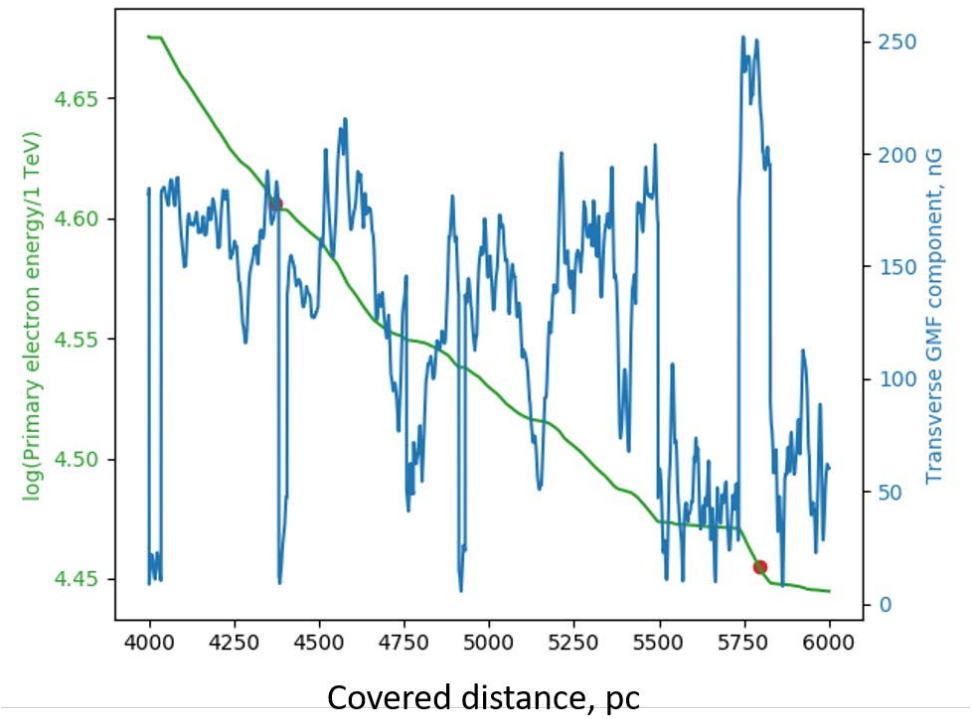

Figure 4.6: Emission points of the above-TeV synchrotron photons during the propagation of the primary electron in the magnetic field.

4.3.2 Propagation of the electron within a plane

On a larger scale the step algorithm used within CRPropa gives reasonably smooth trajectories which is demonstrated in this subsection. In order to zoom at the essential features of the primary electron propagation in the magnetic field we studied the simplest case when the electron propagates in a purely transverse uniform magnetic field. For further simplicity among the available interaction modules only the *"SynchrotronRadiation"* was activated which means that for the sake of demonstration clarity, but also motivated by an important role of synchrotron radiation in electron propagation in the magnetic fields (at least for a certain energy range; see Sec. 3.2), we ignore other processes causing energy losses of the primary electron. We set the initial direction of the primary electron parallel to the X-axis, and let the magnetic field vector be oriented along the Z-axis, to entirely confine the electron trajectory within the XY plane. The complete configuration of the simulation in this example is the following:

- The primary electron starting energy $E_0 = 1.0$ EeV
- The starting point of the primary electron (0.0, 0.0, 0.0)
- The initial direction of the primary electron (1.0, 0.0, 0.0)
- Uniform magnetic field (0.0, 0.0, 200.0) nG

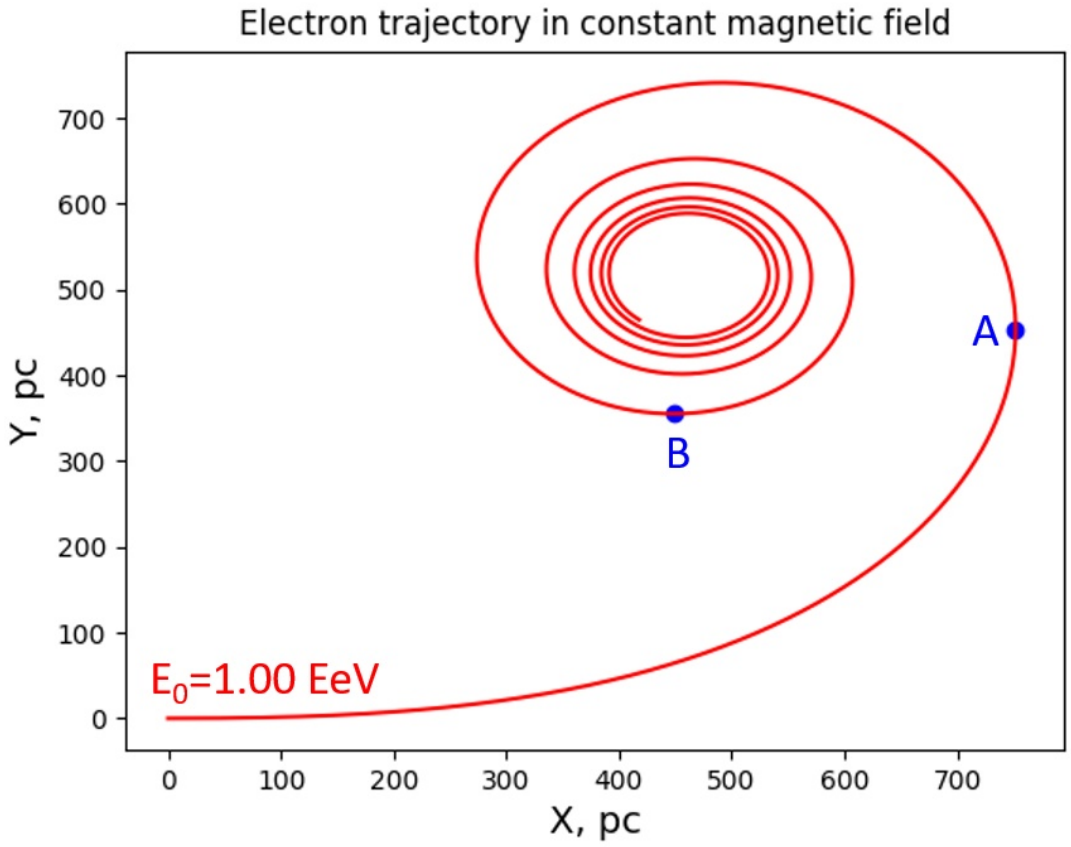

Figure 4.7: The first 50 000 steps of a 1 EeV electron trajectory in the transverse uniform magnetic field of 200 nG obtained with the CRPropa simulation. Point A denotes the first quarter of the first full rotation, while point B marks its end (see the main text for details).

- The minimum energy threshold $E_{br} = 500.0$ GeV
- The synchrotron radiation threshold 1.0 GeV
- Runge-Kutta parameters: sim.add(PropagationCK(B, 10^{-4}, 10^{-4} parsec, 0.1 parsec))

A part of the electron trajectory is shown in Fig. 4.7. It contains only the first 50 000 steps, however, it is clear that the electron will keep on propagating until it reaches the minimum energy E_{br}, rotating counterclockwise with an ever decreasing gyroradius due to the energy loss, also decreasing per step (compare to Fig. 3.2). The parameter choice requires additional comments, because the main goal of this example is full understanding of the influence of every parameter of the input set on the simulation process as well as on its results. This information, as it is shown below, helps defining the optimal threshold conditions to use the computing resources more efficiently.

We note that the minimum energy threshold E_{br}, here 500 GeV, defines the number

of full rotations of the electron before the latter is stopped (we use the "full rotation" term to describe a situation where the trajectory of the electron becomes parallel to its initial direction: e.g. point B in Fig. 4.7 marks the first full rotation of the simulated electron, while point A corresponds to the end of the first "quarter" of a full rotation, after the electron has turned 90 degrees with respect to its initial direction). However, in the context of computations increasing the trajectory length means adding propagation steps and thus overusing resources. Correspondingly, the parameters should be chosen in a way allowing reduce the number of unnecessary iterations. For instance, the electron energy after the first full rotation (point B) is 30.8 PeV (96.92% of the starting energy is already radiated by the electron). If there is no need to study the next full rotations of the electron, 30 PeV could be a reasonable value for minimum energy threshold in the list of the input parameters, which has to be deduced after the test run.

Since the threshold for synchrotron radiation secondaries is lower than the minimum energy of the particles propagation, secondary synchrotron photons are generated by the code, but not propagated for more than one step, as they (mostly) already have energies beyond the breaking condition and are immediately stopped for this reason.

Due to the limited computing resources the simulation of the synchrotron radiation has to be activated (by setting the corresponding flag while configuring the *Synchrotron-Radiation* module) with a user-defined threshold for the minimum energy of a synchrotron photon E^{min}_{synch}: synchrotron photons of energies $E_{synch} < E^{min}_{synch}$ are not simulated. This restriction on E_{synch} is implemented in the CRPropa code by applying the condition:

$$E_{synch} < E^{min}_{synch} = 14 \cdot E_{crit}, \tag{4.10}$$

with E_{synch} denoting the synchrotron photon energy and E_{crit} standing for the critical photon energy expressed by Eq. 3.30. Namely, it is a parameter of the synchrotron radiation spectrum pointing to the frequency region where the emission is negligible; synchrotron photons of significantly higher energies are emitted very rarely and hence can be ignored in the simulations. To define the limit for this negligibility in the CRPropa the factor "14" is used in the condition above which seems a reasonable choice well grounded in classical textbooks and plots showing synchrotron radiation.

It is important to mention that setting E^{min}_{synch} automatically limits the electron energy E^{e}_{thr} below which the production rate of synchrotron photons of energies above E^{min}_{synch} is negligible, and thus not simulated by CRPropa. In our example we require that $E^{min}_{synch} =$ 1.00 GeV (see the parameter list above) which corresponds to $E_{crit} \approx 0.07$ GeV and $E^{e}_{thr} \approx 74.75$ PeV (the values of the correspondent parameters are: $R = 1.25 \cdot 10^{19}$ m, $\gamma = 1,46 \cdot 10^{11}$) - below this energy we do not simulate any synchrotron emission that fulfills the E^{min}_{synch} condition (4.10), as illustrated in Fig. 4.8. Here the electron energy at the point where it reaches $E_e = 74.75$ PeV is marked by a blue point; its normalized

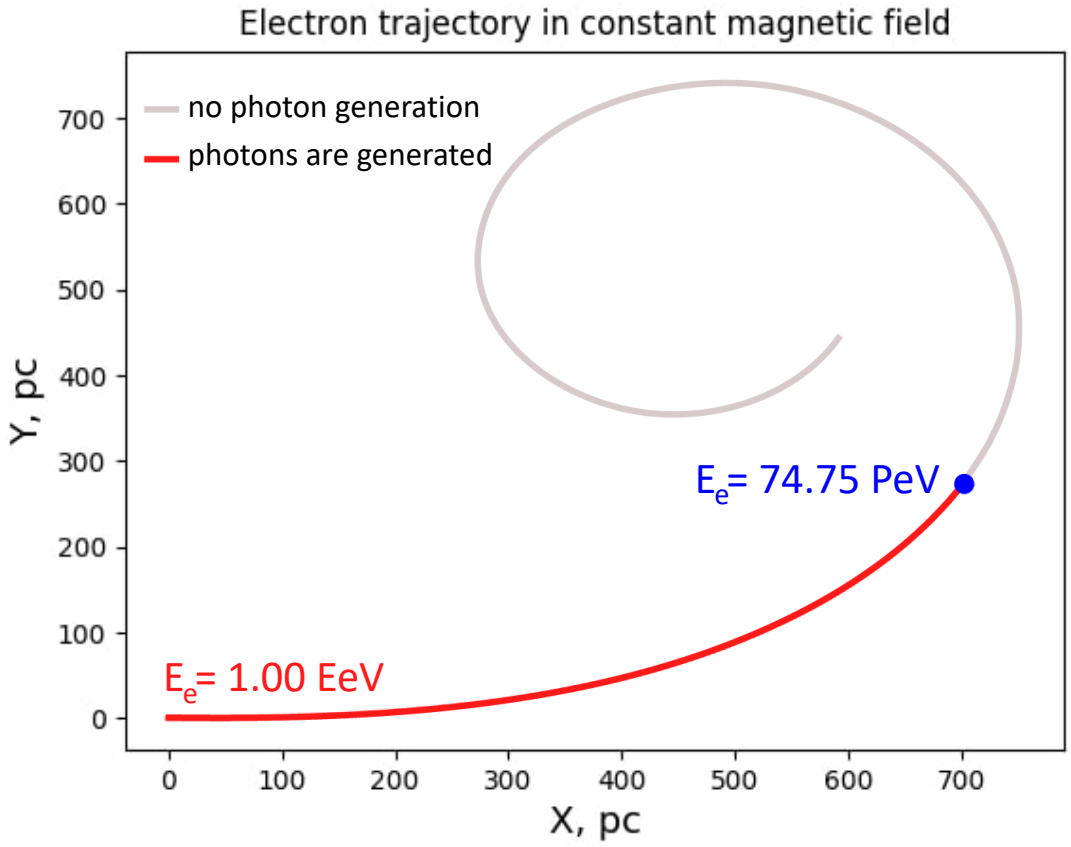

Figure 4.8: A part of the primary electron trajectory with the "photons production threshold" affecting the simulation, here denoted with the blue dot (see the details in the main text).

momentum here is (0.49429, 0.86930, 0.0). This limits the arc of an angular size of around 60°, along which secondary photons are generated by CRPropa. For comparison, the primary electron energy E_e after the first full rotation (point B in Fig. 4.7) is 30.68 PeV, while the other relevant parameters are $R = 165.9$ pc, $\gamma = 6 \cdot 10^{10}$, $E_{crit} = 0.0125$ GeV and no photons of energies above 1 GeV are simulated any more. We can finally infer that in the current example there is no need to chose the minimum energy threshold E_{br} below 70 PeV, since the "lower-energy" part of the electron trajectory is not important for the study of synchrotron radiation.

4.3.3 Distribution of photons along the propagation step

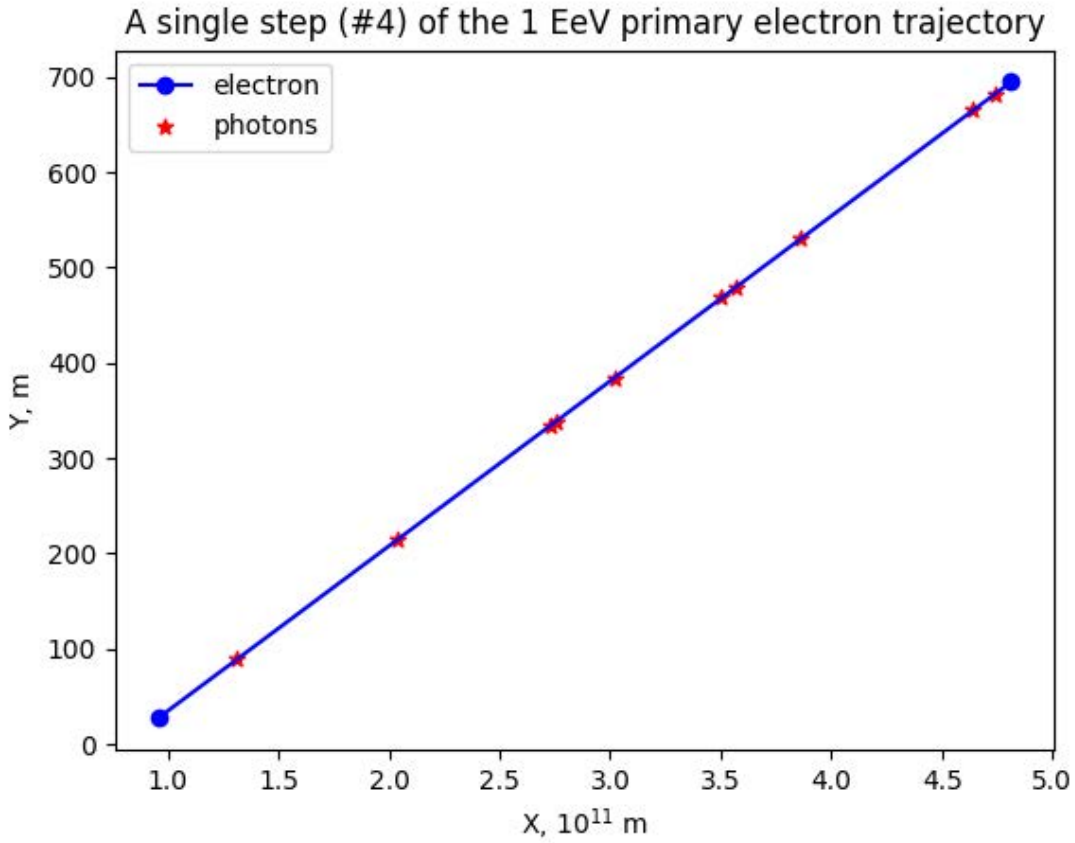

Figure 4.9: Emission of synchrotron photons along a single step of the primary electron trajectory. The electron propagates from the left bottom to the top right.

Since we are interested in obtaining a detailed information on a cascade of particles within an observational reach of the standard astroparticle physics infrastructure, we are motivated to reduce the synchrotron threshold value down to even 1 GeV, which is still acceptable in terms of available computing resources and which seems to be the lower limit of terrestrial gamma rays observatories (for example, [151], [152]). In future, and with more efficient computing resources or simulation programs, one would be interested in tracking the photons of even lower energies, so that even the available satellite data on low energy photons can be used in the search for CRE. Here, to study the photons emission from a single propagation step, we used the same energy parameters, field value, the starting point and initial direction of the electron as in the simulation setup in a previous subsection (4.3.2), reducing only the propagation step size. In the current example the parameters of the Runge-Kutta method are specified as:

sim.add(PropagationCK(B, 10^{-4}*,* 10^{-7} *parsec,* 10^{-4} *parsec)).*

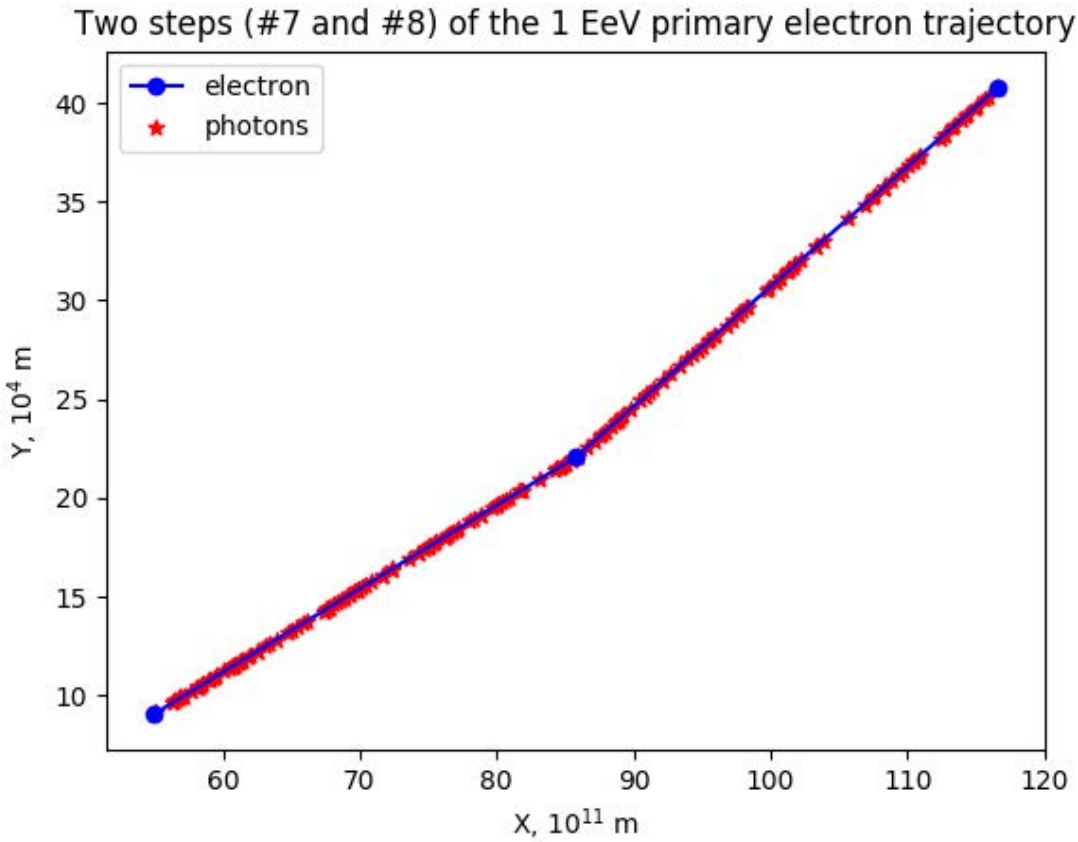

Figure 4.10: Emission of synchrotron photons along two consecutive steps of the primary electron trajectory. The electron propagates from the left bottom to the top right.

We plotted the fragments of the electron trajectory in the magnetic field: a single step, the 4^{th} one, (Fig. 4.9), and two consecutive steps, 7^{th} and 8^{th}, (Fig. 4.10), denoting the photons emission points along the steps with the red stars. The plots demonstrate the difference of the step lengths due to the use of the adaptive step size mechanism. Step 4 (Fig. 4.9) is 8 times shorter than each of the two steps shown in Fig. 4.10 (steps 7 and 8). Since the energy loss of the charged particle is proportional to the distance it covered, the number of photons emitted during different parts of the primary electron trajectory varies correspondingly (in the plotted cases 10 photons for a single step in Fig. 4.9 and 182 photons in total for two steps in Fig. 4.10). The steps in the CK method are consecutively increased by a factor 5 starting from the minimal value until the maximal value is reached, and from that moment on the step size remains unchanged (equal to the maximal value) until the particle is stopped. In our example the maximal step size is 1000 times larger than the minimal one, thus, in units of minimal step sizes the ratios of the consecutive step lengths are 1:5:25:125:625:1000:1000:1000:..., so the fraction of 7th or 8th step lengths to the 4th step length in the same units is 1000:125=8.

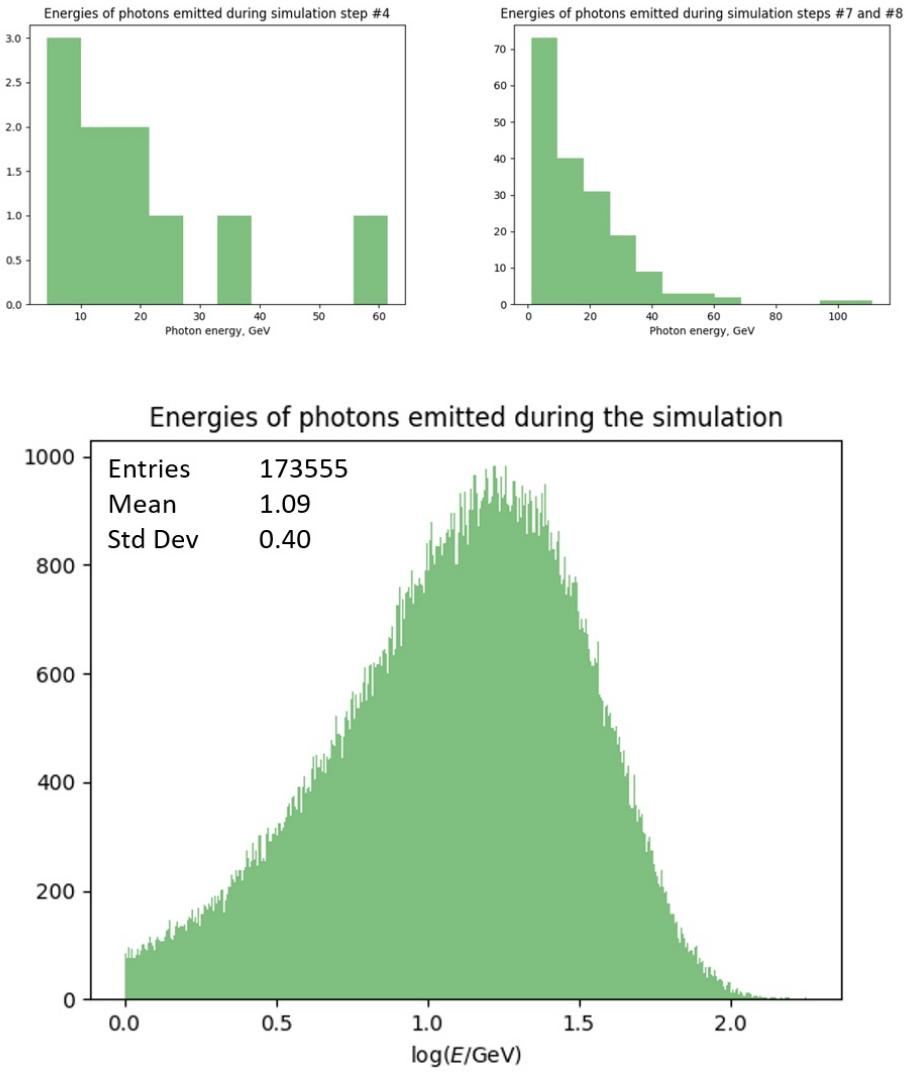

Figure 4.11: Distributions of the emitted photons energies. Top left: step 4; top right: two consecutive steps 7 and 8; bottom: all steps.

The energy spectra of the emitted photons for the trajectory parts plotted above as well as for the whole run are shown in Fig. 4.11. It could be inferred that the distribution of photons is centered at around tens of GeV, which is compatible with the sensitivity regions of the current instruments. On the other hand, the spectrum can help selecting input parameters, in particular, the synchrotron radiation threshold, for the simulations in given conditions. For instance, from the bottom panel of Fig.4.11 one can safely infer that in the demonstrated example the reasonable E^{min}_{synch} can be set to 100 GeV.

Chapter 5

Processing the CRPropa output with CRE-pro

5.1 Motivation for external processing of the CRPropa product particles

The estimation of CRE shapes and sizes as well as of their probability to be registered with terrestrial or human technosphere-based arrays of detectors requires precise knowledge of the synchrotron photons distribution along the electron trajectory as well as over the observer surface. As it is shown below, we developed an algorithm, later referred as the "CRE-Pro" script, which allows to skip tracking of photons with CRPropa (see App. B for technical details). This part of simulation is quite trivial from the physics point of view (linear propagation in overwhelming majority of cases), but uses a significant amount of computing resources due to the huge number of particles needed to be kept in memory. Also, the external script can be used for processing the similar output obtained with the use of different simulation codes.

We are particularly interested in studying the propagation of charged particles in the electromagnetic fields leading to synchrotron emission of photons, which are the main component of an electromagnetic particle cascade, such as a CRE. The most obvious way of calculating the particle trajectory is applying iterative methods to solve the differential equations of motion in an environment, usually containing some field, which affects the particle propagation. The resulting trajectory of a particle is a polygonal chain consisting of a series of line segments (propagation steps).

5.2 Geometrical interpretation

As it was already shown (Fig. 4.9, 4.10), numerous synchrotron photons can be emitted along a single propagation step of the electron in the magnetic field. The main geometrical

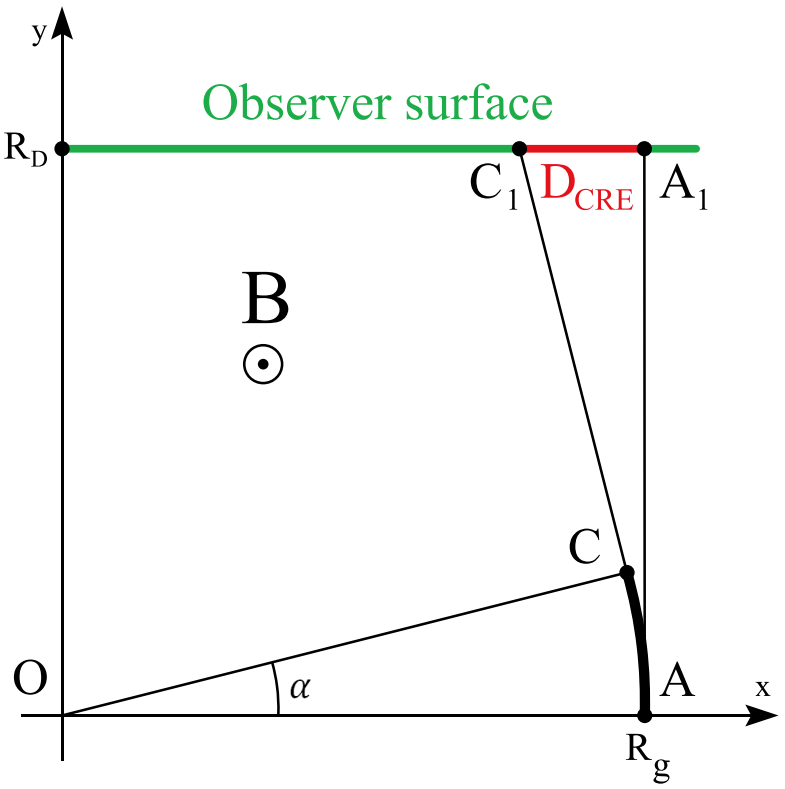

Figure 5.1: Geometrical interpretation of the CRE-Pro script.

idea behind the "CRE-pro" script is that all these photons due to their linear propagation will be confined within some area A_1C_1 of an observer surface (Fig. 5.1), and the size of this area D_{cre} is, in fact, the size of the CRE formed by these photons. The area is in a sense the projection of the step onto the observer surface.

Consider an electron with the energy value E propagating in a transverse magnetic field of the strength B. The real trajectory of the electron is bended by the Lorentz force, forming a complicated spiral with an increasing curvature, like the one demonstrated in Fig. 4.7, described by its gyroradius

$$R_g = \frac{\gamma m v_\perp}{c|q|B} = \frac{E}{ceB}, \tag{5.1}$$

thus a linear propagation step with the length D_{step} is an approximation of an arc AC of the angular size α, where

$$\alpha = \frac{D_{step}}{R_g} \tag{5.2}$$

The photons generated along a given step (arc) should propagate along the lines tangent to the arc at the points of emission, thus, such lines at the beginning and at the end of the step define the edges of the step projection onto the observer surface. The universality of the approach suggests that the observer surface can be defined according to the geometry of a certain physics situation. However, we have chosen the simplest case of the observer surface - a plane, keeping in mind it is situated far enough from the moving particle in the majority of cases of CRE simulations. We are mostly interested in the cases when the size of the observer surface is small with respect to its distance from the emitting region (the electron propagation step), thus a plane is an acceptable approximation and no important details are neglected with the use of this simplification. We placed the observer plane at a distance R_D from the start of the step perpendicularly to the tangent line at this point.

D_{CRE} as a function of α, B, R_D and E can be easily derived using the following geometrical considerations. Suppose the electron trajectory is completely contained within the XY plane (Fig. 5.1). The Cartesian coordinates of the starting point A of the step are (R_g, 0.0), and the electron momentum has initial components (0.0, 1.0). The coordinates of the step ending point C are ($R_g \cos\alpha$, $R_g \sin\alpha$). The intersection points of the observer plane with the tangent lines to the step edges are, correspondingly, A_1 (R_g, R_D) and C_1 ($\frac{R_g}{\cos\alpha} - R_D \tan\alpha$, R_D). Finally,

$$D_{CRE} = A_1C_1 = R_g - \frac{R_g}{\cos\alpha} + R_D \tan\alpha. \tag{5.3}$$

5.3 The CRE-pro algorithm and usage examples

Using expression 5.3, we generated "parameter phase space", looping over the input characteristics of the environment (α, B, R_D and E), in which simulation of the electron propagation is supposed to take place, to obtain the (D_{step}, D_{CRE}) "coordinates" of the points in a 2D phase space cross-section (e.g. Fig. 5.2). The phase space should universally point to parameter regions where observable CRE can be expected. Still, Monte Carlo simulations are needed to tell which parameter regions are expected to occur in reality.

Each of the input parameters ran through the several orders of magnitude of its value in order to cover a wide range of combinations which should correspond to various physics environments (Tab. 5.1). The overall number of combinations is 64000, among which 1805 were excluded because of geometrical restrictions (we had to take care the step does not cross the observer plane).

In order to visualize the obtained phase space we plotted its 2D cross-sections. Two of four input parameters are kept constant (their values are displayed at the plots headers), the third parameter runs through the example set and is displayed on a plot as a family of the colored lines, and the fourth runs through the whole range of its change, resulting

Table 5.1: Parameters used for the "phase space" simulation. Every parameter changes with a unit logarithmic step

Parameter	Min. value	Max. value	Units	Number of bins
α	10^{-12}	10^{-3}		10
B	10^{-9}	10^{15}	G	25
E	10^{6}	10^{21}	eV	16
R_D	10^{-6}	10^{9}	pc	16

Table 5.2: Parameter values selected for the "example set"

Parameter	Minimal value	Maximal value	Units	Steps, orders of magnitude	Number of bins
α	10^{-12}	10^{-3}		3	4
B	10^{-9}	10^{-3}	G	2	4
E	10^{9}	10^{18}	eV	3	4
R_D	10^{-6}	10^{6}	pc	3	5

in the dots on a plot. The example set (Tab. 5.2) contains only some values, which change with the step of several orders of magnitude, of each parameter from Tab. 5.1 in illustrative purposes, to avoid making the resulting plots (Fig. 11 a-l) too messy. The plot types are denoted by f1... f12 specified in the each plot caption.

Together with the dependencies of (D_{step}, D_{CRE}) pairs on the input parameters each plot contains the lines, corresponding to the Earth size (average diameter 13 742 km), Moon average apogee (405 400 km), and Mars aphelion (249 200 000 km), in order to compare the sizes of CRE, expected to be formed in different physics conditions, with the listed distances.

Dependencies of the step-projection lengths on the angular step size α are presented in Fig. 5.2-5.4. Each of them contains 10 points on the line of each color, explained in the plots legends, corresponding to 10 different values of α used for the phase space simulation. The absence of several points on one or more lines means the intersection of the step with the observer plane (Fig. 5.1), which corresponds to a different geometrical situation and is thus not taken into account. The values of α increase with the step of one order of magnitude from the bottom left to the top right on each of the plots, starting with 10^{-12}. As it can be seen from Fig. 5.2, the steps of the electron trajectory with the energy 1 EeV at the beginning and small enough angular sizes can project onto the observer plane, located 1 pc away from the beginning of the step, occupying the areas smaller that the Earth size, which is potentially favorable for registration with the terrestrial detectors.

For a given electron energy value as well as the strength of the magnetic field there is a limitation of distances to the observer plane, which contains projections not exceeding the Earth size. For example (Fig. 5.3), for a 1 EeV electron propagating in a 10 μG transverse magnetic field one can deduce that the steps with $\alpha = 10^{-12}$ can project to the Earth sized area in case they are distanced on parsecs from the observer. The further

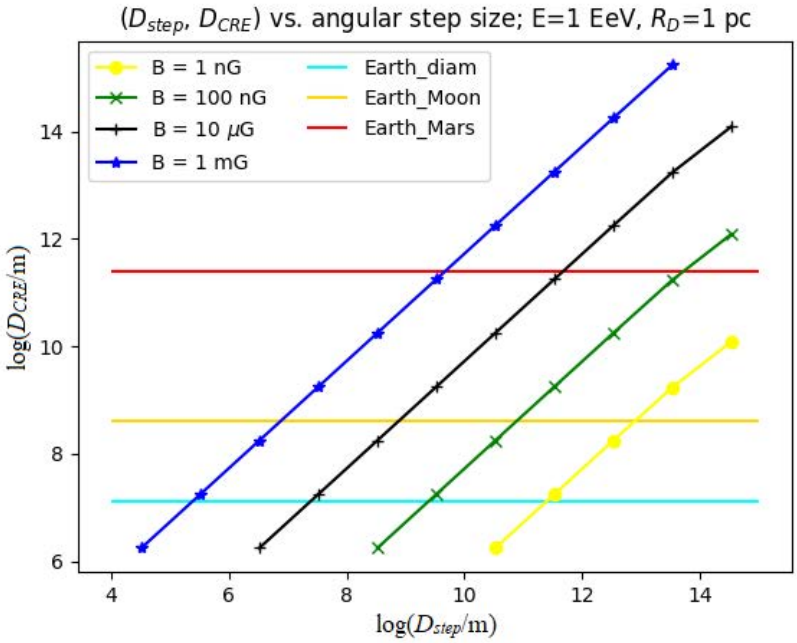

Figure 5.2: (D_{step}, D_{CRE})=$f1(\alpha)$ for different B (the legend), while the values of R_D and E are fixed (the plot header).

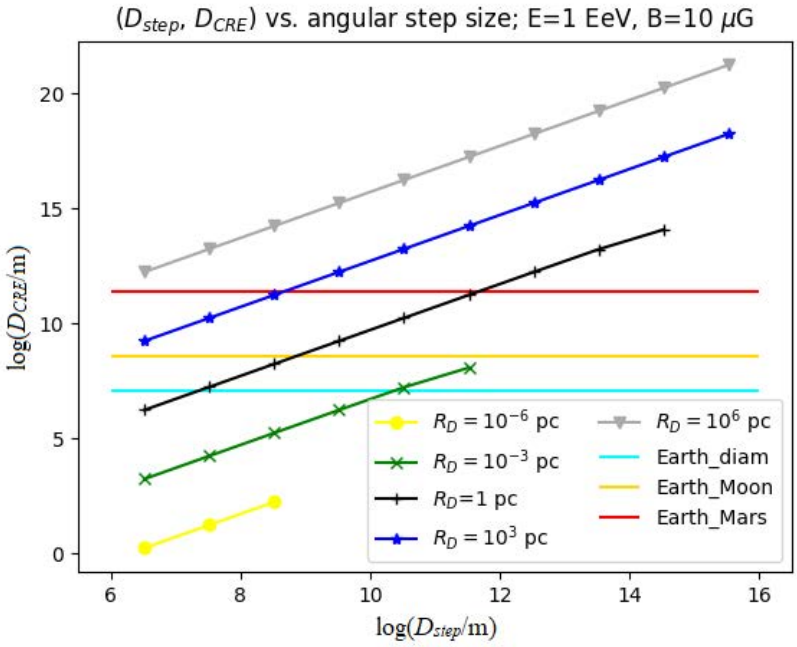

Figure 5.3: (D_{step}, D_{CRE})=$f2(\alpha)$ for different R_D (the legend), while the values of B and E are fixed (the plot header).

reduction of the step can only increase the distance of our interest.

The energy of the primary electron affects the gyroradius of its trajectory and thus the linear step size is proportional to the energy of the electron for the same angular step

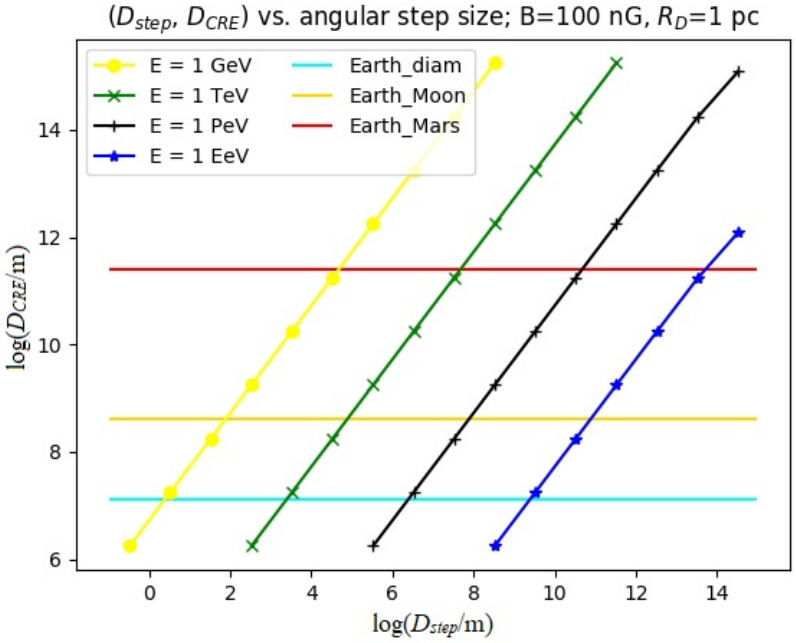

Figure 5.4: (D_{step}, D_{CRE})=$f3(\alpha)$ for different E (the legend), while the values of B and R_D are fixed (the plot header).

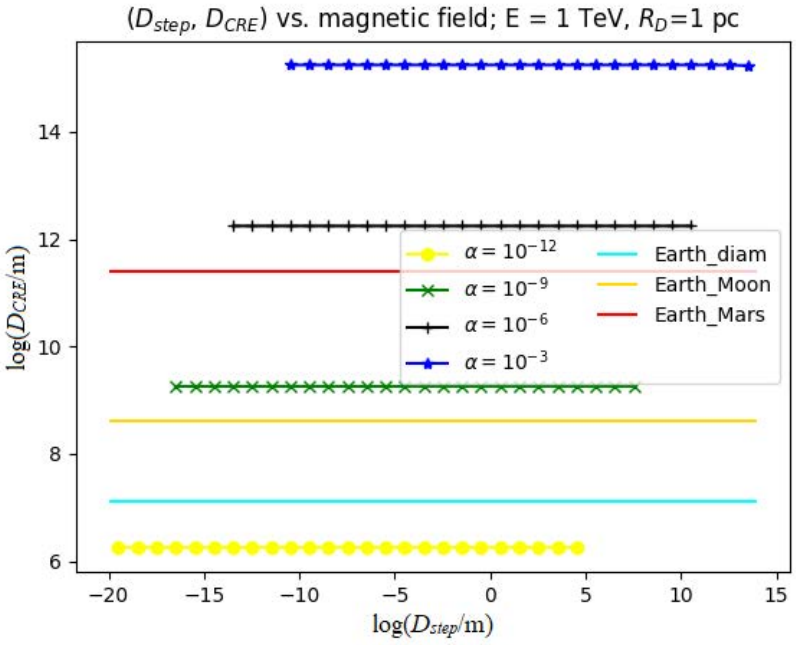

Figure 5.5: (D_{step}, D_{CRE})=$f4(B)$ for different α (the legend), while the values of E and R_D are fixed (the plot header).

size α (Fig. 5.4).

Dependencies of the step-projection lengths on the magnetic field strength B are plotted in Fig. 5.5-5.7. Each of them contains 25 points on the colored lines, explained in

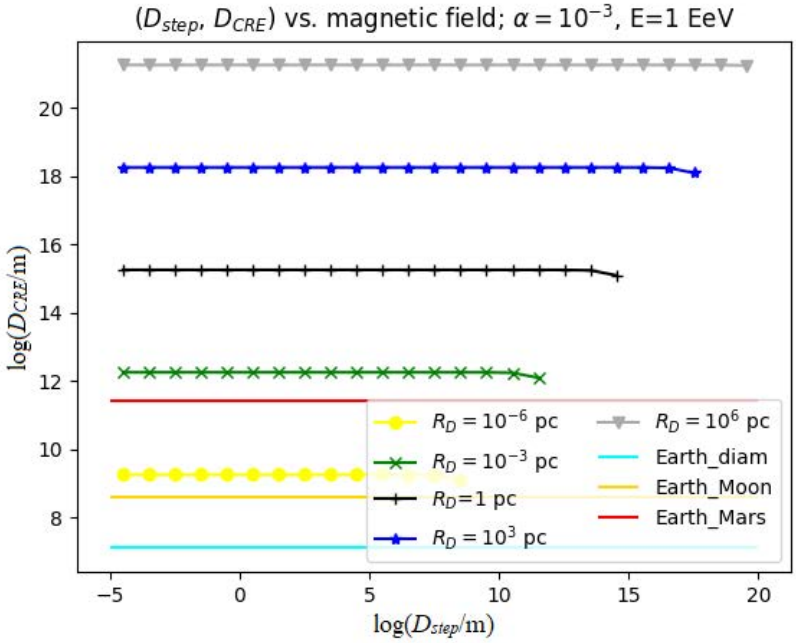

Figure 5.6: (D_{step}, D_{CRE})=$f5(B)$ for different R_D (the legend), while the values of α and E are fixed (the plot header).

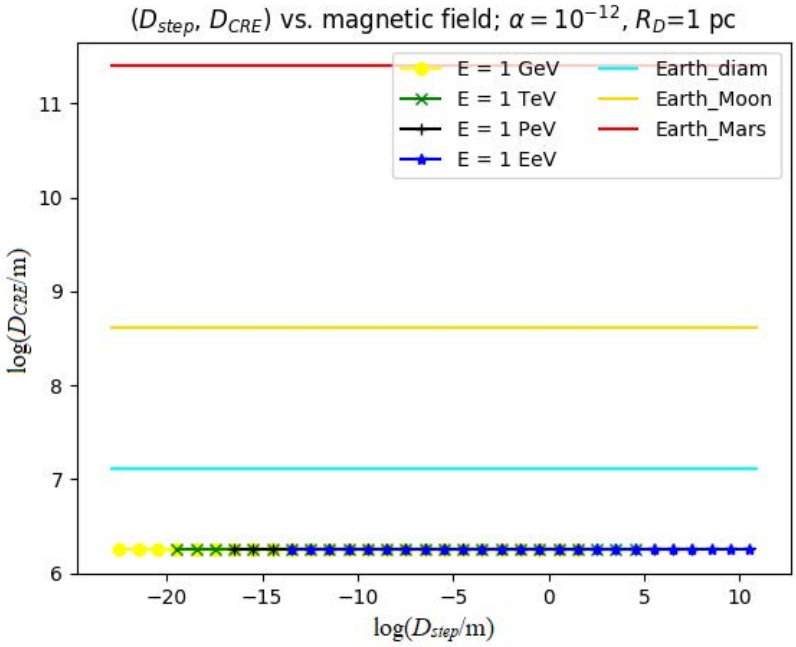

Figure 5.7: (D_{step}, D_{CRE})=$f6(B)$ for different E (the legend), while the values of α and R_D are fixed (the plot header).

the plots legends, corresponding to different values of magnetic field strength used for the phase space simulation. The field increases from right to left along each line of the plot, starting from 10^{-9} G (the gyroradius of the trajectory is inversely proportional to

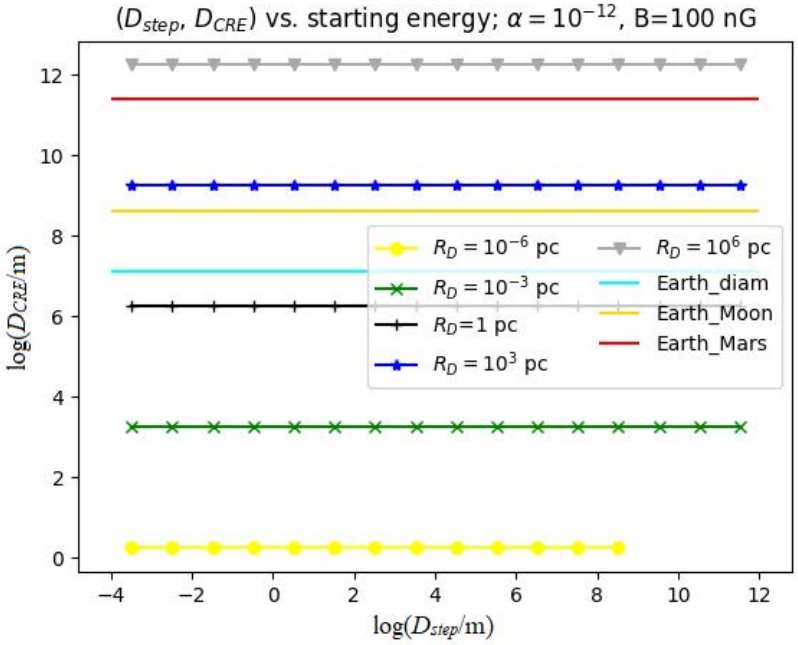

Figure 5.8: (D_{step}, D_{CRE})=$f7(E)$ for different R_D (the legend), while the values of α and B are fixed (the plot header).

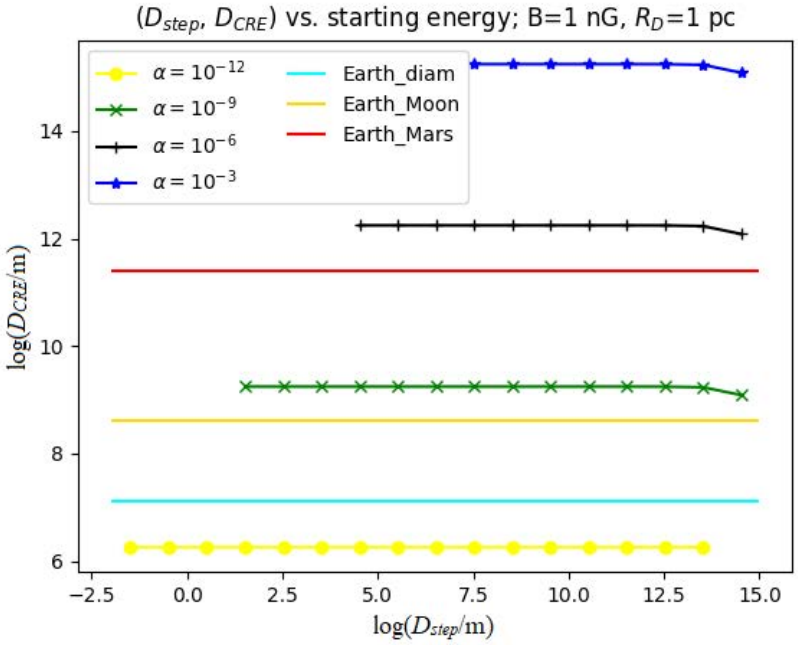

Figure 5.9: (D_{step}, D_{CRE})=$f8(E)$ for different α (the legend), while the values of R_D and B are fixed (the plot header).

the field strength). The step projections not exceeding the Earth size are formed when the angular step size α (Fig. 5.5) and the observer distance (Fig. 5.6) are selected appropriately regarding the energy of the electron at the beginning of the step. Since the step

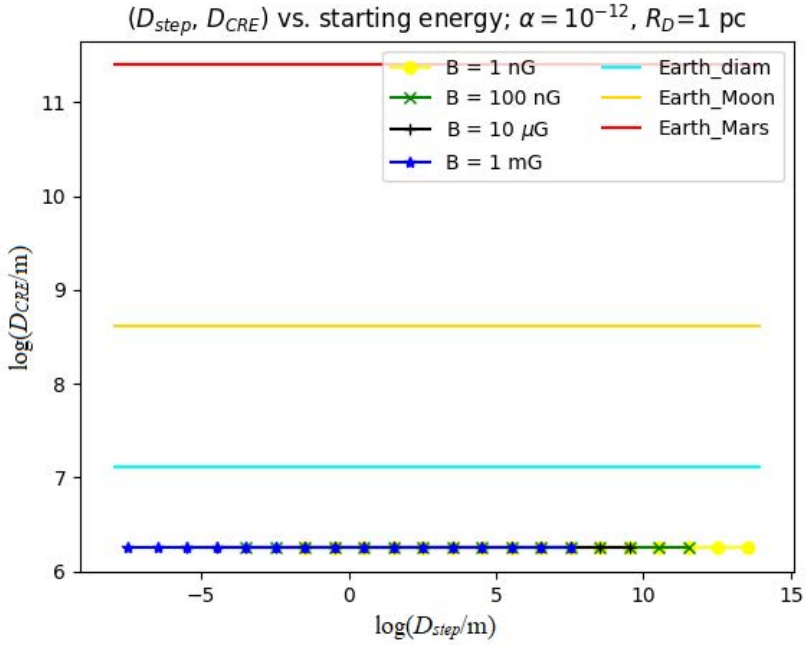

Figure 5.10: (D_{step}, D_{CRE})=$f9(E)$ for different B (the legend), while the values of α and R_D are fixed (the plot header).

sizes are proportional to the gyroradius, which is proportional to the $\frac{E}{B}$ ratio, the plots for different energies partly overlap, as shown in Fig. 5.7, while the size of the step projection depends on the distance to the observer.

Dependencies of the step-projection lengths on the electron energy E at the beginning of the step are plotted in Fig. 5.8-5.10. Each of the plots is supposed to contain 16 points on the colored lines, explained in the plots legends, corresponding to different energies of the electron at the beginning of the step, used for the phase space simulation. The electron energy increases from left to right, starting from 1 GeV (the gyroradius of the electron trajectory is proportional to its energy). As it has already been described, the distances from the beginning of the step to the observer plane where the projection smaller than the Earth size is formed, can reach up to parsecs in case the propagation step is short enough (Fig. 5.8), and the reduction of the step leads to an increase of this distance. The strength of the magnetic field affects the step length via the gyroradius, so the plots for different fields partly overlap for the reasons also mentioned above.

Dependencies of the step-projection lengths on the distance to the observer plane R_D are plotted in Fig. 5.11-5.13. Each of the plots contains 16 points on the colored lines, explained in the plots legends, corresponding to different distances of the observer plane from the beginning of the electron propagation step, used for the phase space simulation. With the increase of the observer distance, starting from 10^{-6} pc (upwards on each of the plots) the CRE size also grows, but still, in case of a small enough angular step size α (Fig. 5.11) the optimistic conditions for the formation of a CRE below the Earth size

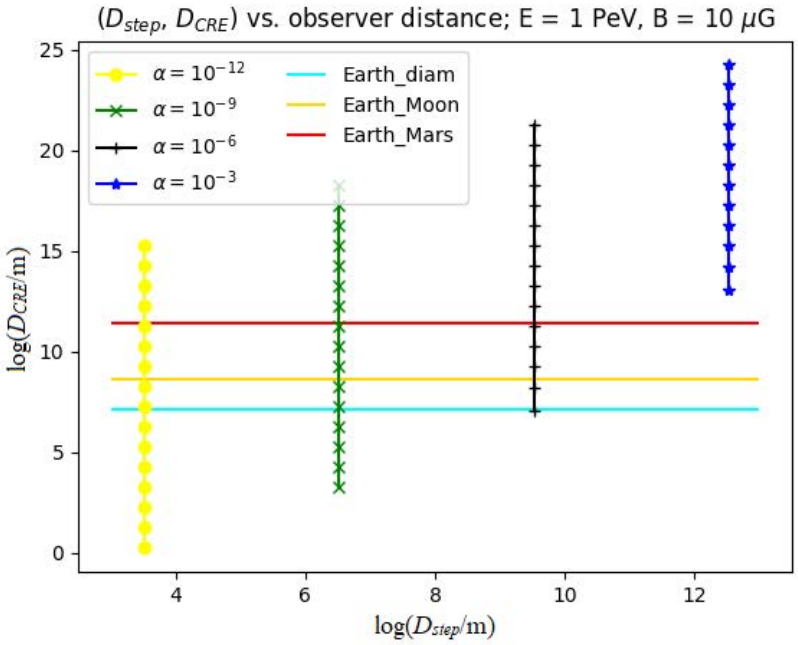

Figure 5.11: (D_{step}, D_{CRE})=$f10(R_D)$ for different α (the legend), while the values of B and E are fixed (the plot header).

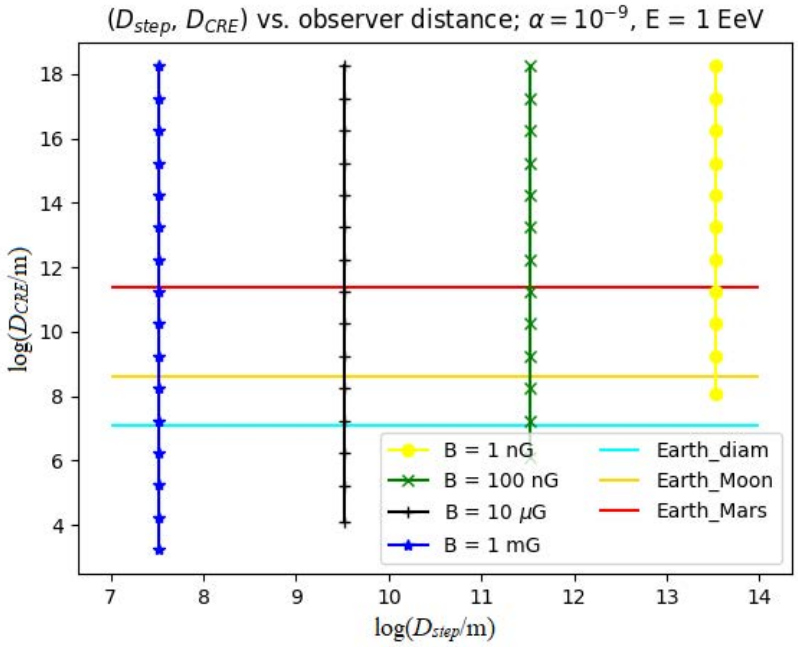

Figure 5.12: (D_{step}, D_{CRE})=$f11(R_D)$ for different B (the legend), while the values of α and E are fixed (the plot header).

are met for the longer observer distances. Stronger magnetic fields are another favorable factor to observe the Earth sized CRE on the larger distances (Fig. 5.12). Larger gyroradii corresponding to the higher value of the electron energy at the beginning of the step

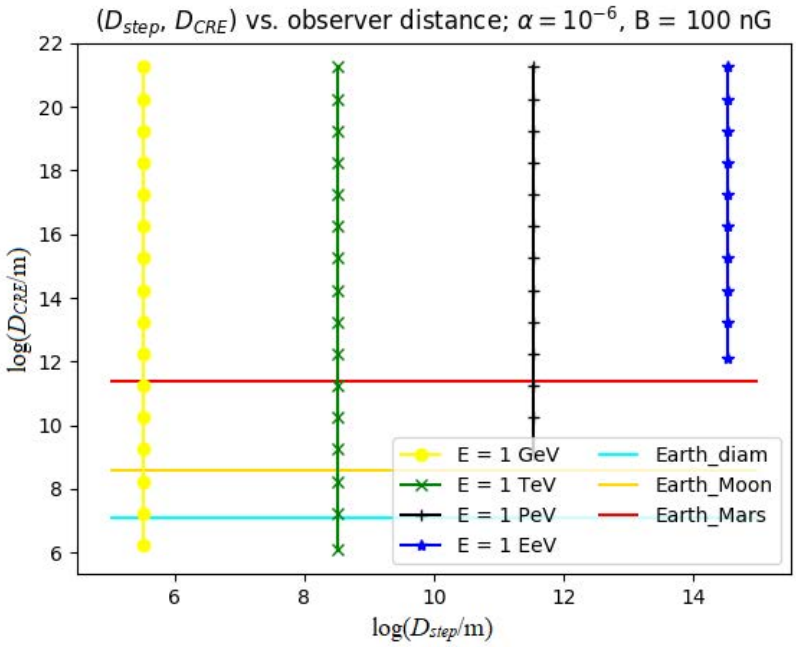

Figure 5.13: (D_{step}, D_{CRE})=$f12(R_D)$ for different E (the legend), while the values of α and B are fixed (the plot header).

result in the increase of the step length, while the projection length remains unchanged (Fig. 5.13).

The cross-sections of the phase space, presented in Fig. 5.2-5.13, show that there are combinations of the input parameters that allow the step of the electron to be "projected" onto the observer plane having sizes favorable for their potential observation on the Earth.

It is important to stress that in all the examples demonstrated in this chapter a single propagation step of the electron and its projection were considered, because the step is the simplest part of the trajectory obtained during a simulation. However, numerous photons are emitted along the step, and all of them should be located within the calculated step projection. As we have already mentioned (3.4.3), the definition of the CRE is equivalent to "$N > 1$", with N standing for the number of photons forming the CRE. Thus, to obtain a more detailed picture of possible sizes and configurations of CRE as they are defined above, the distribution of synchrotron photons emitted along the electron propagation step should be taken into account. The results of such study are illustrated and discussed in the next chapter of the thesis.

Chapter 6

CRE horizon

6.1 The "ideal" CRE horizon phase-space

In order to analyze the propagation of the electron simulated with CRPropa, a few remarks should be made regarding the extraction of parameters necessary to calculate the size of the step projection at the observer surface. Each part of the electron trajectory, i.e. a single propagation step, has a certain spatial extent, thus both magnetic field and electron energy vary along it.

As far as the particle energy is concerned, CRPropa algorithm writes down the energy values only on the step edges, i.e. the energy loss is accounted for only along the whole step, without exact recalculation made for every emitted photon "inside" the step. This allows to skip computations of the trajectory gyroradius after every emission act and saves much time and resources, but the photons simulated in this simplified way are assigned to with the momenta equal to that of their parent electron. Their exact distribution over the observer surface is the subject of the discussion in this chapter.

In case the magnetic field experiences dramatic changes along a single propagation step, it is logical to divide the step into the smaller parts with smoother field changes, to be able to describe the field strength with a certain value. However, this approach requires unnecessary complications; besides, such abrupt field strength oscillations are unlikely to occur too frequently, because the step size chosen for our simulations is usually much smaller than the regions of a substantial magnetic field change (fractions of a parsec for the step size vs. tens of parsecs for the GMF coherence length). One of the possible solutions is to extract the strength of the transverse magnetic field in every point of the synchrotron photons emission along the step, and then compute its mean value B_{av} the as well as the standard deviation B_{std}. After that the steps for which $B_{std} > n \cdot B_{av}$, where n is an arbitrary chosen fraction of a unit, can be filtered out, and the strength of the magnetic field can be considered equal to B_{av} for the rest of the steps.

However, we performed calculations using the largest value of B together with the

energy at the end of the step, because within such an approach the gyroradius of the electron trajectory is minimal, and thus the maximal length of the step projection on the observer plane (Fig. 5.1) is computed.

Below we present the results of an example simulation run analysis. We used the following setup parameters to obtain the trajectory of the electron:

- The primary electron starting energy 3.981 EeV
- The starting point of the primary electron is the Galactic center, the origin point of the galactocentric coordinate system, (0.0, 0.0, 0.0)
- The initial direction of the primary electron (-1.0, 0.0, 0.0) (towards the Solar System)
- The galactic magnetic field described by the JF12 model 2.4.1
- The minimum energy threshold $E_{br} = 10$ TeV
- The synchrotron radiation threshold 1 GeV
- Runge-Kutta method parameters: sim.add(PropagationCK(B, 10^{-4}, 10^{-5} parsec, 10^{-2} parsec))

6.2 "N=2" horizon

As it was already mentioned, the propagation of synchrotron photons within the CRPropa simulation chain is replaced by the CRE-Pro script. This means that the emission points of the synchrotron photons along the step are known from the CRPropa output, but the exact distribution of photons over the step projection on the observer plane should be deduced using some extra assumptions. The simplest one is that the photons are distributed over the projection equidistantly (from this point on this case is referred to as the "uniform distribution"). It is an entirely artificial approach as there are no reasons to expect such a distribution to occur in reality. Nevertheless, assuming N photons being emitted along the propagation step (and we are interested in the $N \geq 2$ case which is logically connected with the definition of a CRE; there are 589 steps meeting this condition in the presented example), we calculated the observer distances for which 2 neighbouring photons on the step projection are located at a distance not exceeding the Earth size, denoted here and later in the text as $R_{D(2)}$. For the uniform photon distribution case we use the condition

$$(N-1) \cdot D_{Earth} = D_{CRE}, \tag{6.1}$$

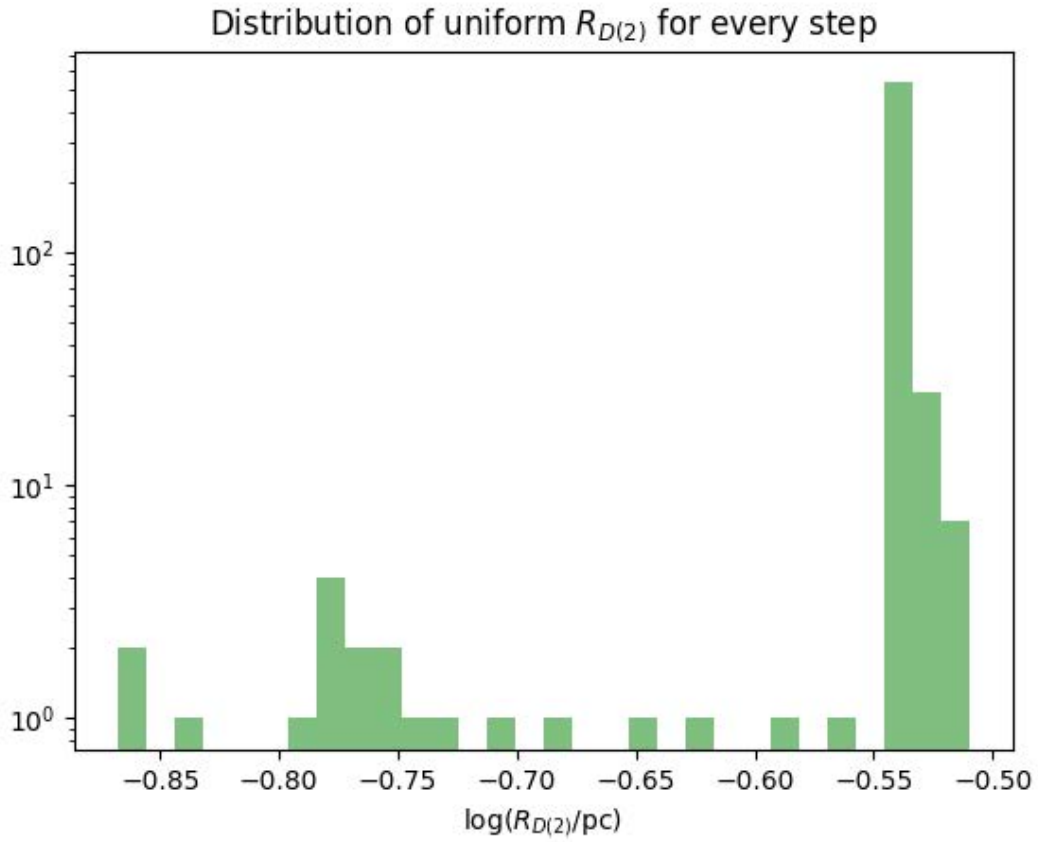

Figure 6.1: The largest distances $R_{D(2)}$ distribution for all the steps (589) with $N \geq 2$ emitted photons; the minimal and maximal values plotted are 0.135 pc and 0.309 pc, respectively.

After inserting this condition into Eq. 5.3, we get

$$R_{D(2)} = \frac{(N-1)\, D_{Earth} \cos\alpha + R_g\,(1-\cos\alpha)}{\sin\alpha}. \tag{6.2}$$

The resulting distribution of $R_{D(2)}$ is shown in Fig. 6.1.

More accurate approach to accounting for the distribution of photons along the step projection on the observer plane is keeping proportionality of the corresponding distances between the emission points of the photons and their projections on the observer plane. This situation might also not reflect the real photons distribution properly because the emitted photons have different energies and thus the energy of the electron does not reduce with a constant rate. However, this assumption is more realistic than the uniform distribution.

Hence we assume the one-to-one correspondence of the emitted photons and the photons distributed over the step projection, there is no need to calculate exact positions of the photons on the observer plane. Unchanged proportions of the corresponding distances suggest that the distance between any two neighbouring photons on the observer form

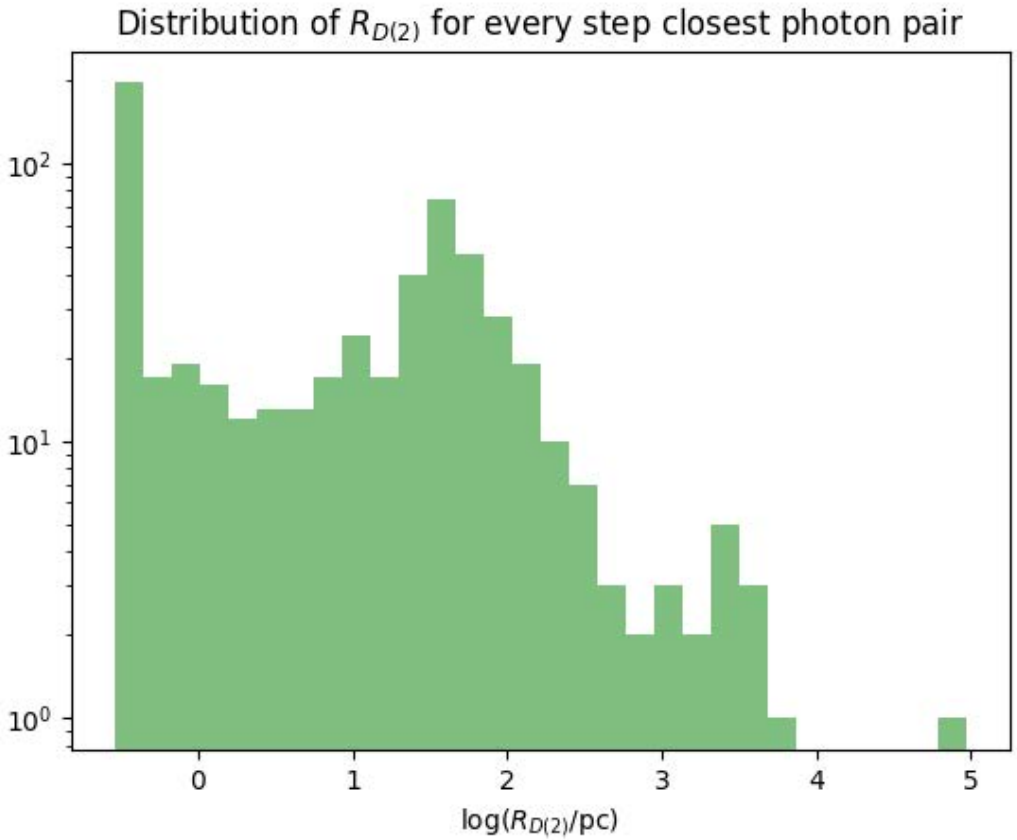

Figure 6.2: The distribution of the largest observer distances for the closest pairs of photons emitted during every electron propagation step; the minimal and maximal values plotted are 0.288 pc and 94.618 kpc, respectively.

the same fraction of the whole projection length as the ratio between the distance separating their emission points and the step length. For this reason we calculate the distance between every pair of the neighbouring photons and then demand the distance between their projection points not to exceed the Earth size, i.e.

$$\frac{D_{step}}{D_{i,i+1}} D_{Earth} = D_{CRE}, \tag{6.3}$$

where $D_{i,i+1}$ is the distance between the i-th and the (i+1)-th photons. The distance to the observer in this case is

$$R_{D(2)} = \frac{(D_{step}/D_{i,i+1})\, D_{Earth} \cos\alpha + R_g\,(1-\cos\alpha)}{\sin\alpha} \tag{6.4}$$

Potential abrupt changes of the magnetic field become even less probable and could be neglected. Among the two field values at the points of photon emission we pick the largest one and use it for calculation of the gyroradius R_g in (6.4) together with the energy at the end of the whole step. In this way ensure the computation of the minimal value of

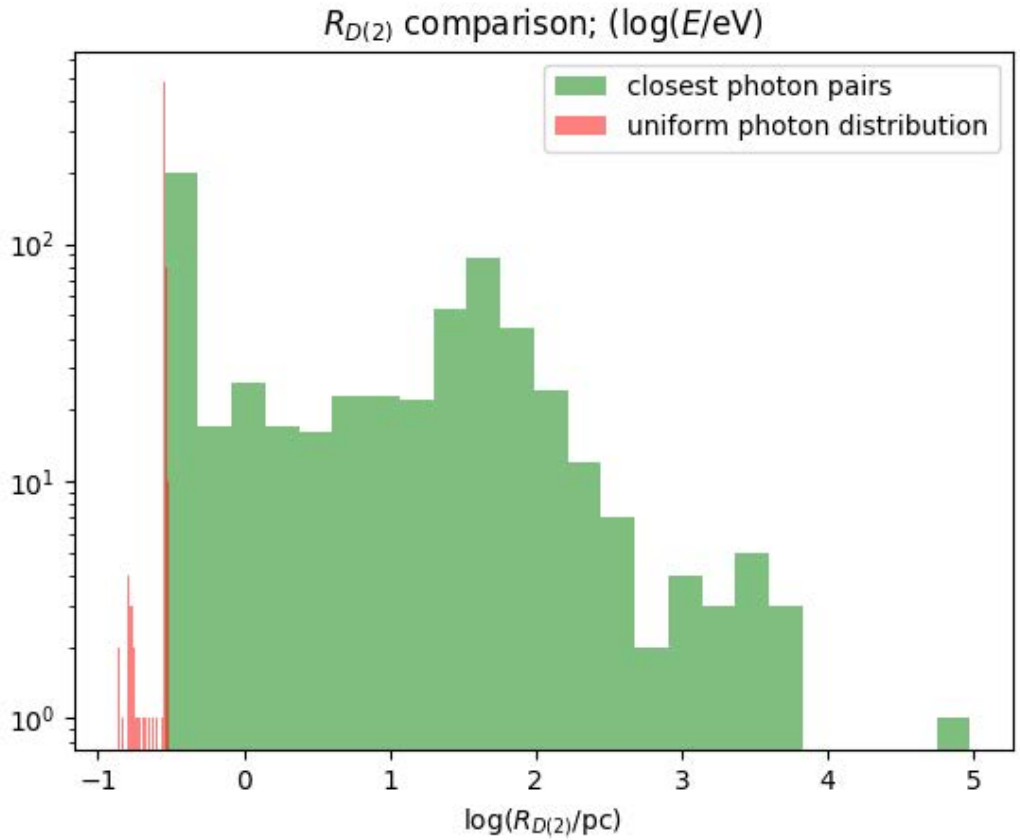

Figure 6.3: The distribution of the largest observer distances for the closest pairs of photons emitted during every electron propagation step, compared for the "uniform" and "proportional" photon distributions.

$R_{D(2)}$.

Thus, for every step of the electron propagation that N photons are emitted from, we obtain $N-1$ observer distances calculated using (6.4). The largest of them represents the most optimistic number regarding the remoteness of the observer from the emitting part of the particular step of the electron trajectory. It obviously corresponds to the closest photon pair (two photons which emission points are located at the minimal distance $D_{i,i+1}$ from each other).

The resulting distributions of $R_{D(2)}$ for the whole example run are presented in Fig. 6.2 (the "proportional distribution" case only) and Fig. 6.3 (the comparison of both approaches). Every entry on the plots corresponds to a single step of the electron propagation.

As one can see from the comparison plot (Fig. 6.3), the use of the proportional approach allows for a lot more (orders of magnitude) optimistic expectations regarding the observer distances at which the separation of two photons does not exceed the Earth size.

We also calculated observer distances for each neighboring pair of photons emitted

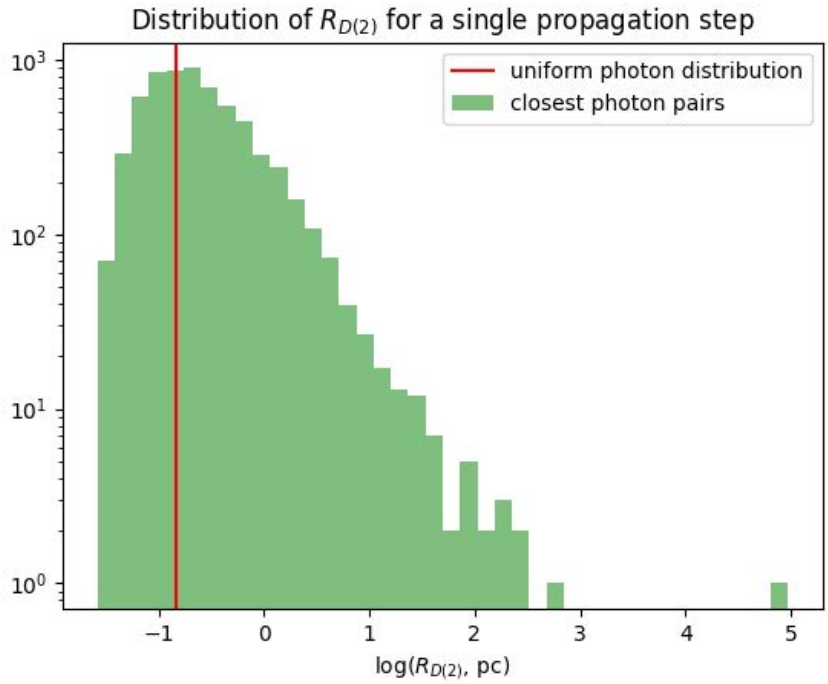

Figure 6.4: Distribution of observer distances calculated for every pair of neighbouring photons along the step 3.

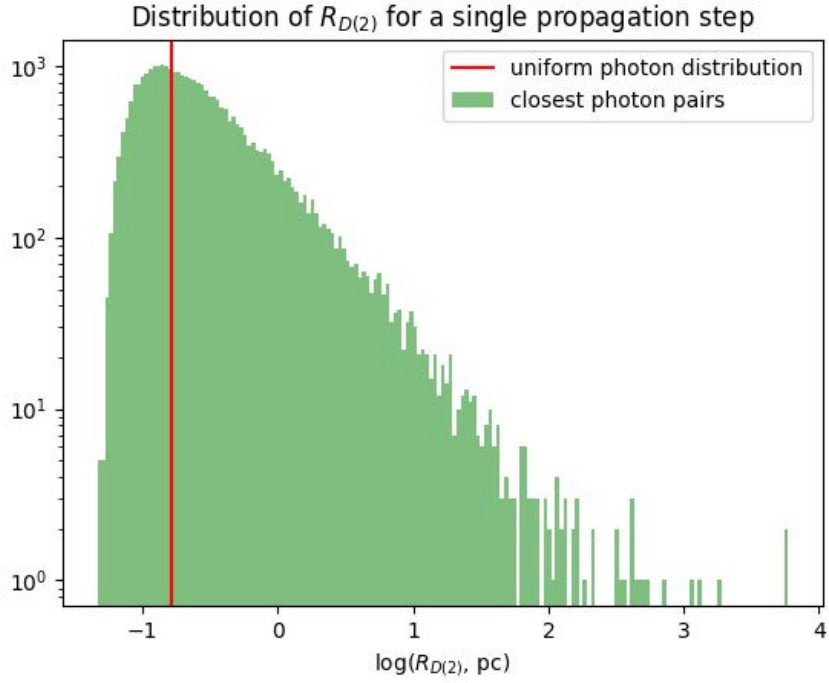

Figure 6.5: Distribution of observer distances calculated for every pair of neighbouring photons along the step 4.

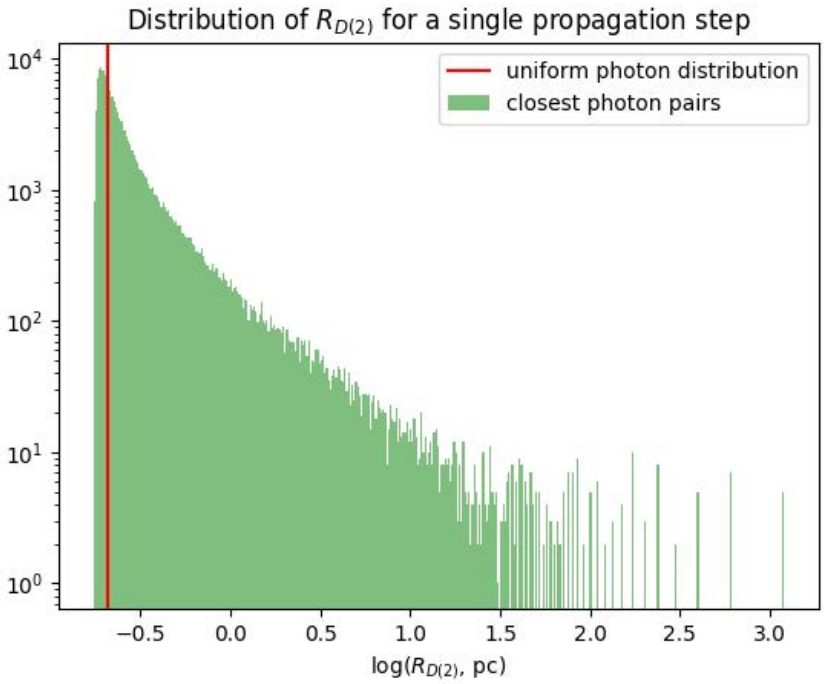

Figure 6.6: Distribution of observer distances calculated for every pair of neighbouring photons along the step 16.

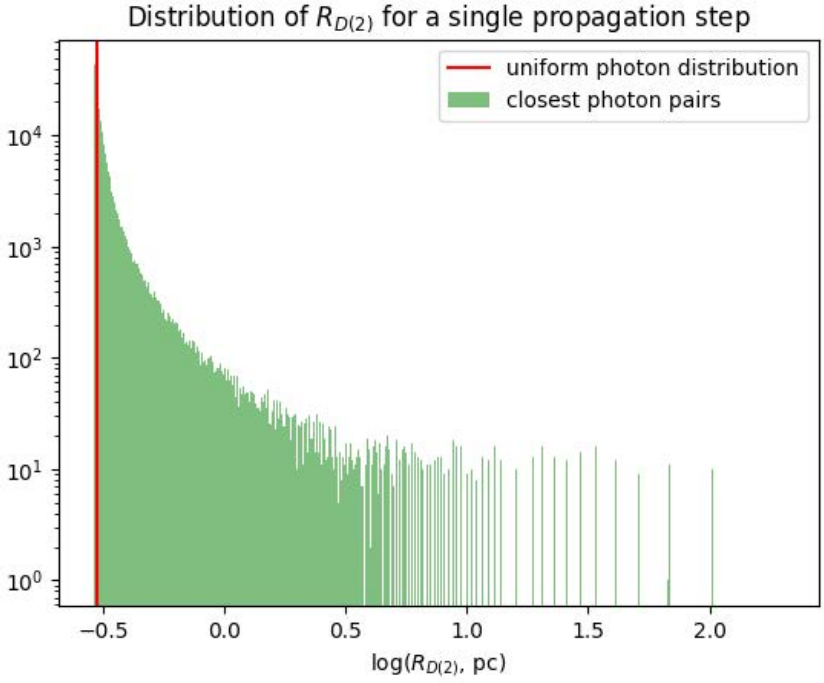

Figure 6.7: Distribution of observer distances calculated for every pair of neighbouring photons along the step 34.

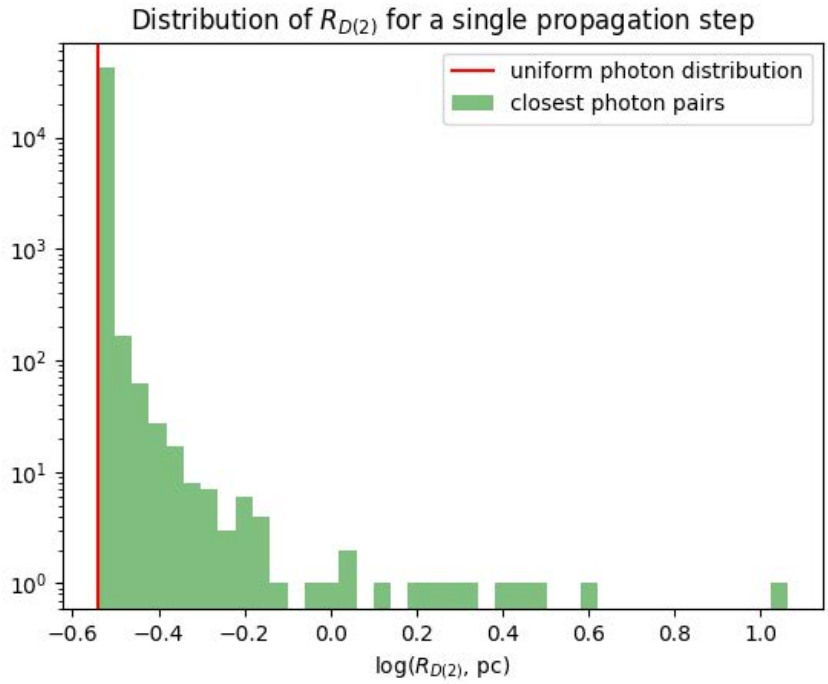

Figure 6.8: Distribution of observer distances calculated for every pair of neighbouring photons along the step 272.

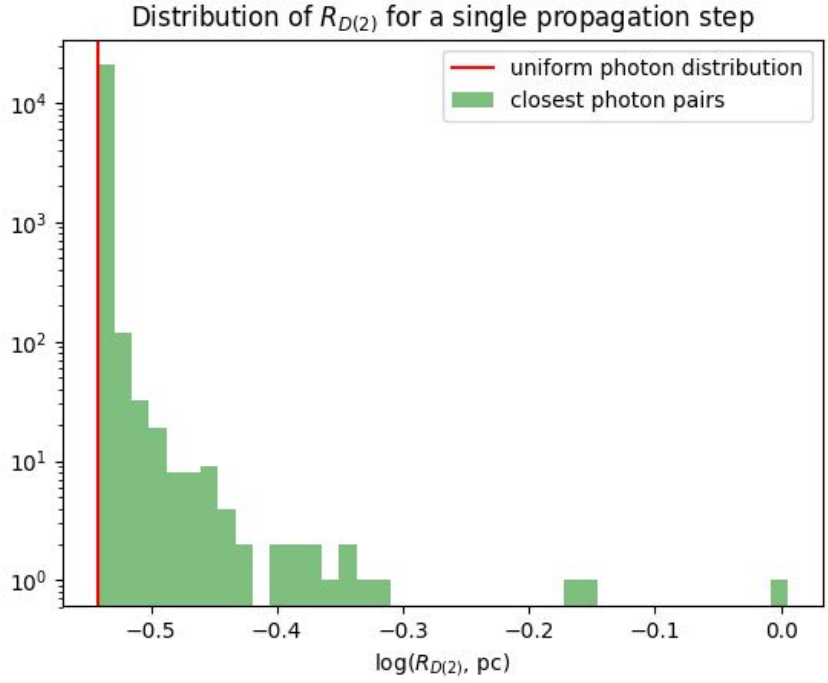

Figure 6.9: Distribution of observer distances calculated for every pair of neighbouring photons along the step 323.

Table 6.1: Information about the electron steps, plotted in Fig. 6.4-6.9. "Maximal" and "Uniform" denote proportional ("closest pair") and uniform distributions of photons over the observer surface, respectively

Fig.	Step	Maximal $R_{D(2)}$, pc	Uniform $R_{D(2)}$, pc	D_{step}, pc$\cdot 10^{-3}$	Photons emitted	B_{max}, μG	B_{av}, μG	E_{start}, PeV	E_{final}, PeV
6.4	3	$9.46 \cdot 10^4$	0.145	0.25	6270	5.55	5.55	3969.6	3922.3
6.5	4	$5.94 \cdot 10^3$	0.163	1.25	30786	5.55	5.55	3922.3	3691.2
6.6	16	$1.20 \cdot 10^3$	0.209	5.9	144509	5.54	5.53	1290.2	1173.0
6.7	34	$2.04 \cdot 10^2$	0.298	10	241821	5.48	5.48	347.4	333.2
6.8	272	11.60	0.287	10	42178	5.29	5.29	35.93	35.79
6.9	323	1.014	0.287	10	20980	5.64	5.63	29.59	29.48

along a single step. The steps with different observer distances corresponding to the closest photon pair are presented in Fig. 6.4-6.9. For comparison, each of the plots contains the value of the observer distance obtained for the uniform approach (a vertical red line). Extended information on the physics parameters of a particular step being plotted are listed in Tab. 6.1.

As one can see from the numbers comparison, the "earlier" propagation steps have a higher probability to form a more compact CRE, which leads to expansion of the horizon for its observation in the terrestrial conditions. This conclusion is consistent with expectations from the physics of a charged particle propagation in the magnetic field: higher electron energies correspond to larger trajectory gyroradii and thus to smaller deflections. On the other hand, the energy losses are also higher, which leads to more photons emitted. Along the equal sized steps larger number of photons leads to decrease of the closest point distance, which, as discussed above, expands the horizon of CRE observation at the Earth.

6.3 Multiplicity of a CRE

We also investigated the maximal number of photons within a CRE not exceeding the Earth size, provided the observer distance is set at a constant value. The proportional distribution approach allows to skip the calculation of the exact positions of the photons on the observer surface, analyzing just the coordinates of the emission points of the photons along the step. For the given observer distance R_D we first calculated the length of the propagation step part R_{win}, the projection of which equals to the Earth size. Since the correspondent distances are proportional, i.e.

$$\frac{R_{win}}{D_{step}} = \frac{D_{Earth}}{D_{CRE}}, \tag{6.5}$$

and with the use of (5.3), one can infer:

$$R_{win} = \frac{D_{Earth} D_{step} \cos\alpha}{R_D \sin\alpha - R_g (1 - \cos\alpha)} \tag{6.6}$$

After the value of R_{win} is calculated for a particular step, we "slide" the section of this length along the step, matching its beginning with all the photons consecutively, one-by-one, and calculating the number of photons within this "sliding window" at every iteration. The results for observer planes at different distances from the propagation step are summarized in Tab. 6.2. The number in a column with the largest multiplicity for a given distance is bolded.

Table 6.2: Multiplicity (maximal number of photons within the Earth size area) of a CRE for different observer distances

R_D, pc	Multiplicity					
	1	2	3	4	5	≥ 6
8500	40897780	**1**				
5000	40897778	**3**				
1000	40897729	**52**				
100	40896495	**1286**				
10	40878481	19276	**24**			
1	40644981	249505	3228	64	**1**	

The numbers presented in Tab. 6.2 show that for a 3.981 EeV electron propagating from the Galactic center there can be only a single case when two synchrotron photons emitted during a single propagation step can be separated with not more than the Earth size distance at ~ 8.5 kpc distances from the electron starting point. For the closer located observers the CRE consisting of more than two photons can also be formed.

Chapter 7

Astrophysical CRE scenarios

7.1 Galactic center as a UHECR source

There are numerous experimental evidences (see e.g. [153] and the references therein) that the compact radio source Sgr A^* at the Galactic center can be considered as a supermassive black hole. Violent processes are expected to take place in this object and its vicinity, so we assume that the physics conditions are favourable for the production of the UHE electrons and their emission outside this region. We model the UHE electron propagation in the GMF in order to apply the CRE-Pro analysis described in the previous chapter to the estimation of CRE size at the observer plane located at a distance of 8.5 kpc from the electron starting point.

We chose 11 random directions (Tab. 7.1) of the initial momentum of the electron, and varied its starting energy from 10^{17} eV to 10^{19} eV with a logarithmic step size 0.1, thus considering 21 values of energy overall. Each run of the electron with a specific starting energy in a certain direction was repeated 10 times which resulted in 2310 simulation runs in total.

We used the following input parameters for the simulation setup:

- The primary electron starting energy E_0 choice is described above
- The initial directions are listed in Tab. 7.1
- The minimum energy threshold $E_{br} = 10$ PeV
- The Galactic magnetic field described by the JF12 model
- The synchrotron radiation threshold $E_{synch} = 1$ GeV
- The propagation module (PropagationCK, 10^{-4}, 10^{-5} pc, 10^{-2} pc)

We analyzed the results of every simulation run by the CRE-Pro script, assuming the uniform distribution of photons over the observer surface, and summarized them for every

Table 7.1: The initial directions of the primary electron momentum in spherical Galactocentric coordinates (the Galactic Center is the origin point, (-1.0, 0.0, 0.0) is the direction towards the Solar System)

Spherical		Cartesian		
ϕ, deg	θ, deg	P_x	P_y	P_z
180.0000	0.0000	-1.0000	0.0000	0.0000
217.1008	21.3026	-0.7431	-0.5620	0.3633
25.3458	-40.1655	0.6906	0.3271	-0.6450
259.1134	41.2059	-0.1421	-0.7388	0.6588
28.9159	58.4257	0.4583	0.2532	0.8520
298.8458	-70.2007	0.1634	-0.2967	-0.9409
304.4253	46.1752	0.3915	-0.5712	0.7215
349.5571	-55.1722	0.5617	-0.1035	-0.8209
64.9173	23.9724	0.3874	0.8276	0.4063
69.1075	52.1377	0.2189	0.5734	0.7895
91.6777	43.2736	-0.0213	0.7278	0.6855

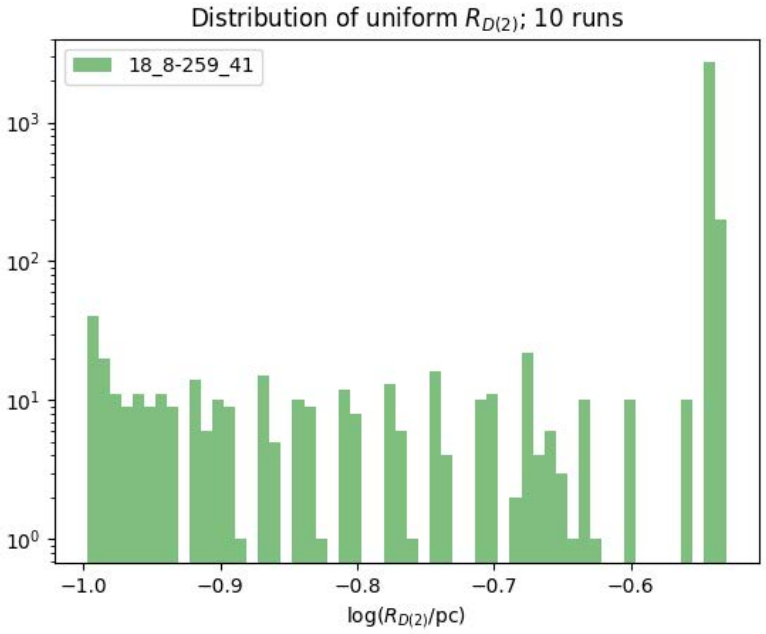

Figure 7.1: An example distribution of uniform $R_{D(2)}$ for every step of 10 runs. The electron starting energy is $\log(E_0/\text{eV})$=18.8, its initial direction is (259.1134, 41.2059) (see Tab. 7.1 and the plot legend). The maximal value plotted is 0.295 pc, the minimal is 0.100 pc, number of entries 3241.

combination of the electron starting energy and its initial direction. An example of the calculation of "N=2" horizon is presented in Fig. 7.1.

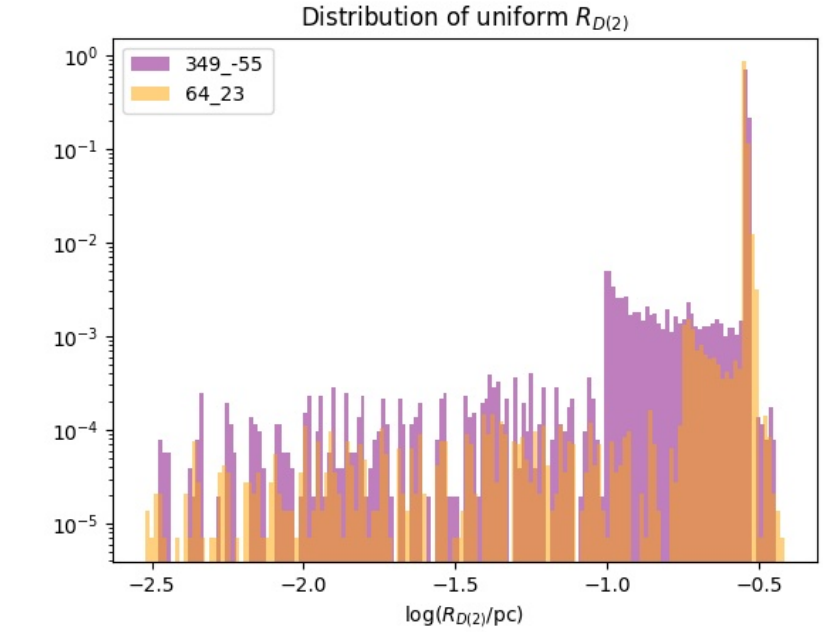

Figure 7.2: An example distribution of uniform $R_{D(2)}$ for every electron step of 210 runs (21 different values of the starting energy repeated 10 times each). Purple: 51846 entries, orange: 143567 entries. The initial directions of the electron are displayed at the plot legend (details in Tab. 7.1).

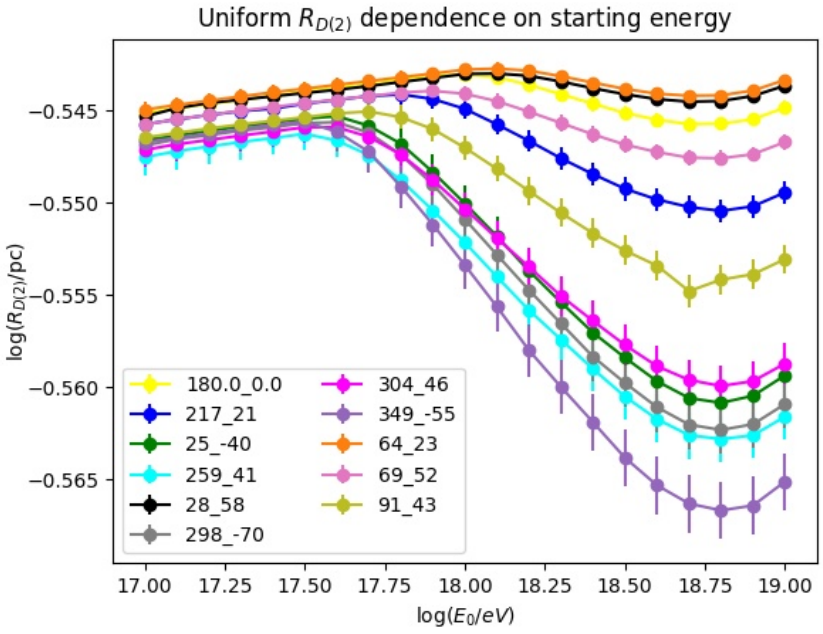

Figure 7.3: Dependence of uniform $R_{D(2)}$ on the electron starting energy. Each dot of the plot represents the "best" step - the one with the largest $R_{D(2)}$ among 10 repeated runs with the same starting energy (X-axis) in a given direction (see Tab. 7.1 and the plot legend). The largest $R_{D(2)}$ is 0.387 pc.

Since a single run of the electron contains the steps with different energies at the beginning, all the runs in a particular direction from the Galactic Center regardless of the starting energy of the electron can be analyzed jointly. We plotted the normalized distribution of $\log R_{D(2)}$ for two example directions in Fig. 7.2. A sharp peak at $\log(R_{D(2)})/pc \simeq -0.55$ followed by the populated region $-1.0 \leq \log(R_{D(2)}) \leq -0.5$ can be explained by the propagation of electrons in the "typical" conditions, i.e. in the regions with close or similar values of magnetic field strength and in the same energy range. Consecutively, energy losses of the electron along the propagation steps will be comparable (the step lengths are also matching, which is discussed in Subsection 4.3.3), that results in relatively similar numbers of photons generated along step by CRPropa. Thus, all the parameters entering Eq. 6.2, which defines $R_{D(2)}$, do not vary much, which is reflected in the plotted distribution.

The dependence of uniform $R_{D(2)}$ distribution on the electron starting energy is presented in Fig. 7.3. Each point of the plot corresponds to the mean value of $R_{D(2)}$ calculated for all the steps from 10 runs of the electron with a given starting energy (X-axis) in a specified direction (denoted by color at the plot legend). In general the behavior of the plots is consistent with the "typical conditions" explanation, which is more pronounced in the energy range $17.0 \leq \log(E/eV) \leq 17.6$. Higher starting energies introduce larger uncertainties because of smaller propagation steps which might result in significantly different numbers of emitted photons along the step. Still, due to faster energy losses at higher energies the number of steps before the electron gets into the "typical conditions" is relatively small, e.g in the (91.68; 43.27) direction (the olive plot) a 10^{19} eV electron loses its energy down to $10^{17.5}$ eV in less than 40 steps, while the photons were generated along 421 steps of the same run. The distance covered during these "higher energy steps" though should be taken into account in attempts to explain the directional dependence of the plots behavior. However, the difference between the average values of $R_{D(2)}$ even for the most distinct directions does not exceed several percent in the plotted energy range, which might be negligible in comparison with the uncertainty in the estimation of magnetic field value in the Galactic center region.

The results of calculation $R_{D(2)}$ using Eq. 6.4, in assumption that the ratios of the distances between the emission points of the photons and their positions at the observer surface are kept unchanged (the "proportional", or the "closest pair" approach), are presented in Fig. 7.4 - 7.6.

An example distribution of the closest photon pair $R_{D(2)}$ for 10 similar runs of the electron in a given direction is presented in Fig. 7.4. As one can see, the current approach to the photons distribution over the observer surface indicates that the emission of photons can take place at much higher distances from the observer, even compatible with the Galaxy size. However, the region of the "typical conditions", discussed above, can be seen on this plot as well (the local maximum at around tens of parsec). This feature is

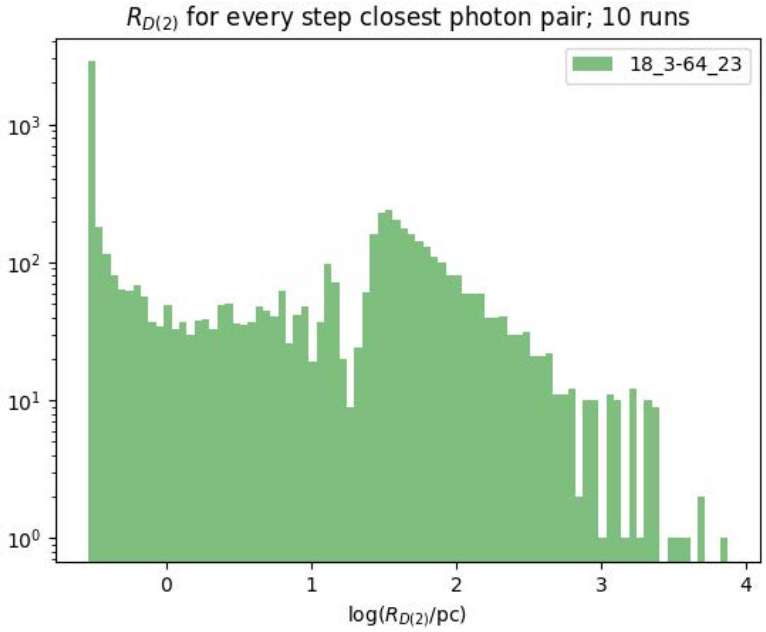

Figure 7.4: An example distribution of the closest photon pair $R_{D(2)}$ for every step of 10 runs. The electron starting energy is $\log(E_0/\text{eV})$=18.3, its initial direction is (64.9173, 23.9724) (see Tab. 7.1 and the plot legend). The maximal value plotted is 7.527 kpc, the minimal is 0.287 pc, number of entries 7059.

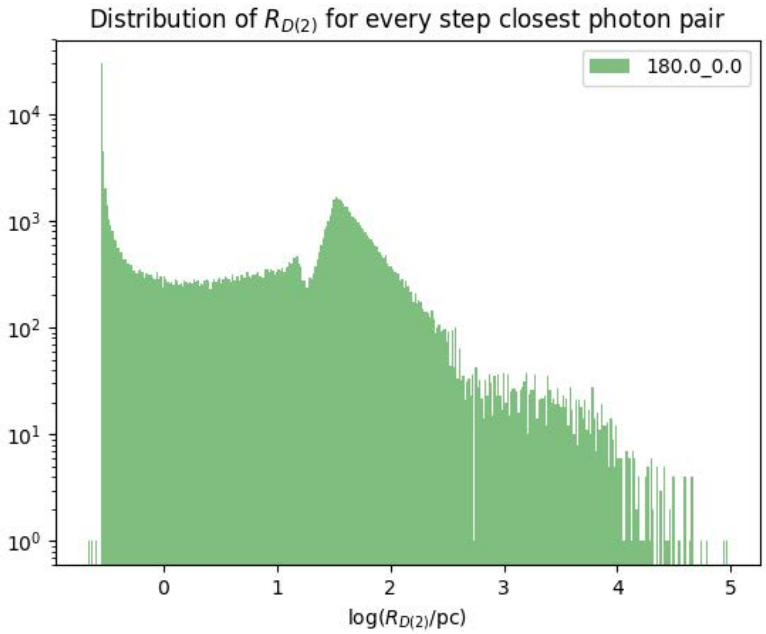

Figure 7.5: An example distribution of the closest photon pair $R_{D(2)}$ for every electron step of 210 runs (21 different values of starting energy repeated 10 times each); the electron initial direction is (180.0000, 0.0000) (see Tab. 7.1 and the plot legend). The maximal value plotted is 94.618 kpc, the minimal is 0.216 pc, number of entries 120894.

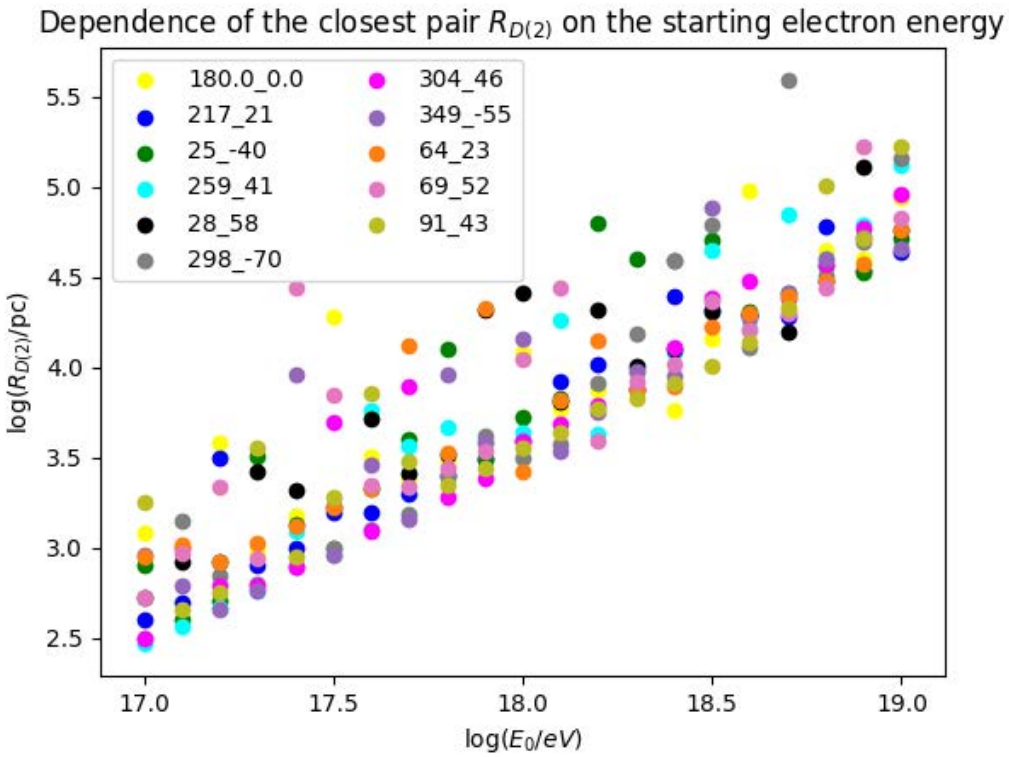

Figure 7.6: Dependence of the closest photon pair $R_{D(2)}$ on the electron starting energy. Each dot of the plots represents the "best" step - the one with the largest $R_{D(2)}$ among 10 repeated runs with the same starting energy (X-axis) in a given direction (see Tab. 7.1 and the plot legend). The largest $R_{D(2)}$ is 392.452 kpc.

typical for all the distributions of this type, which can be also shown at the cumulative plot containing all propagation steps of the electron in a given direction regardless of its starting energy (Fig. 7.5). The steps corresponding to higher electron energies are more likely to produce the closest photon pairs and, respectively, more distant CRE, as can be seen from Fig. 7.6. One can notice, that the most "optimistic" observer distance the Earth-sized CRE can originate at is around 400 kpc, which by far exceeds the Galaxy size.

The assumptions of uniform and proportional distributions of photons for the given electron starting energy and its initial direction are compared in Fig. 7.7 - 7.8. The former illustrates the results of processing 10 similar runs of the electron in a given direction, while the latter plot is cumulative and contains all 21 electron starting energies used in this study.

It could be summarized that the uniform photon distribution allows for making qualitative conclusions: the average photon pairs are not expected to form CRE observable on Earth, unless the sources (interaction origins) are very close, like the closest stars - which should happen very rarely. This result is in a sense compatible with the "state-of-the-art"

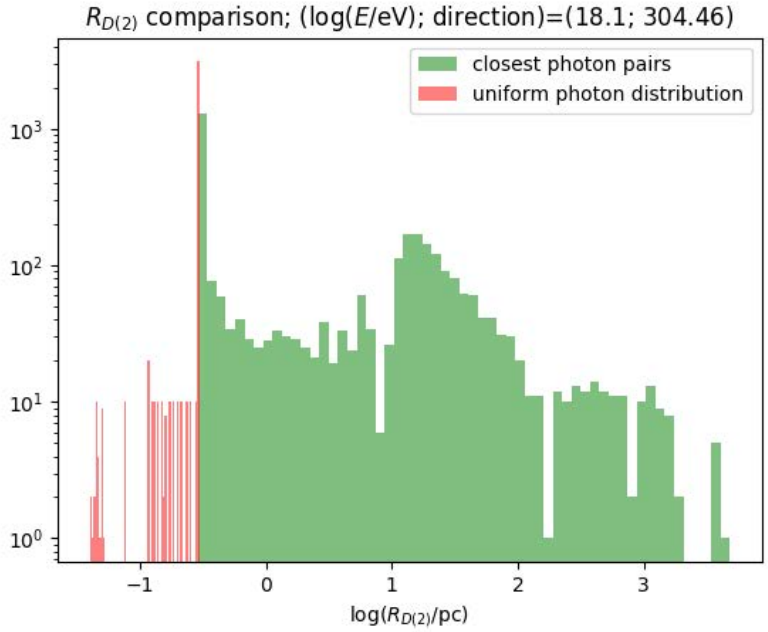

Figure 7.7: Comparison of two approaches to the $R_{D(2)}$ calculation; the electron starting energy and its initial direction are presented in the plot title (see also Tab. 7.1). The maximal value of the closest pair $R_{D(2)}$ is 4.863 kpc, the maximal value of the uniform $R_{D(2)}$ is 0.296 pc, number of entries 3301.

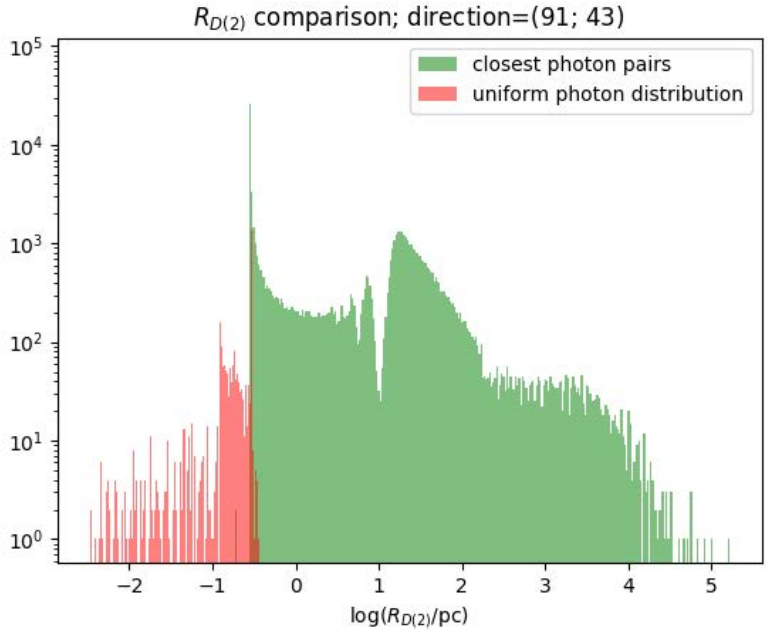

Figure 7.8: Comparison of two approaches to the $R_{D(2)}$ calculation; all the electron steps in a given direction, presented in the plot title (see also Tab. 7.1), are taken into account. The maximal value of the closest pair $R_{D(2)}$ is 167.280 kpc, the maximal value of the uniform $R_{D(2)}$ is 0.383 pc, number of entries 81751.

assumption on the "extinction" of a particle after its interaction with the background radiation. What makes the difference is the closest pair approach, which gives a lot more optimistic expectations of the distances between the emission region and the observer. One might have a chance to observe the CRE of the Earth size at distances exceeding the Galaxy size. This conclusion holds true for all the directions chosen for this set of simulations, as well as for every value of the electron starting energy from the considered range (Fig. 7.6).

7.2 Uniform distribution of galactic sources

Another hypothesis worth considering in attempts to explain origination and existence of UHECR, including UHE electrons, is already mentioned SHDM scenario. According to this theory super massive X particles (in addition to already cited references see e.g., [154]) may undergo decay or be destroyed via annihilation, which results in production of quarks and leptons. The quarks then produce jets of hadrons containing mainly pions with a small fraction of nucleons (the process known as hadronization). Decay of pions, it turn, leads to the production of photons, neutrinos and electrons. Such a scenario does not require any acceleration mechanisms and thus distinct astrophysical objects as UHECR sources. On the contrary, the interactions described above may take place elsewhere in the Galaxy, since it is believed that most of the mass in galactic halos is composed of dark matter. Correspondingly, the uniform distribution of particles within the halo or even within a cluster of galaxies is assumed within SHDM model [44].

In this context we simulated the uniform distribution of points over the Galaxy, considering the latter as the sphere of 20 kpc radius. We chose 292 random points as the origin points of 1 EeV electrons, each being initially directed towards the Solar System traversing the regions with different values of the GMF. The simulation setups for these 292 runs contained the following parameters:

- The primary electron starting energy $E_0 = 1$ EeV
- The minimum energy threshold $E_{br} = 10$ PeV
- The Galactic magnetic field described by the JF12 model
- The synchrotron radiation threshold $E_{synch} = 1$ GeV
- The propagation module (PropagationCK, 10^{-4}, 10^{-5} pc, 10^{-2} pc)

Every run has been processed with the CRE-Pro script, and the correspondent distributions of $R_{D(2)}$ were plotted. The example comparison of two approaches to the distribution of synchrotron photons over the observer surface are shown in Fig. 7.9 - 7.13

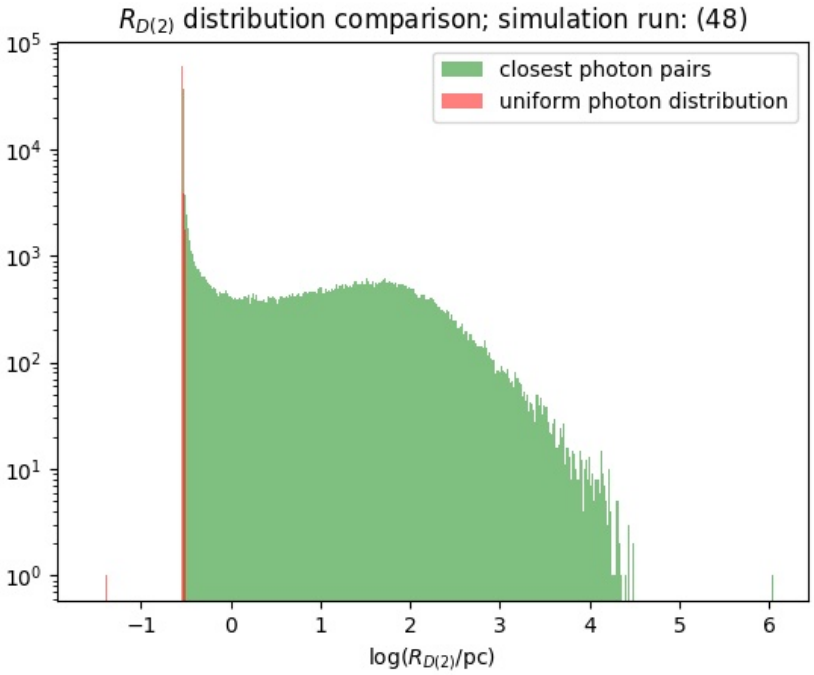

Figure 7.9: An example comparison of two approaches to the calculation of $R_{D(2)}$ for the simulation run 48 (see Tab. 7.2 for details).

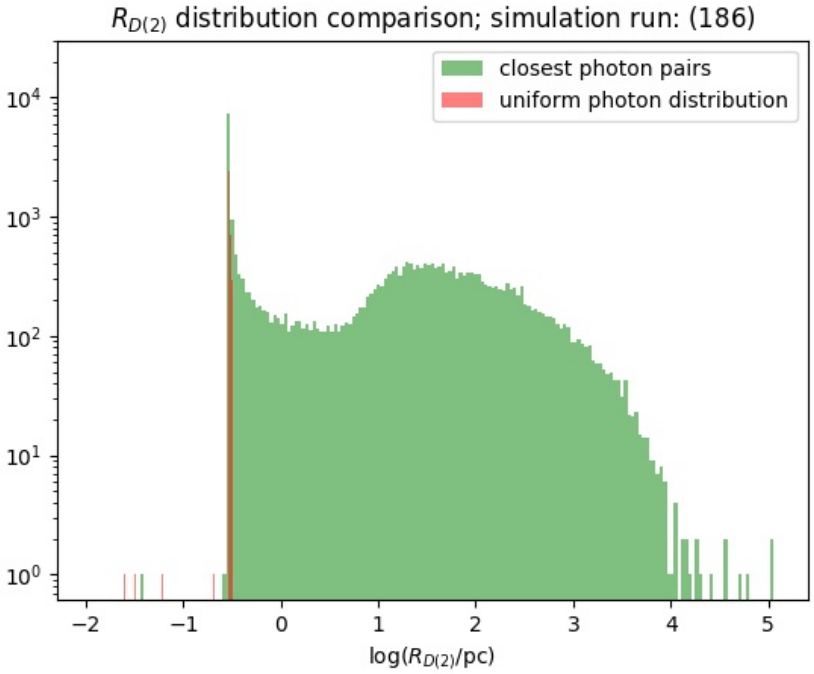

Figure 7.10: An example comparison of two approaches to the calculation of $R_{D(2)}$ for the simulation run 186 (see Tab. 7.2 for details).

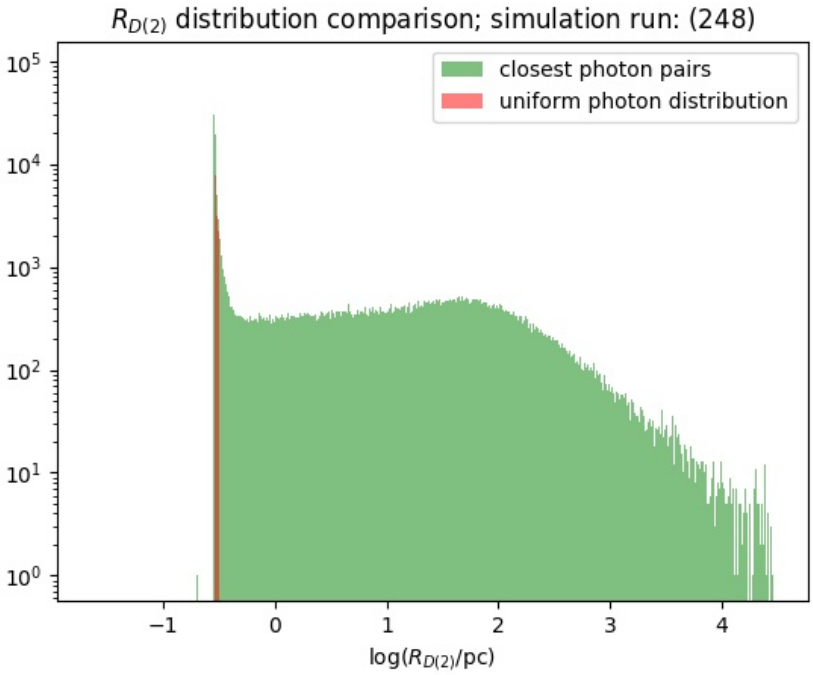

Figure 7.11: An example comparison of two approaches to the calculation of $R_{D(2)}$ for the simulation run 248 (see Tab. 7.2 for details).

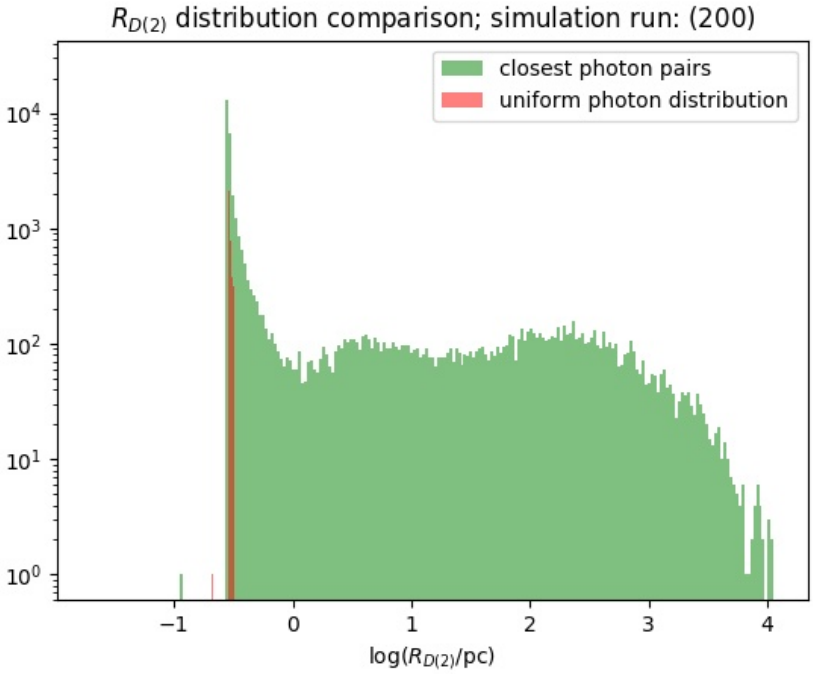

Figure 7.12: An example comparison of two approaches to the calculation of $R_{D(2)}$ for the simulation run 200 (see Tab. 7.2 for details).

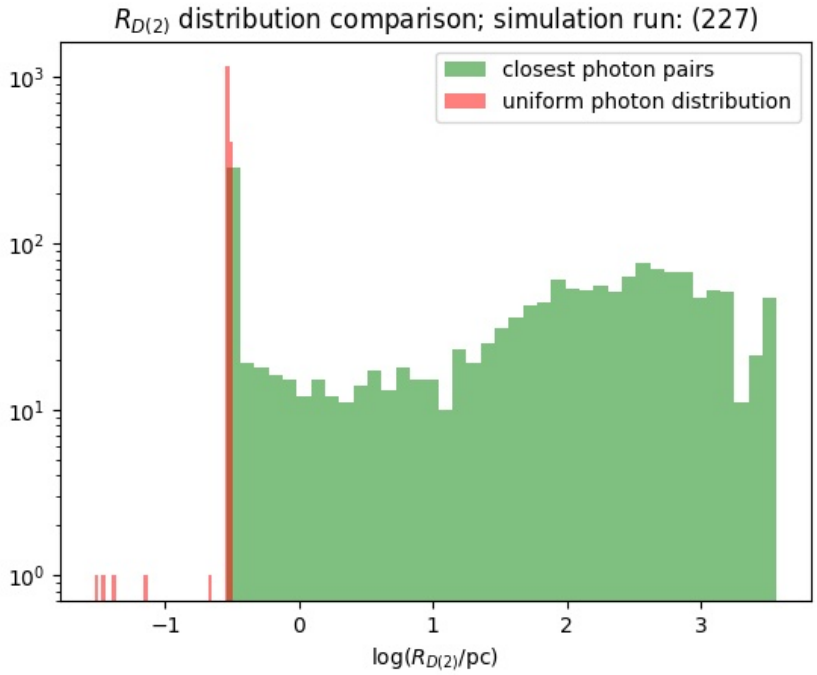

Figure 7.13: An example comparison of two approaches to the calculation of $R_{D(2)}$ for the simulation run 227 (see Tab. 7.2 for details).

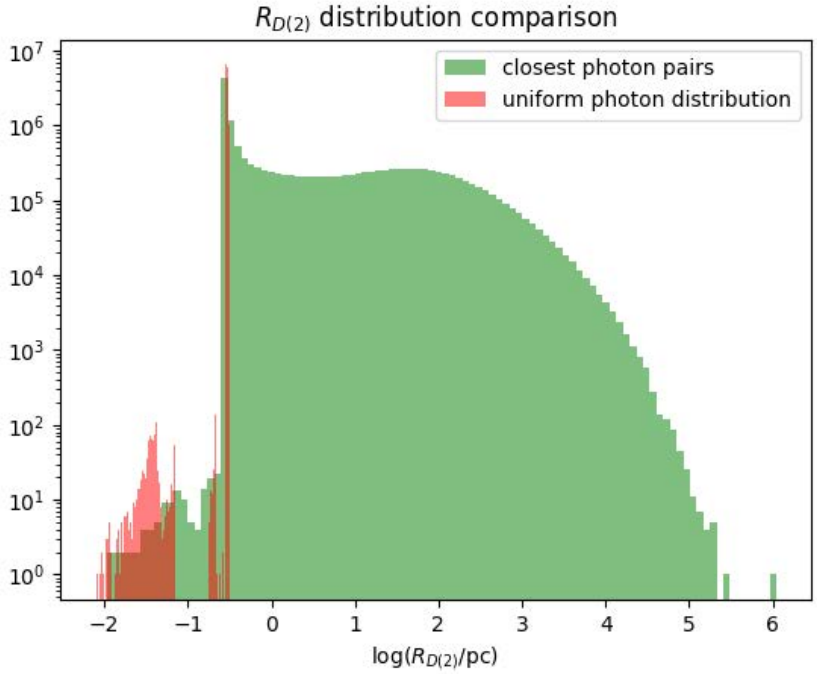

Figure 7.14: Comparison of two approaches to the calculation of $R_{D(2)}$. The number of entries 15318555, maximal value of the closest photon pair $R_{D(2)}$ is 1.129 Mpc, the maximal value of uniform $R_{D(2)}$ is 0.321 pc.

for 5 different simulation runs, corresponding to different positions of the source (the electron starting point). Unlike the Galactic Center scenario (Sec. 7.1), the random allocation of sources over the Galaxy barely allows for unambiguous explanation of the closest pair $R_{D(2)}$ distribution in all cases. The number of steps in different runs varies in a wide range, from $\sim 10^2$ to $\sim 10^5$ (the latter situation is expected to occur as the electron propagates through the regions with a small transverse component of the magnetic field). Correspondingly, there is little sense in speaking about the "typical conditions", as they might be far from matching not only during different runs, but within a single run as well, for instance if the trajectory of the electron is long enough.

The cumulative plot with all the directions put into one data set (Fig. 7.14) does not indicate significant difference from the previous scenario regarding the uniform distribution of photons over the observer surface qualitatively, as well as the average $R_{D(2)}$ value of 0.292 pc ($\log(R_{D(2)} = -0.535)$ is similar to the corresponding values plotted in Fig. 7.3. The smooth distribution of the closest pairs $R_{D(2)}$ does not contain a pronounced local maximum at tens of parsec, but rather a wide local maximum at around 100 pc. One should also note that numerous values plotted in Fig. 7.14 match and even exceed the size of the Galaxy.

Table 7.2: Parameters of the simulation runs illustrated in Fig. 7.9 - 7.13. 1 EeV primary electron is initially directed towards the Solar System in all cases.

Run	Cartesian coordinates of the source			Entries	Maximal $R_{D(2)}$, pc
	x, pc	y, pc	z, pc		
48	$1.197 \cdot 10^4$	$-1.407 \cdot 10^2$	$1.232 \cdot 10^4$	130464	$1.129 \cdot 10^6$
186	$-1.435 \cdot 10^4$	$2.186 \cdot 10^3$	$-1.037 \cdot 10^4$	31332	$1.150 \cdot 10^5$
248	$-5.584 \cdot 10^2$	$-1.765 \cdot 10^4$	$9.103 \cdot 10^3$	151155	$2.945 \cdot 10^4$
200	$-2.518 \cdot 10^3$	$1.006 \cdot 10^4$	$5.501 \cdot 10^3$	38940	$1.143 \cdot 10^4$
227	$-1573 \cdot 10^3$	$1.048 \cdot 10^4$	$4.500 \cdot 10^2$	1566	$3.683 \cdot 10^3$

The information on the simulation runs demonstrated in Fig. 7.9 - 7.13 is presented in Tab. 7.2.

7.3 Discussion of the results

We have simulated synchrotron emission of UHE electrons during their propagation in the GMF, considering two toy models of distribution of their sources. They are, namely, Galactic Center as a UHECR source (Sec. 7.1), and the uniform distribution of galactic sources (Sec. 7.2), which might take place within non-acceleration astrophysical scenarios of UHECR origin. The simulation results were processed by the CRE-Pro script (Ch. 5) in order to estimate the sizes of resultant CRE and, consecutively, the distances (CRE horizon) potentially observable CRE could arrive from. The results obtained for aforementioned scenarios are compared in Fig. (7.15), which is a normalized histogram of the

$R_{D(2)}$ values (Eq. 6.4) calculated for the closest photon pairs of every step of the primary electron propagation. The starting energy of primary electrons in each of the scenarios is 1 EeV.

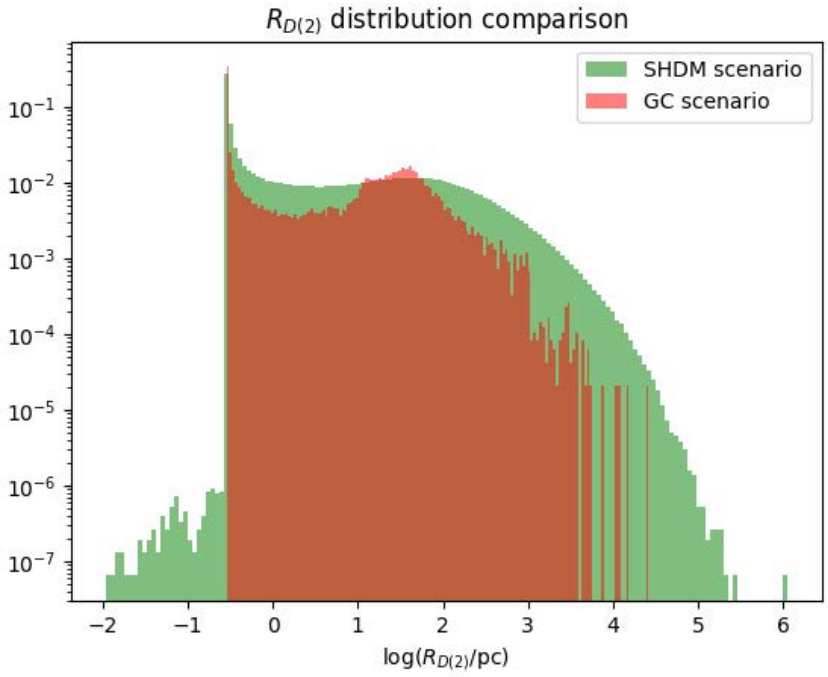

Figure 7.15: Comparison of two scenarios of UHECR sources distribution. The number of entries for uniform distribution scenario is 15318555, maximal value of the closest photon pair $R_{D(2)}$ is 1.129 Mpc. For the Galactic center scenario the plot contains 48339 entries, with the maximal value of $R_{D(2)}$ around 26.146 kpc.

As one can see from the plot, CRE with two photons with the distance less than the Earth diameter between them have chances to be formed even at distance comparable with the Galactic size (∼tens of kpc in Galactic center source model) or exceeding it (∼1 Mpc in case the sources are uniformly distributed over the Galaxy). The latter case might allow for some extragalactic sources to initiate the observable CRE, but the study of extragalactic physics conditions in the CRE context requires additional research.

Chapter 8

Summary and outlook

In the thesis we studied the formation of cosmic-ray ensembles and investigated their propagation in space, keeping in mind the synchrotron emission of charged particles in the magnetic field as the main source of the product photons, which are constituents of the CRE. Our study was aimed towards simulation of CRE footprint shape and size at the observer surface in order to estimate the possibility of CRE observation at the Earth (or another feasible in the observable future surface in the human technosphere). The main method of study was computer simulations with the publicly available Monte-Carlo framework CRPropa. We show that regarding the tasks of our research this code performance could be improved in terms of the effective use of hardware resources, in case the propagation of secondary photons is substituted with the external simulation of their distribution at the observer surface.

We have produced a universal script named CRE-Pro which allows calculating the shape and size of the CRE footprint at the custom observer surface. Due to the fact that the photons propagate along the straight trajectories, CRE-Pro skips their propagation and instead provides their distribution at the observer surface. This approach allows at least to save the computing time; moreover, in cases when the number of the product particles is large enough to cause memory problems, it can be one of the practical ways to preserve the job from being terminated. Another important feature of the CRE-Pro is its flexibility, because having the information on the photons emission stored in the output file is enough for not repeating CRPropa simulations for different observers in case of such a need - the same parameters could be reused for any surface, which has to be predefined no longer. Together with the possibility of using the CRE-Pro algorithm universally - not only for processing CRPropa outputs, but also for any similar code output as well - its advantages mentioned above make it a potentially useful tool for a study of CRE.

With the use of this script astrophysical scenarios of the CRE formation could be analyzed which is demonstrated in the thesis. The results presented here for the first time show that there might be a chance of observing a CRE originating from synchrotron radiation occurring even as far as 10 Mpc away from the Earth. This means that even "con-

ventional" and abundant electromagnetic processes like synchrotron radiation in galactic magnetic fields are expected to generate CRE reaching the Earth. The main conclusion of the research presented here could be formulated as follows: some fraction of gamma rays of energies larger than 1 GeV reach the Earth as groups, here named cosmic-ray ensembles, and this result opens up a new research channel focused of observation and studying large scale cosmic ray correlations. This conclusion is one of the cornerstones of the physics program defined by the Cosmic-Ray Extremely Distributed Observatory, as highlighted in Ref. [20]. Determining feasibility and cost of CRE observations requires another investigation which is now being carried out within the CREDO Collaboration, to complement the work described in this thesis. If CRE can be observed, it will open a new information channel about the Universe, with a wide plausible impact on astroparticle physics and beyond. This impact would include e.g. an ability to independently confirm or constrain physics scenarios concerning fundamental processes occurring at energies beyond the reach of man-made accelerators, astrophysical multi-messenger applications, and unprecedented interdisciplinary opportunities, as also explained in Ref. [20].

The current work has been focused only on a few aspects of more general CRE-oriented research, while many important questions have been left untouched since they require more thorough and complex study. The list includes propagation in the extragalactic field (the photons trajectories are linear, and two particles emitted within a narrow open angle could potentially form a localized CRE). The accurate account for the synchrotron emission opening angle will enlarge the simulated CRE size, since instead of a dot, like it is assumed in the CRE-Pro, every photon will land on the observer surface within the area confined in an ellipse, which will turn the section into a prolate ellipse. If induced by a UHE photon, the electromagnetic cascade will consist at some stage of many electrons and positrons, which in turn will undergo interactions with the backgrounds and emit synchrotron photons, so that the product photons originated from different parent particles will mix and the picture of their propagation as well as the shape and size of the footprint of such a cascade will be a lot more complex than the simplest model we use in the present work. More complex astrophysical scenarios, e.g. strong magnetic fields, should be also tested with respect to the plausible processes responsible for the origination of CRE. To study the probability of CRE observation the detector response should be simulated, which will likely result in the estimation of shape, size and cost of the detector array suitable for the CRE-oriented research. This list might be incomplete, because entering the untouched domain (like the CRE channel) always leaves space for unpredictable discoveries as well as drawbacks, leading to dynamic changes of the research plan.

Appendix A

Selected technical aspects of simulations with CRPropa

A.1 Post-processing of the CRPropa output

In order to get a detailed information on the cosmic-ray ensemble from the CRPropa simulation, one has to configure the output enabling all the steps of every particle forming the cascade to be written down. The size of the resultant output file constitutes the main difficulty for processing it in a straightforward way. Even when considering the synchrotron emission as the only interaction producing secondary particles, like it is typically done in the thesis, the size of the output file is already large enough to make its reading line-by-line a time consuming task.

For example, in case the primary electron energy is chosen in the $\sim$ EeV range, one can expect as many as $\sim 10^6$ secondary $\sim$ TeV particles to be produced. This problem gets more and more pronounced with an increasing difference between the starting energy of the primary and threshold energy for the product particles. For instance, in case of the synchrotron radiation threshold $E^{min}_{synch} = 1$ GeV for a $\sim$ EeV primary electrons (Chapters 6 - 7), the typical output file is $\sim$10 Gb, $\sim$ 50 million lines large and it could barely be handled according to the purposes of the thesis without certain preliminary steps. These steps are aimed at preparation of the output file to its further processing with the CRE-Pro script (5) with a significant reduction of the computational time.

Even the simplest shell commands like "*awk*", "*grep*", "*head*" etc. cause system response long enough when applied to a huge file on a standard PC. Yet, the order of records (lines) in the output file allows to propose a trick to solve the problem. The information on a particle propagation is written down step by step, thus occupying several consecutive lines of the output file. After the particle is stopped, the steps of the next one are started to be written down, and this process is repeated until the last particle is stopped. The output file, accordingly, consists of the "blocks" containing full information on a certain particle

propagation from its first step till the last one. The first block saved this way describes the propagation of the primary particle, while the next blocks track all the product particles, originated due to the interactions of the primary with the environment specified in the code, one by one. The blocks can be distinguished by the particles serial number or by the energy and type of the parent particle (as it was done in this work).

The order the blocks are written in, the number of lines in each of them as well as the number of the first and the last line of the block in the initial file, can be defined by applying the "*uniq -c*" shell command to the latter to count the number of occurrences of a duplicate entry, e.g. the energy of a parent particle, in it. This information is in principle enough to split the initial file into the parts corresponding to the blocks, using the combinations of "*head*" and "*tail*" shell commands with relevant flags. Still, one more time-saving operation could be performed before extracting the blocks.

Any file can be divided into smaller parts using "*split*" shell command, which allows, among the other options, to create the parts with a given number of lines in each one. This allows to replace navigation over the large file with navigation over its smaller parts of the size chosen by the user. The time gain could be illustrated with the following simple example. Suppose the file containing 1520 lines is split into parts containing 100 lines each, which results in 16 parts ($15 \times 100 + 20$). Suppose also that there are only 3 blocks in it with 380, 250 and 890 lines, correspondingly. The first block occupies 3 first "100-lined" parts and a fragment (starting from the beginning to line 80) of the 4-th such part, the second block starts in the 4-th part (line 81) and ends in the 7-th (line 30), and the third block occupies a fragment (from line 31 to the end) of the 7-th part and all the remaining parts, from the 8-th to the 16-th. The first entry of the second block is thus the 381-th line of the large file or the 81-th line of the 4-th part. Manipulating the number of a block and its size as well as the number of "parts" of the pre-defined size allows for around 100 times faster navigation over the split file than over the initial one.

It should be noted, that splitting of the large file is comparable in duration with the system response to a single shell command be the latter applied to the initial file. For instance, the file "output.txt" containing around 1.6 billion lines (such file sizes are typical for large CRE obtained when many interactions are included into the simulation setup) is split into 10 million lines parts in around 35 minutes. On the other hand, the operation

awk 'NR=1000000000' output.txt

(the extraction of a single line with a known number from the file) is performed in around 39 minutes. Splitting of the same file into 100 million lines parts takes around 50 minutes, while the simplest calculation of the number of lines in the file

wc -l output.txt

takes around 26 minutes. However, once the large file is split, the navigation over its parts causes time delays no longer.

A.2 Example CRPropa output

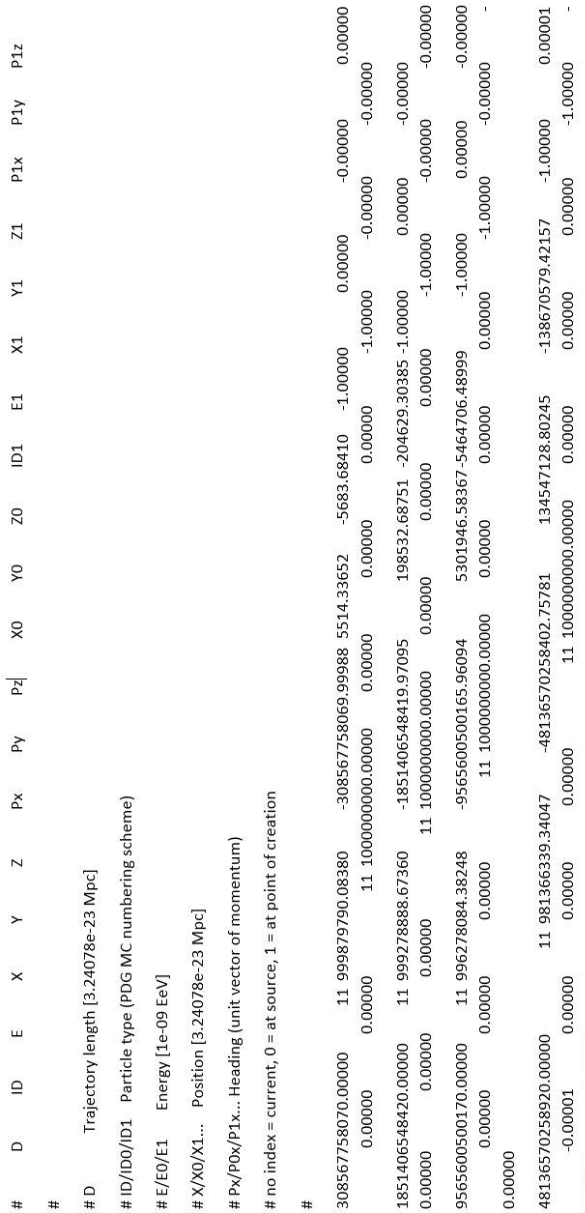

```
#       D      ID      E      X      Y      Z      Px      Py      Pz|     X0      Y0      Z0     ID1     E1     X1     Y1     Z1     P1x     P1y     P1z
#
# D       Trajectory length [3.24078e-23 Mpc]
# ID/ID0/ID1   Particle type (PDG MC numbering scheme)
# E/E0/E1     Energy [1e-09 EeV]
# X/X0/X1...   Position [3.24078e-23 Mpc]
# Px/P0x/P1x...Heading (unit vector of momentum)
# no index = current, 0 = at source, 1 = at point of creation
#
308567758070.00000     11 999879790.08380  -308567758069.99988  5514.33652  -5683.68410  -1.00000      0.00000     -0.00000     -0.00000      0.00000
         0.00000      0.00000          11 1000000000.00000     0.00000      0.00000      0.00000     -1.00000     -0.00000     -0.00000
1851406548420.00000     11 999278888.67360  -1851406548419.97095     198532.68751  -204629.30385 -1.00000      0.00000     -0.00000
0.00000      0.00000      0.00000          11 1000000000.00000     0.00000      0.00000      0.00000     -1.00000     -0.00000     -0.00000
956560050170.00000     11 996278084.38248  -956560050165.96094     5301946.58367-5464706.48999     -1.00000      0.00000     -0.00000
         0.00000      0.00000      0.00000          11 1000000000.00000     0.00000      0.00000      0.00000     -1.00000     -0.00000     -
0.00000
481365702589 20.00000     11 981366339.34047  -481365702584 02.75781     134547128.80245  -138670579.42157     -1.00000      0.00001
        -0.00001      0.00000      0.00000      0.00000          11 1000000000.00000     0.00000      0.00000      0.00000     -1.00000     -
0.00000     -0.00000
```

Figure A.1: Example CRPropa output.

A.3 CRPropa steering card example

The following piece of pseudocode is an example of a steering card which simulates the propagation of an electron in a uniform magnetic field of 200 nG strength (4.3.3).

```
import os
from crpropa import *

dir_path = os.path.dirname(os.path.realpath(__file__))

#parameters
E_0 = 1.0 #EeV; the energy of the primary particle
E_br = 1.0 #GeV; the breaking condition
r = 0.2 #parsec; the radius of the observer sphere

#magnetic field
ConstMagVec = Vector3d(0.0*nG,0.0*nG,200.0*nG)
B = UniformMagneticField(ConstMagVec)

# simulation: a sequence of modules
sim = ModuleList()

#propagation
sim.add(PropagationCK(B,1e-4, 1e-7 * parsec, 1e-4 * parsec))

#Synchrotron radiation; optional secondaries: photons
synch = SynchrotronRadiation(B,True)
synch.setSecondaryThreshold(1*GeV)
sim.add(synch)

#breaking condition
sim.add( MinimumEnergy( E_br * GeV) )

#observer
obs = Observer()
obs.add(ObserverLargeSphere(Vector3d(0.,0.,0.),r * parsec))
sim.add(obs)

#output
t = TextOutput( dir_path+'/fullOutput.txt',Output.Everything)
```

```
t.disable(Output.RedshiftColumn)
t.disable(Output.SerialNumberColumn)
t.disable(Output.SourceIdColumn)
t.disable(Output.SourceEnergyColumn)
t.disable(Output.SourcePositionColumn)
t.disable(Output.SourceDirectionColumn)
sim.add(t)
#units
t.setLengthScale(meter)
t.setEnergyScale(GeV)

#source
source = Source()
source.add(SourceParticleType(11)) #electron
source.add(SourceEnergy(E_0 * EeV)) #initial energy
source.add(SourcePosition(Vector3d(0.,0.,0.))) #starting
   position
source.add(SourceDirection(Vector3d(1.,0.,0.))) #initial
   direction of the primary particle
sim.run(source, 1, True) #1 particle is propagated
t.close()
```

A.4 Coordinate problem

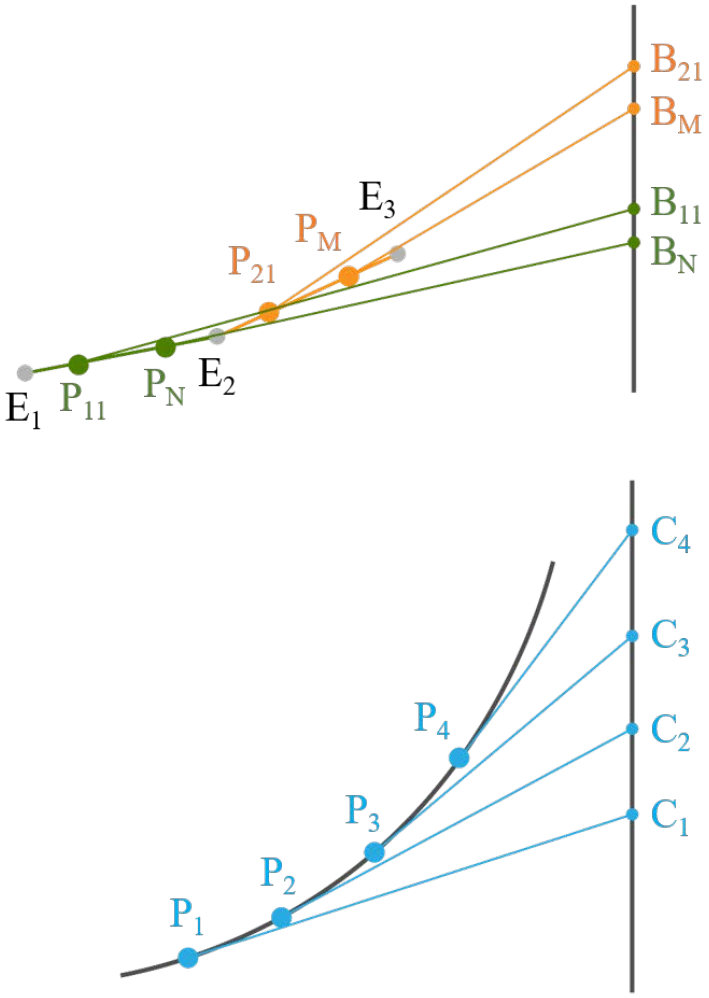

Figure A.2: Illustration of distribution of the synchrotron photons over the observer surface. Top: in CRPropa, Bottom: in the CRE-Pro. The electron propagates from the bottom left towards the top right in both cases.

We compared the distribution of synchrotron photons emission points along the electron propagation step (4.3.3) with the distribution of the same photons on the observer surface. It turned out that the photon emitted closer to the beginning of the step is deflected more than the photons emitted after it, vice versa - the deflection of the photon emitted closer to the step end is the smallest of all the photons. This situation is schematically illustrated in Fig. A.2, where two consecutive steps of the electron trajectory, namely, E_1E_2 and E_2E_3 are shown. Suppose there are N photons emitted along the

step E_1E_2 and M photons - along E_2E_3. We show only the first and the last photons of every step not to overload the illustration. Such a distribution obtained by CRPropa (top panel) does not seem to be logical, and was reported by the author of the thesis as a possible CRPropa bug, requiring more detailed explanation by CRPropa developers. Meanwhile, CRE-Pro approach (Chapter 5), reflected in the bottom panel, seems to be more realistic, at least qualitatively.

Appendix B

Selected parts of the CRE-pro code with description

B.1 Program Summary

Table B.1: Summary of the CRE-Pro script

Title of the program	CRE-Pro
Program obtainable from	oleksandr.sushchov@ifj.edu.pl
Computer on which the program was tested	Intel Core i7-6700HQ CPU@ 2.60 GHz
Operating system	Linux Ubuntu
Programming languages	Python 2.7, Bash
Nature of physics problem	Distribution of synchrotron photons emitted during a single propagation step of a UHE electron in the magnetic field
Method of solution	Geometrical projecting of the propagation step into a plane (Fig. 5.1)
Restrictions	The propagation step should not cross the plane, otherwise it's projection length is set to zero

B.2 Files included in the distribution

The CRE-Pro code consists of the following files:

- MC_script.py
  contains the main procedure obtaining the CRE size as well as printing the step summary into the output file

- func.py
  contains the functions needed for the calculations

- multiplicity.py
  calculates the maximal number of neighbouring photons contained within a CRE on a certain observer distance (optional)

- split.sh
  ensures post-processing of the CRPropa output file to prepare it for the CRE-Pro operation (see Section B.3).

- sum_check.py
  a supporting script which helps splitting

B.3 Input and output data

The input data is read from the result of the CRPropa3 output file *fullOutput.txt* post-processing, performed with the *split.sh* file. This file splits *fullOutput.txt* into the "electron" part, which contains only the steps of the primary electron until it is stopped, and the parts containing the photons emitted during every single propagation step of the electron. This data is stored in the files in the same directory with the CRE-Pro files listed in (B.2):

- *11.txt*
  the "electron" part

- *steps/sfile_energy.txt*,
  photons emitted along every step, where *energy* denotes the electron energy at the end of the step, and the photons are sorted with respect to the order of their emission.

The output data is also stored in the same directory in the following files:

- *results.txt*
  general information on every propagation step, such as the energy of the electron at the end of the step E, maximal magnetic field B_{max}, average magnetic field B_{av}, number of photons emitted N, step length D_{step}, logarithm of the "N=2" horizon $\log R_{D(2)}$ and the angular step size α (see Chapter 6 for details).

- *pair_ dist/sfile_ energy.txt*,
  logarithm of distances between every pair of neighbouring photons emitted along the step.

In case of calculation of the number of the photons within a CRE of the Earth size at a certain observer distance, *multiplicity.py* should be run from the same working directory. The input files are the same, while the output is stored in the files *dir/sfile_ energy.txt*, where *dir* is the folder which has to be created in the working directory in advance, and every file contains the multiplicity, sliding over all the photons emitted along a given step, one-by-one.

Bibliography

[1] V. F. Hess. Über Beobachtungen der durchdringenden Strahlung bei sieben Freiballonfahrten. *Physikalische Zeitschrift*. 12 (Nov. 1912), pp. 1084–1091.

[2] Todor Stanev. *High Energy Cosmic Rays*. Jan. 2010. DOI: 10.1007/978-3-540-85148-6.

[3] P. Sokolsky. Final Results from the High solution Fly's Eye (HiRes) Experiment. *Nuclear Physics B - Proceedings Supplements* [online]. 212-213 (2011). Proceedings of the Cosmic Ray International Seminars (CRIS 2010), pp. 74–78. ISSN: 0920-5632. DOI: https://doi.org/10.1016/j.nuclphysbps.2011.03.010. Available from: http://www.sciencedirect.com/science/article/pii/S0920563211000430.

[4] The Pierre Auger Cosmic Ray Observatory. *Nuclear Instruments and Methods in Physics Research Section A: Accelerators, Spectrometers, Detectors and Associated Equipment* [online]. 798 (2015), pp. 172–213. ISSN: 0168-9002. DOI: https://doi.org/10.1016/j.nima.2015.06.058. Available from: http://www.sciencedirect.com/science/article/pii/S0168900215008086.

[5] Ogio, Shoichi. Telescope Array Experiment. *EPJ Web Conf.* [online]. 208 (2019), p. 08002. DOI: 10.1051/epjconf/201920808002. Available from: https://doi.org/10.1051/epjconf/201920808002.

[6] Julia Becker Tjus and Lukas Merten. Closing in on the origin of Galactic cosmic rays using multimessenger information. *Physics Reports* [online]. 872 (2020). Closing in on the origin of Galactic cosmic rays using multimessenger information, pp. 1–98. ISSN: 0370-1573. DOI: https://doi.org/10.1016/j.physrep.2020.05.002. Available from: http://www.sciencedirect.com/science/article/pii/S0370157320301927.

[7] K. Greisen. End to the Cosmic-Ray Spectrum? *Physical Review Letters* [online]. 16 (Apr. 1966), pp. 748–750. DOI: 10.1103/PhysRevLett.16.748.

[8] G. T. Zatsepin and V. A. Kuzmin. Upper limit of the spectrum of cosmic rays. *Sov Phys JETP Lett.* 4 (1966), pp. 78–80.

[9] M. S. Longair. *High Energy Astrophysics*. Feb. 2011.

[10] M. Kachelrieß. „The rise and fall of top-down models as main UHECR sources". In: *20th Rencontres de Blois on Challenges in Particle Astrophysics*. 2008, pp. 215–224. arXiv: 0810.3017 [astro-ph].

[11] R. Aloisio, S. Matarrese, and A. V. Olinto. Super Heavy Dark Matter in light of BICEP2, Planck and Ultra High Energy Cosmic Rays Observations. *JCAP* [online]. 8, 024 (Aug. 2015), p. 024. DOI: 10.1088/1475-7516/2015/08/024. arXiv: 1504.01319 [astro-ph.HE].

[12] G. B. Gelmini, O. E. Kalashev, and D. V. Semikoz. GZK photons as ultra-high-energy cosmic rays. *Soviet Journal of Experimental and Theoretical Physics* [online]. 106.6 (June 2008), pp. 1061–1082. DOI: 10.1134/S106377610806006X. arXiv: astro-ph/0506128 [astro-ph].

[13] V. Berezinsky, M. Kachelrieß, and A. Vilenkin. Ultrahigh Energy Cosmic Rays without Greisen-Zatsepin-Kuzmin Cutoff. *Physical Review Letters* [online]. 79 (Dec. 1997), pp. 4302–4305. DOI: 10.1103/PhysRevLett.79.4302. eprint: astro-ph/9708217.

[14] Luca Maccione, Stefano Liberati, and Günter Sigl. Ultrahigh-Energy Photons as Probes of Lorentz Symmetry Violations in Stringy Space-Time Foam Models. *Phys. Rev. Lett.* [online]. 105 (2 July 2010), p. 021101. DOI: 10.1103/PhysRevLett.105.021101. Available from: https://link.aps.org/doi/10.1103/PhysRevLett.105.021101.

[15] T. Abu-Zayyad et al. Upper limit on the flux of photons with energies above 10^{19} eV using the Telescope Array surface detector. *Phys. Rev. D* [online]. 88 (11 Dec. 2013), p. 112005. DOI: 10.1103/PhysRevD.88.112005. Available from: https://link.aps.org/doi/10.1103/PhysRevD.88.112005.

[16] A Aab et al. Erratum: Search for photons with energies above 10^{18} eV using the hybrid detector of the Pierre Auger Observatory. *Journal of Cosmology and Astroparticle Physics* [online]. 2020.09 (Sept. 2020), E02–E02. DOI: 10.1088/1475-7516/2020/09/e02. Available from: https://doi.org/10.1088%2F1475-7516%2F2020%2F09%2Fe02.

[17] P. Homola, (O. Sushchov) et. al (CREDO Collab.) Search for Extensive Photon Cascades with the Cosmic-Ray Extremely Distributed Observatory. *CERN Proceedings* [online]. 1 (2018) (2018), p. 289. DOI: 10.23727/CERN-Proceedings-2018-001.289. arXiv: 1804.05614 [astro-ph.IM].

[18] D. Góra, (O. Sushchov) et. al (CREDO Collab.) Cosmic-Ray Extremely Distributed Observatory: status and perspectives. *Universe* [online]. 4.11 (2018), p. 111. DOI: 10.3390/universe4110111. arXiv: 1810.10410 [astro-ph.IM].

[19] P. Homola, (O. Sushchov) et. al (CREDO Collab.) Public engagement as a scientific tool to implement multi-messenger strategies with the Cosmic-Ray Extremely Distributed Observatory. *PoS* [online]. Asterics2019 (2019), p. 034. DOI: 10.22323/1.357.0034.

[20] P. Homola, (O. Sushchov) et. al (CREDO Collab.) Cosmic-Ray Extremely Distributed Observatory. *Symmetry* [online]. 12.11 (2020), p. 1835. DOI: https://doi.org/10.3390/sym12111835.

[21] R. J. Protheroe. On the nature of the cosmic ray positron spectrum. *Astrophysical Journal* [online]. 254 (Mar. 1982), pp. 391–397. DOI: 10.1086/159743.

[22] C. J. Cesarsky. Cosmic-ray confinement in the galaxy. *Annual Review of Astron and Astrophys* [online]. 18 (Jan. 1980), pp. 289–319. DOI: 10.1146/annurev.aa.18.090180.001445.

[23] P. O. Lagage and C. J. Cesarsky. The maximum energy of cosmic rays accelerated by supernova shocks. *Astronomy and Astrophysics*. 125 (Sept. 1983), pp. 249–257.

[24] Tadeusz Wibig and Arnold W. Wolfendale. At what particle energy do extragalactic cosmic rays start to predominate? *J. Phys. G* [online]. 31 (2005), pp. 255–264. DOI: 10.1088/0954-3899/31/3/005. arXiv: astro-ph/0410624.

[25] D. Allard, E. Parizot, and A.V. Olinto. On the transition from galactic to extragalactic cosmic-rays: Spectral and composition features from two opposite scenarios. *Astroparticle Physics* [online]. 27.1 (2007), pp. 61–75. ISSN: 0927-6505. DOI: https://doi.org/10.1016/j.astropartphys.2006.09.006. Available from: http://www.sciencedirect.com/science/article/pii/S092765050600137X.

[26] Dan Hooper, Subir Sarkar, and Andrew M. Taylor. The intergalactic propagation of ultra-high energy cosmic ray nuclei. *Astroparticle Physics* [online]. 27.2 (2007), pp. 199–212. ISSN: 0927-6505. DOI: https://doi.org/10.1016/j.astropartphys.2006.10.008. Available from: http://www.sciencedirect.com/science/article/pii/S0927650506001629.

[27] James W. Cronin. Cosmic rays: the most energetic particles in the universe. *Rev. Mod. Phys.* [online]. 71 (2 Mar. 1999), S165–S172. DOI: 10.1103/RevModPhys.71.S165. Available from: https://link.aps.org/doi/10.1103/RevModPhys.71.S165.

[28] M Nagano and Alan A Watson. Observations and implications of the ultrahigh-energy cosmic rays. *Reviews of Modern Physics*. 72.3 (2000), p. 689.

[29] W. Baade and F. Zwicky. Remarks on Super-Novae and Cosmic Rays. *Physical Review* [online]. 46 (July 1934), pp. 76–77. DOI: 10.1103/PhysRev.46.76.2.

[30] V. L. Ginzburg and S. I. Syrovatsky. Origin of Cosmic Rays. *Progress of Theoretical Physics Supplement* [online]. 20 (1961), pp. 1–83. DOI: 10.1143/PTPS.20.1.

[31] L O'C Drury. An introduction to the theory of diffusive shock acceleration of energetic particles in tenuous plasmas. *Reports on Progress in Physics* [online]. 46.8 (Aug. 1983), pp. 973–1027. DOI: 10.1088/0034-4885/46/8/002. Available from: https://doi.org/10.1088%2F0034-4885%2F46%2F8%2F002.

[32] R. Blandford and D. Eichler. Particle Acceleration at Astrophysical Shocks-a Theory of Cosmic-Ray Origin. *Physics Reports*. 154 (Oct. 1987), pp. 1–75.

[33] E.G. Berezhko and G.F. Krymsky. Acceleration of Cosmic Rays by Shock Waves. *Sov. Phys. Usp.* 31 (1988), pp. 27–51.

[34] Frank C. Jones and Donald C. Ellison. The plasma physics of shock acceleration. *Space Science Reviews* [online]. 58.1 (Dec. 1991), pp. 259–346. DOI: 10.1007/BF01206003.

[35] E. Fermi. On the Origin of the Cosmic Radiation. *Physical Review* [online]. 75 (Apr. 1949), pp. 1169–1174. DOI: 10.1103/PhysRev.75.1169.

[36] E. Fermi. Galactic Magnetic Fields and the Origin of Cosmic Radiation. *Astrophysical Journal* [online]. 119 (Jan. 1954), p. 1. DOI: 10.1086/145789.

[37] G. Morlino and D. Caprioli. Acceleration of cosmic rays in Tycho's SNR. *Memorie della Societa Astronomica Italiana*. 82 (2011), p. 731.

[38] P. Slane et al. A CR-hydro-NEI Model of the Structure and Broadband Emission from Tycho's Supernova Remnant. *Astrophysical Journal* [online]. 783, 33 (Mar. 2014), p. 33. DOI: 10.1088/0004-637X/783/1/33.

[39] J. Aleksić et al. Measurement of the Crab Nebula spectrum over three decades in energy with the MAGIC telescopes. *Journal of High Energy Astrophysics* [online]. 5 (Mar. 2015), pp. 30–38. DOI: 10.1016/j.jheap.2015.01.002. arXiv: 1406.6892 [astro-ph.HE].

[40] H. E. S. S. Collaboration et al. H.E.S.S. observations of RX J1713.7-3946 with improved angular and spectral resolution; evidence for gamma-ray emission extending beyond the X-ray emitting shell. *ArXiv e-prints* [online] (Sept. 2016). arXiv: 1609.08671 [astro-ph.HE].

[41] S. Archambault et al. Gamma-Ray Observations of Tycho's Supernova Remnant with VERITAS and Fermi. *Astrophysical Journal* [online]. 836, 23 (Feb. 2017), p. 23. DOI: 10.3847/1538-4357/836/1/23.

[42] A. Aab et al. Observation of a large-scale anisotropy in the arrival directions of cosmic rays above 8×10^{18} eV. *Science* [online]. 357.6357 (2017), pp. 1266–1270. ISSN: 0036-8075. DOI: 10.1126/science.aan4338. eprint: https://science.sciencemag.org/content/357/6357/1266.full.pdf. Available from: https://science.sciencemag.org/content/357/6357/1266.

[43] W. I. Axford. The origins of high-energy cosmic rays. *Astrophysical Journal, Supplement* [online]. 90 (Feb. 1994), pp. 937–944. DOI: 10.1086/191928.

[44] Pijushpani Bhattacharjee and Günter Sigl. Origin and propagation of extremely high-energy cosmic rays. *Physics Reports* [online]. 327.3 (2000), pp. 109–247. DOI: https://doi.org/10.1016/S0370-1573(99)00101-5. Available from: http://www.sciencedirect.com/science/article/pii/S0370157399001015.

[45] W. F. Swann. A Mechanism of Acquirement of Cosmic-Ray Energies by Electrons. *Physical Review* [online]. 43 (Feb. 1933), pp. 217–220. DOI: 10.1103/PhysRev.43.217.

[46] A. Y. Neronov, D. V. Semikoz, and I. I. Tkachev. Ultra-high energy cosmic ray production in the polar cap regions of black hole magnetospheres. *New Journal of Physics* [online]. 11.6, 065015 (June 2009), p. 065015. DOI: 10.1088/1367-2630/11/6/065015. arXiv: 0712.1737.

[47] Shan Gao et al. Modelling the coincident observation of a high-energy neutrino and a bright blazar flare. *Nature Astronomy* [online]. 3 (Jan. 2019). DOI: 10.1038/s41550-018-0610-1.

[48] Kohta Murase, Yoshiyuki Inoue, and Charles D. Dermer. Diffuse neutrino intensity from the inner jets of active galactic nuclei: Impacts of external photon fields and the blazar sequence. *Phys. Rev. D* [online]. 90 (2 July 2014), p. 023007. DOI: 10.1103/PhysRevD.90.023007. Available from: https://link.aps.org/doi/10.1103/PhysRevD.90.023007.

[49] A. M. Hillas. The Origin of Ultra-High-Energy Cosmic Rays. *Annual Review of Astron and Astrophys* [online]. 22 (1984), pp. 425–444. DOI: 10.1146/annurev.aa.22.090184.002233.

[50] Antoine Letessier-Selvon and Todor Stanev. Ultrahigh energy cosmic rays. *Rev. Mod. Phys.* [online]. 83 (3 Sept. 2011), pp. 907–942. DOI: 10.1103/RevModPhys.83.907. Available from: https://link.aps.org/doi/10.1103/RevModPhys.83.907.

[51] Mikhail Medvedev. A Constraint on Electromagnetic Acceleration of Highest Energy Cosmic Rays. *Physical review. E, Statistical, nonlinear, and soft matter physics* [online]. 67 (May 2003), p. 045401. DOI: 10.1103/PhysRevE.67.045401.

[52] G 't Hooft. Magnetic monopoles in unified gauge theories. *Nuclear Physics B* [online]. 79.2 (Sept. 1974), pp. 276–284. DOI: 10.1016/0550-3213(74)90486-6.

[53] A. M. Polyakov. Particle spectrum in quantum field theory. *Soviet Journal of Experimental and Theoretical Physics Letters*. 20 (Sept. 1974), p. 194.

[54] Pijushpani Bhattacharjee and N. C. Rana. Ultrahigh-energy particle flux from cosmic strings. *Physics Letters B* [online]. 246.3-4 (Aug. 1990), pp. 365–370. DOI: 10.1016/0370-2693(90)90615-D.

[55] Alexander Vilenkin. Gravitational field of vacuum domain walls. *Physics Letters B* [online]. 133.3 (1983), pp. 177–179. ISSN: 0370-2693. DOI: https://doi.org/10.1016/0370-2693(83)90554-3. Available from: http://www.sciencedirect.com/science/article/pii/0370269383905543.

[56] A. Vilenkin and E.P. S. Shellard. *Cosmic Strings and Other Topological Defects*. Cambridge University Press, July 2000. ISBN: 978-0-521-65476-0.

[57] V.A. Kuzmin and V. Rubakov. Ultrahigh-energy cosmic rays: A window on postinflationary reheating epoch of the Universe? *Physics of Atomic Nuclei - Phys Atom Nucl-Eng Tr.* 61 (June 1998), pp. 1028–1030.

[58] Michael Birkel and Subir Sarkar. Extremely high energy cosmic rays from relic particle decays. *Astroparticle Physics*. 9.4 (1998), pp. 297–309.

[59] Paul H Frampton, Bettina Keszthelyi, and Y Jack Ng. Longevity and highest-energy cosmic rays. *International Journal of Modern Physics D*. 8.01 (1999), pp. 117–122.

[60] Pasquale Blasi, Rainer Dick, and Edward W Kolb. Ultra-high energy cosmic rays from annihilation of superheavy dark matter. *Astroparticle Physics*. 18.1 (2002), pp. 57–66.

[61] T Weiler. Resonant absorption of cosmic-ray neutrinos by the relic-neutrino background. *Physical Review Letters*. 49.3 (1982), p. 234.

[62] Thomas J Weiler. Cosmic-ray neutrino annihilation on relic neutrinos revisited: a mechanism for generating air showers above the Greisen-Zatsepin-Kuzmin cutoff. *Astroparticle Physics*. 11.3 (1999), pp. 303–316.

[63] D Fargion, B Mele, and A Salis. Ultra-high-energy neutrino scattering onto relic light neutrinos in the galactic halo as a possible source of the highest energy extragalactic cosmic rays. *The Astrophysical Journal*. 517.2 (1999), p. 725.

[64] B.H.J. Mckellar et al. Neutrino clustering and the Z-burst model. *arXiv preprint hep-ph/0106123* (2001).

[65] R.U. Abbasi et al. Constraints on the diffuse photon flux with energies above 10^{18} eV using the surface detector of the Telescope Array experiment. *Astropart. Phys.* [online]. 110 (2019), pp. 8–14. DOI: 10.1016/j.astropartphys.2019.03.003. arXiv: 1811.03920 [astro-ph.HE].

[66] Julian Rautenberg. Limits on ultra-high energy photons with the Pierre Auger Observatory. *PoS* [online]. ICRC2019 (2019), p. 398. DOI: 10.22323/1.358.0398.

[67] W. D. Apel et al. KASCADE-Grande Limits on the Isotropic Diffuse Gamma-Ray Flux between 100 TeV and 1 EeV. *The Astrophysical Journal* [online]. 848.1 (Oct. 2017), p. 1. DOI: 10.3847/1538-4357/aa8bb7. Available from: https://doi.org/10.3847%2F1538-4357%2Faa8bb7.

[68] Yu. A. Fomin et al. Constraints on the flux of $\sim (10^{16} - 10^{17.5})$ eV cosmic photons from the EAS–MSU muon data. *Phys. Rev. D* [online]. 95 (12 June 2017), p. 123011. DOI: 10.1103/PhysRevD.95.123011. Available from: https://link.aps.org/doi/10.1103/PhysRevD.95.123011.

[69] F. Acero et al. Development of the Model of Galactic Interstellar Emission for Standard Point-Source Analysis of FERMI Large Area Telescope Data. *The Astrophysical Journal Supplement Series* [online]. 223.2 (Apr. 2016), p. 26. ISSN: 1538-4365. DOI: 10.3847/0067-0049/223/2/26. Available from: http://dx.doi.org/10.3847/0067-0049/223/2/26.

[70] W. L. Kraushaar et al. High-Energy Cosmic Gamma-Ray Observations from the OSO-3 Satellite. *The Astrophysical Journal* [online]. 177 (Nov. 1972), p. 341. DOI: 10.1086/151713.

[71] C. E. Fichtel et al. High-energy gamma-ray results from the second Small Astronomy Satellite. *The Astrophysical Journal* [online]. 198 (May 1975), pp. 163–182. DOI: 10.1086/153590.

[72] G. F. Bignami et al. The COS-B experiment for gamma-ray astronomy. *Space Science Instrumentation*. 1 (Aug. 1975), pp. 245–268.

[73] R. C. Hartman et al. „The EGRET High Energy Gamma Ray Telescope." In: *NASA Conference Publication*. Vol. 3137. NASA Conference Publication. Feb. 1992, pp. 116–125.

[74] M. Ackermann et al. Fermi-LAT Observations of the Diffuse γ-ray Emission: Implications for Cosmic Rays and the Interstellar Medium. *The Astrophysical Journal* [online]. 750.1 (Apr. 2012), p. 3. DOI: 10.1088/0004-637x/750/1/3. Available from: https://doi.org/10.1088%2F0004-637x%2F750%2F1%2F3.

[75] Meng Su, Tracy R. Slatyer, and Douglas P. Finkbeiner. Giant Gamma-Ray Bubbles from Fermi-LAT: Active Galactic Nucleus Activity or Bipolar Galactic Wind? *The Astrophysical Journal* [online]. 724.2 (Nov. 2010), pp. 1044–1082. ISSN: 1538-4357. DOI: 10.1088/0004-637x/724/2/1044. Available from: http://dx.doi.org/10.1088/0004-637X/724/2/1044.

[76] A.U. Abeysekara et al. On the sensitivity of the HAWC observatory to gamma-ray bursts. *Astroparticle Physics* [online]. 35.10 (May 2012), pp. 641–650. ISSN: 0927-6505. DOI: 10.1016/j.astropartphys.2012.02.001. Available from: http://dx.doi.org/10.1016/j.astropartphys.2012.02.001.

[77] Daniel Ferenc. The MAGIC gamma-ray observatory. *Nuclear Instruments and Methods in Physics Research Section A: Accelerators, Spectrometers, Detectors and Associated Equipment* [online]. 553 (Nov. 2005), pp. 274–281. DOI: 10.1016/j.nima.2005.08.085.

[78] R.W. Lessard. VERITAS: the Very Energetic Radiation Imaging Telescope Array System. *Astroparticle Physics* [online]. 11.1 (1999). TeV Astrophysics of Extragalactic Sources, pp. 243–246. ISSN: 0927-6505. DOI: https://doi.org/10.1016/S0927-6505(99)00057-2. Available from: http://www.sciencedirect.com/science/article/pii/S0927650599000572.

[79] James Hinton. The status of the HESS project. *New Astronomy Reviews* [online]. 48 (Mar. 2004). DOI: 10.1016/j.newar.2003.12.004.

[80] B.S. Acharya et al. Introducing the CTA concept. *Astroparticle Physics* [online]. 43 (2013). Seeing the High-Energy Universe with the Cherenkov Telescope Array - The Science Explored with the CTA, pp. 3–18. ISSN: 0927-6505. DOI: https://doi.org/10.1016/j.astropartphys.2013.01.007. Available from: http://www.sciencedirect.com/science/article/pii/S0927650513000169.

[81] M. Aguilar et al. Towards Understanding the Origin of Cosmic-Ray Electrons. *Phys. Rev. Lett.* [online]. 122 (10 Mar. 2019), p. 101101. DOI: 10.1103/PhysRevLett.122.101101. Available from: https://link.aps.org/doi/10.1103/PhysRevLett.122.101101.

[82] Bastian Beischer. „Measurement of high energy gamma rays from 200 MeV to 1 TeV with the Alpha Magnetic Spectrometer on the International Space Station". Veröffentlicht auf dem Publikationsserver der RWTH Aachen University; Dissertation, RWTH Aachen University, 2020. Dissertation. Aachen: RWTH Aachen University, 2020, 1 Online–Ressource (198 Seiten) : Illustrationen, Diagramme. DOI: 10.18154/RWTH-2020-06535. Available from: https://publications.rwth-aachen.de/record/792985.

[83] R. Beck. Galactic and Extragalactic Magnetic Fields. *AIP Conference Proceedings* [online]. 1085 (2008), pp. 83–97. DOI: 10.1063/1.3076806.

[84] JinLin Han. The magnetic structure of our Galaxy: a review of observations. *Proceedings of the International Astronomical Union* [online] (Nov. 2008), pp. 455–466. DOI: 10.1017/S1743921309031123.

[85] R. Beck. Magnetic fields in spiral galaxies. *The Astronomy and Astrophysics Review* [online]. 24 (Dec. 2016). DOI: 10.1007/s00159-015-0084-4.

[86] JinLin Han. Observing Interstellar and Intergalactic Magnetic Fields. *Annual Review of Astronomy and Astrophysics* [online]. 55 (Aug. 2017), pp. 111–157. DOI: 10.1146/annurev-astro-091916-055221.

[87] Jakov Borisovič Zel'dovič et al. *Magnetic fields in astrophysics*. Vol. 3. The fluid mechanics of astrophysics and geophysics. New York u.a: Gordon and Breach, 1983, XVI, 365 S : ill. ISBN: 0677063806. Available from: https://bib-pubdb1.desy.de/record/426440.

[88] Rainer Beck et al. Synthesizing Observations and Theory to Understand Galactic Magnetic Fields: Progress and Challenges. *Galaxies* [online]. 8.1 (Dec. 2019), p. 4. ISSN: 2075-4434. DOI: 10.3390/galaxies8010004. Available from: http://dx.doi.org/10.3390/galaxies8010004.

[89] Tess R Jaffe. Practical Modeling of Large-Scale Galactic Magnetic Fields: Status and Prospects. *Galaxies* [online]. 7 (Apr. 2019), p. 52. DOI: 10.3390/galaxies7020052.

[90] Ronnie Jansson and Glennys R. Farrar. A New Model of the Galactic Magnetic Field. *The Astrophysical Journal* [online]. 757.1 (Aug. 2012), p. 14. DOI: 10.1088/0004-637x/757/1/14. Available from: https://doi.org/10.1088%2F0004-637x%2F757%2F1%2F14.

[91] Richard J Wainscoat et al. A model of the 8-25 micron point source infrared sky. *The Astrophysical Journal Supplement Series*. 83 (1992), pp. 111–146.

[92] JinLin Han and GJ Qiao. The magnetic field in the disk of our Galaxy. *Astronomy and Astrophysics*. 288 (1994), pp. 759–772.

[93] Todor Stanev. Ultra-high-energy cosmic rays and the large-scale structure of the Galactic magnetic field. *The Astrophysical Journal*. 479.1 (1997), p. 290.

[94] Diego Harari, Silvia Mollerach, and Esteban Roulet. The toes of the ultra high energy cosmic ray spectrum. *Journal of High Energy Physics* [online]. 1999.08 (Aug. 1999), pp. 022–022. ISSN: 1029-8479. DOI: 10.1088/1126-6708/1999/08/022. Available from: http://dx.doi.org/10.1088/1126-6708/1999/08/022.

[95] P. G. Tinyakov and I. I. Tkachev. Correlation function of ultrahigh-energy cosmic rays favors point sources. *Journal of Experimental and Theoretical Physics Letters* [online]. 74.1 (July 2001), pp. 1–5. ISSN: 1090-6487. DOI: 10.1134/1.1402195. Available from: http://dx.doi.org/10.1134/1.1402195.

[96] JinLin Han. „Magnetic fields in our Galaxy: How much do we know?(II) Halo fields and the global field structure". In: *AIP Conference Proceedings*. Vol. 609. 1. American Institute of Physics. 2002, pp. 96–101.

[97] M. Prouza and R. Šmída. The Galactic magnetic field and propagation of ultra-high energy cosmic rays. *Astronomy and Astrophysics* [online]. 410.1 (Oct. 2003), pp. 1–10. ISSN: 1432-0746. DOI: 10.1051/0004-6361:20031281. Available from: http://dx.doi.org/10.1051/0004-6361:20031281.

[98] M. Kachelrieß, P. D. Serpico, and M. Teshima. The Galactic magnetic field as spectrograph for ultra-high energy cosmic rays. *Astroparticle Physics* [online]. 26.6 (Jan. 2007), pp. 378–386. DOI: 10.1016/j.astropartphys.2006.08.004. arXiv: astro-ph/0510444 [astro-ph].

[99] M. S. Pshirkov et al. Deriving the global structure the Galactic magnetic field from Faraday rotation measures of extragalactic sources. *The Astrophysical Journal* [online]. 738.2 (Aug. 2011), p. 192. DOI: 10.1088/0004-637x/738/2/192. Available from: https://doi.org/10.1088%2F0004-637x%2F738%2F2%2F192.

[100] J. C. Brown et al. Rotation Measures of Extragalactic Sources behind the Southern Galactic Plane: New Insights into the Large-Scale Magnetic Field of the Inner Milky Way. *The Astrophysical Journal* [online]. 663.1 (July 2007), pp. 258–266. DOI: 10.1086/518499. Available from: https://doi.org/10.1086%2F518499.

[101] Todor Stanev. Ultra–High-Energy Cosmic Rays and the Large-Scale Structure of the Galactic Magnetic Field. *The Astrophysical Journal* [online]. 479.1 (Apr. 1997), pp. 290–295. DOI: 10.1086/303866. Available from: https://doi.org/10.1086%2F303866.

[102] O. B. Sushchov et al. Search of ultra high energy cosmic rays' sources. FRI-radiogalaxy Centaurus A. *Kinematics and Physics of Celestial Bodies* [online]. 28.6 (Nov. 2012), pp. 270–279. DOI: 10.3103/S0884591312060062. arXiv: 1212.1402 [astro-ph.HE].

[103] O. Kobzar, (O. Sushchov) et. al. Search for ultra high-energy cosmic rays from radiogalaxy Virgo A. *Monthly Notices of the Royal Astronomical Society* [online]. 484.2 (Jan. 2019), pp. 1790–1799. ISSN: 1365-2966. DOI: 10.1093/mnras/stz094. Available from: http://dx.doi.org/10.1093/mnras/stz094.

[104] Kumiko Kotera and Angela V. Olinto. The Astrophysics of Ultrahigh-Energy Cosmic Rays. *Annual Review of Astronomy and Astrophysics* [online]. 49.1 (2011), pp. 119–153. DOI: 10.1146/annurev-astro-081710-102620. eprint: https://doi.org/10.1146/annurev-astro-081710-102620. Available from: https://doi.org/10.1146/annurev-astro-081710-102620.

[105] P. P. Kronberg. Extragalactic magnetic fields. *Reports on Progress in Physics* [online]. 57.4 (Apr. 1994), pp. 325–382. DOI: 10.1088/0034-4885/57/4/001.

[106] P. P. Kronberg et al. A Global Probe of Cosmic Magnetic Fields to High Redshifts. *Astrophysical Journal* [online]. 676.1 (Mar. 2008), pp. 70–79. DOI: 10.1086/527281. arXiv: 0712.0435 [astro-ph].

[107] Dongsu Ryu et al. Turbulence and Magnetic Fields in the Large-Scale Structure of the Universe. *Science* [online]. 320.5878 (2008), pp. 909–912. ISSN: 0036-8075. DOI: 10.1126/science.1154923. eprint: https://science.sciencemag.org/content/320/5878/909.full.pdf. Available from: https://science.sciencemag.org/content/320/5878/909.

[108] Ruth Durrer and Andrii Neronov. Cosmological Magnetic Fields: Their Generation, Evolution and Observation. *The Astronomy and Astrophysics Review* [online]. 21 (Mar. 2013). DOI: 10.1007/s00159-013-0062-7.

[109] Luigina Feretti et al. Clusters of galaxies: observational properties of the diffuse radio emission. *Astronomy and Astrophysics Reviews* [online]. 20, 54 (May 2012), p. 54. DOI: 10.1007/s00159-012-0054-z. arXiv: 1205.1919 [astro-ph.CO].

[110] S. Brown et al. Limiting magnetic fields in the cosmic web with diffuse radio emission. *Monthly Notices of the Royal Astronomical Society* [online]. 468.4 (Mar. 2017), pp. 4246–4253. ISSN: 0035-8711. DOI: 10.1093/mnras/stx746. eprint: https://academic.oup.com/mnras/article-pdf/468/4/4246/14013230/stx746.pdf. Available from: https://doi.org/10.1093/mnras/stx746.

[111] M. S. Pshirkov, P. G. Tinyakov, and F. R. Urban. New Limits on Extragalactic Magnetic Fields from Rotation Measures. *Phys. Rev. Lett.* [online]. 116 (19 May 2016), p. 191302. DOI: 10.1103/PhysRevLett.116.191302. Available from: https://link.aps.org/doi/10.1103/PhysRevLett.116.191302.

[112] Alex Zucca, Yun Li, and Levon Pogosian. Constraints on primordial magnetic fields from Planck data combined with the South Pole Telescope CMB B-mode polarization measurements. *Phys. Rev. D* [online]. 95 (6 Mar. 2017), p. 063506. DOI: 10.1103/PhysRevD.95.063506. Available from: https://link.aps.org/doi/10.1103/PhysRevD.95.063506.

[113] Andrii Neronov and Ievgen Vovk. Evidence for Strong Extragalactic Magnetic Fields from Fermi Observations of TeV Blazars. *Science* [online]. 328.5974 (2010), pp. 73–75. ISSN: 0036-8075. DOI: 10.1126/science.1184192. eprint: https://science.sciencemag.org/content/328/5974/73.full.pdf. Available from: https://science.sciencemag.org/content/328/5974/73.

[114] Eli Waxman and Jordi Miralda-Escudé. Images of Bursting Sources of High-Energy Cosmic Rays: Effects of Magnetic Fields. *The Astrophysical Journal* [online]. 472.2 (Dec. 1996), pp. L89–L92. DOI: 10.1086/310367. Available from: https://doi.org/10.1086%2F310367.

[115] Günter Sigl, Francesco Miniati, and Torsten A. Ensslin. Ultrahigh energy cosmic rays in a structured and magnetized universe. *Phys. Rev. D* [online]. 68 (4 Aug. 2003), p. 043002. DOI: 10.1103/PhysRevD.68.043002. Available from: https://link.aps.org/doi/10.1103/PhysRevD.68.043002.

[116] F. W. Stecker, M. A. Malkan, and S. T. Scully. Intergalactic Photon Spectra from the Far-IR to the UV Lyman Limit for 0 <z< 6 and the Optical Depth of the Universe to High-Energy Gamma Rays. *The Astrophysical Journal* [online]. 648.2 (Sept. 2006), pp. 774–783. ISSN: 1538-4357. DOI: 10.1086/506188. Available from: http://dx.doi.org/10.1086/506188.

[117] Tanja M. Kneiske et al. Implications of cosmological gamma-ray absorption. 2. Modification of gamma-ray spectra. *Astron. Astrophys.* [online]. 413 (2004), pp. 807–815. DOI: 10.1051/0004-6361:20031542. arXiv: astro-ph/0309141.

[118] A. Franceschini, G. Rodighiero, and M. Vaccari. Extragalactic optical-infrared background radiation, its time evolution and the cosmic photon-photon opacity. *Astronomy and Astrophysics* [online]. 487.3 (2008), pp. 837–852. DOI: 10.1051/0004-6361:200809691. Available from: https://app.dimensions.ai/details/publication/pub.1056940338%20and%20https://www.aanda.org/articles/aa/pdf/2008/33/aa09691-08.pdf.

[119] Justin D. Finke, Soebur Razzaque, and Charles D. Dermer. Modeling the Extragalactic Background Light from Stars and Dust. *The Astrophysical Journal* [online]. 712.1 (Feb. 2010), pp. 238–249. DOI: 10.1088/0004-637x/712/1/238. Available from: https://doi.org/10.1088%2F0004-637x%2F712%2F1%2F238.

[120] A. Domínguez et al. Extragalactic background light inferred from AEGIS galaxy-SED-type fractions. *Monthly Notices of the Royal Astronomical Society* [online]. 410.4 (Jan. 2011), pp. 2556–2578. ISSN: 0035-8711. DOI: 10.1111/j.1365-2966.2010.17631.x. eprint: https://academic.oup.com/mnras/article-pdf/410/4/2556/6295256/mnras0410-2556.pdf. Available from: https://doi.org/10.1111/j.1365-2966.2010.17631.x.

[121] Rudy C. Gilmore et al. Semi-analytic modelling of the extragalactic background light and consequences for extragalactic gamma-ray spectra. *Monthly Notices of the Royal Astronomical Society* [online]. 422.4 (May 2012), pp. 3189–3207. ISSN: 0035-8711. DOI: 10.1111/j.1365-2966.2012.20841.x. eprint: https://academic.oup.com/mnras/article-pdf/422/4/3189/18601416/mnras0422-3189.pdf. Available from: https://doi.org/10.1111/j.1365-2966.2012.20841.x.

[122] J. L. Puget, F. W. Stecker, and J. H. Bredekamp. Photonuclear interactions of ultrahigh energy cosmic rays and their astrophysical consequences. *Astrophysical Journal* [online]. 205 (Apr. 1976), pp. 638–654. DOI: 10.1086/154321.

[123] J. K. Daugherty and A. K. Harding. Pair production in superstrong magnetic fields. *Astrophysical Journal* [online]. 273 (Oct. 1983), pp. 761–773. DOI: 10.1086/161411.

[124] R. W. Brown et al. Role of $\gamma + \gamma \rightarrow e^+ + e^- + e^+ + e^-$ in Photoproduction, Colliding Beams, and Cosmic Photon Absorption. *Phys. Rev. D* [online]. 8 (9 Nov. 1973), pp. 3083–3102. DOI: 10.1103/PhysRevD.8.3083. Available from: https://link.aps.org/doi/10.1103/PhysRevD.8.3083.

[125] Oleg Kalashev, V.A. Kuzmin, and Dmitry Semikoz. Top-Down Models and Extremely High Energy Cosmic Rays (Dec. 1999).

[126] S. V. Demidov and O. E. Kalashev. Double pair production by ultra-high-energy cosmic ray photons. *Journal of Experimental and Theoretical Physics* [online]. 108.5 (May 2009), pp. 764–769. ISSN: 1090-6509. DOI: 10.1134/s1063776109050057. Available from: http://dx.doi.org/10.1134/S1063776109050057.

[127] A. Mastichiadis. Relativistic electrons in photon fields: effects of triplet pair production on inverse Compton gamma-ray spectra. *Monthly Notices of the Royal Astronomical Society* [online]. 253.2 (Nov. 1991), pp. 235–244. ISSN: 0035-8711. DOI: 10.1093/mnras/253.2.235. eprint: https://academic.oup.com/mnras/article-pdf/253/2/235/32290415/mnras253-0235.pdf. Available from: https://doi.org/10.1093/mnras/253.2.235.

[128] Matthew G. Baring and Alice K. Harding. Magnetic Photon Splitting: Computations of Proper-Time Rates and Spectra. *The Astrophysical Journal* [online]. 482.1 (June 1997), pp. 372–376. DOI: 10.1086/304152. Available from: https://doi.org/10.1086%2F304152.

[129] Vladimir V. Usov. Photon Splitting in the Superstrong Magnetic Fields of Pulsars. *The Astrophysical Journal* [online]. 572.1 (June 2002), pp. L87–L90. DOI: 10.1086/341505. Available from: https://doi.org/10.1086%2F341505.

[130] Thomas Erber. High-Energy Electromagnetic Conversion Processes in Intense Magnetic Fields. *Rev. Mod. Phys.* [online]. 38 (4 Oct. 1966), pp. 626–659. DOI: 10.1103/RevModPhys.38.626. Available from: https://link.aps.org/doi/10.1103/RevModPhys.38.626.

[131] V. N. Baĭer and V. M. Katkov. Quasiclassical Theory of Bremsstrahlung by Relativistic Particles. *Soviet Journal of Experimental and Theoretical Physics*. 28 (Apr. 1969), p. 807.

[132] Wu-yang Tsai and Thomas Erber. Photon pair creation in intense magnetic fields. *Phys. Rev. D* [online]. 10 (2 July 1974), pp. 492–499. DOI: 10.1103/PhysRevD.10.492. Available from: https://link.aps.org/doi/10.1103/PhysRevD.10.492.

[133] L. D. Landau and E. M. Lifshitz. *The classical theory of fields; 4th ed.* Course of theoretical physics. Trans. from the 6th rev. ed. of Theoriya Pola, Nauka, Moscow, 1973. Oxford: Pergamon, 1975. Available from: https://cds.cern.ch/record/101807.

[134] F. R. Elder et al. Radiation from Electrons in a Synchrotron. *Phys. Rev.* [online]. 71 (11 June 1947), pp. 829–830. DOI: 10.1103/PhysRev.71.829.5. Available from: https://link.aps.org/doi/10.1103/PhysRev.71.829.5.

[135] J. D. Jackson. Electrodynamics, Classical. In: *digital Encyclopedia of Applied Physics*. American Cancer Society, 2003. ISBN: 9783527600434. DOI: 10.1002/3527600434.eap109. eprint: https://onlinelibrary.wiley.com/doi/pdf/10.1002/3527600434.eap109. Available from: https://onlinelibrary.wiley.com/doi/abs/10.1002/3527600434.eap109.

[136] P. Homola et al. Simulation of ultra-high energy photon propagation in the geomagnetic field. *Computer Physics Communications* [online]. 173.1-2 (Dec. 2005), pp. 71–90. ISSN: 0010-4655. DOI: 10.1016/j.cpc.2005.07.001. Available from: http://dx.doi.org/10.1016/j.cpc.2005.07.001.

[137] P. Homola et al. Characteristics of geomagnetic cascading of ultrahigh energy photons at the southern and northern sites of the Pierre Auger Observatory. *Astropart. Phys.* [online]. 27 (2007), pp. 174–184. DOI: 10.1016/j.astropartphys.2006.10.005. arXiv: astro-ph/0608101.

[138] Markus Risse and Piotr Homola. Search For Ultra-High Energy Photons Using Air Showers. *Modern Physics Letters A* [online]. 22.11 (2007), pp. 749–766. DOI: 10.1142/S0217732307022864. eprint: https://doi.org/10.1142/S0217732307022864. Available from: https://doi.org/10.1142/S0217732307022864.

[139] K. Almeida Cheminant, (O. Sushchov) et. al. Search for ultra-high energy photons through preshower effect with gamma-ray telescopes: Study of CTA-North efficiency. *Astroparticle Physics* [online]. 123 (2020), p. 102489. ISSN: 0927-6505. DOI: https://doi.org/10.1016/j.astropartphys.2020.102489. Available from: http://www.sciencedirect.com/science/article/pii/S092765052030061X.

[140] W. Bednarek. Cascades initiated by EHE photons in the magnetic field of the Earth and the Sun. *arXiv e-prints* [online], astro-ph/9911266 (Nov. 1999), astro–ph/9911266. arXiv: astro-ph/9911266 [astro-ph].

[141] N. Dhital, (O. Sushchov) et. al (CREDO Collab.) *Cosmic ray ensembles as signatures of ultra-high energy photons interacting with the solar magnetic field*. 2019. arXiv: 1811.10334 [astro-ph.HE].

[142] M. Banaszkiewicz, W. I. Axford, and J. F. McKenzie. An analytic solar magnetic field model. *Astronomy and Astrophysics*. 337 (Sept. 1998), pp. 940–944.

[143] Michal Niedzwiecki et al. *Recognition and classification of the cosmic-ray events in images captured by CMOS/CCD cameras*. 2019. arXiv: 1909.01929 [astro-ph.IM].

[144] D. Góra, (O. Sushchov) et. al (CREDO Collab.) Cosmic Ray Extremely Distributed Observatory: Status and perspectives of a global cosmic ray detection framework. *PoS* [online]. ICRC2019 (2020), p. 272. DOI: 10.22323/1.358.0272. arXiv: 1908.04139 [astro-ph.IM].

[145] R. Kamiński, (O. Sushchov) et. al (CREDO Collab.) CREDO Project. *Acta Physica Polonica B* [online]. 50 (Jan. 2019), p. 2001. DOI: 10.5506/APhysPolB.50.2001.

[146] Łukasz Bibrzycki and et al. (CREDO Collab.) Towards a global cosmic ray sensor network: CREDO Detector as the first open source mobile application enabling detection of penetrating radiation. *Symmetry, Special Issue on Cosmic Rays* (2020).

[147] R. Alves Batista et al. CRPropa 3: a public astrophysical simulation framework for propagating extraterrestrial ultra-high energy particles. *Journal of Cosmology and Astroparticle Physics* [online]. 2016.05 (May 2016), pp. 038–038. DOI: 10.1088/1475-7516/2016/05/038. Available from: https://doi.org/10.1088%2F1475-7516%2F2016%2F05%2F038.

[148] *CRPropa website*. Available from: https://crpropa.desy.de/ [Accessed 10/31/2020].

[149] W. M. Yao et al. Review of particle physics. English. *Journal of Physics G: Nuclear and Particle Physics* [online]. 33.1 (July 2006). ISSN: 0954-3899. DOI: 10.1088/0954-3899/33/1/001.

[150] J. R. Cash and Alan H. Karp. A Variable Order Runge-Kutta Method for Initial Value Problems with Rapidly Varying Right-Hand Sides. *ACM Trans. Math. Softw.* [online]. 16.3 (Sept. 1990), pp. 201–222. ISSN: 0098-3500. DOI: 10.1145/79505.79507. Available from: https://doi.org/10.1145/79505.79507.

[151] M. Berkova, R. Clay, and E. Eroshenko V. Yanke. „Atmospheric Variations As Observed by the Adelaide and Buckland Muon Telescopes". In: *International Cosmic Ray Conference*. Vol. 33. International Cosmic Ray Conference. Jan. 2013, p. 1650.

[152] Roger Clay. Applications of the Adelaide HEAMS muon detector. *PoS* [online]. ICRC2015 (2016), p. 218. DOI: 10.22323/1.236.0218.

[153] Arman Tursunov et al. Effect of Electromagnetic Interaction on Galactic Center Flare Components. *Astrophys. J.* [online]. 897.1 (2020), p. 99. ISSN: 0370-1573. DOI: 10.3847/1538-4357/ab980e. arXiv: 1912.08174 [astro-ph.GA].

[154] Daniel J. H. Chung, Edward W. Kolb, and Antonio Riotto. Superheavy dark matter. *Physical Review D* [online]. 59.2 (Nov. 1998). ISSN: 1089-4918. DOI: 10.1103/physrevd.59.023501. Available from: http://dx.doi.org/10.1103/PhysRevD.59.023501.

List of Figures

List of Tables